Volume Grating Couplers for Optical Interconnects: Analysis, Design, Fabrication and Testing

A Thesis
Presented to
The Academic Faculty

by

Ricardo A. Villalaz

In Partial Fulfillment
of the Requirements for the Degree
Doctor of Philosophy

School of Electrical and Computer Engineering
Georgia Institute of Technology
July 2004

Volume Grating Couplers for Optical Interconnects: Analysis, Design, Fabrication and Testing

Approved by:

Professor Thomas K. Gaylord, Chair

Professor Elias N. Glytsis, Co-Chair

Professor Ali Adibi

Professor John A. Buck

Professor Paul A. Kohl

Date Approved: 12 July 2004

To my parents,

Itzel y Ricardo,

and to my wife,

Lea

ACKNOWLEDGEMENTS

The work presented in this dissertation could not have been completed without the support and contributions of many people. First, I would like to thank my advisors, Prof. Thomas K. Gaylord and Prof. Elias N. Glytsis. Their dedication, patience, and generosity have provided inspiration and motivation throughout the years. Their knowledge, curiosity and creativity have been essential to the completion of this work. I would also like to thank the members of my thesis defense committee, Prof. Ali Adibi, Prof. John Buck, and Prof. Paul Kohl for their insightful questions and observations.

The fellow students and researchers is have had the pleasure of working with for the past few years have also made many contributions, big and small, to the completion of this work. Dr. Anthony Mule' must be thanked for the development of the waveguide fabrication techniques and some of the measurement configurations used as for this research. Furthermore, he must be thanked for the many helpful discussions and encouragement he provided. Dr. Steve Schultz taught me how to make volume gratings, and Dr. Muhannad Bakir fabricated the polymer pillars described in this dissertation. Thanks to Mr. Brent Bachim for helping so much with the use of optical fibers and other materials and many helpful discussions, and to Dr. Shun-Der Wu for his sharp observations on the fabrication and performance of volume grating couplers and for the energy and enthusiasm he brought to the lab. Many thanks also to Dr. Neena Imam, Mr. Greg Kilby, Ms. Carole Montarou, Mr. Olowafemi Ogunsola, Mr. Justin Stay, Mr. Hiren Thacker, Dr. Greg Van Wiggeren, Mr. Yu-Ming (Arthur) Wu and Dr. Yan Yi for their discussions, their encouragement and their help at many different times. Also, many thanks to previous members of my research group for blazing the path for me and my contemporaries. My office mate for most of my time here, Mr. Mohammad Braiwish, also deserves special thanks for his optimism and for the many history lessons and political and cultural discussions we shared. Many thanks as well to the staffs of the School of Electrical and Computer Engineering, the Microelectronics

Research Center and the Packaging Research Center for their support in the use of their excellent facilities.

I must also thank the many friends that have welcomed me in Atlanta and made my time at GT one to cherish. I could not have done this without you.

Finally, I would like to thank my family. All of you have helped me get here and your support is invaluable to me. Al, Candice, Niki, Hank, Hal, Kate, and Brook, thanks for welcoming me into your family. Itzel, Ivonne, Víctor, Juan Raúl y José Pablo, you always bring a smile to my face and I am always looking forward to seeing you again. No words can express the gratitude I feel towards my mother Itzel and my father Ricardo for giving me so many opportunities in life, and more love and support than anyone could ever hope for. To my wife Lea, thanks for all your love and patience, especially as the final stages of this research were completed. You have made my life happier and better every day I have known you.

RICARDO A. VILLALAZ

Georgia Institute of Technology
July 2004

TABLE OF CONTENTS

LIST OF TABLES

LIST OF FIGURES

SUMMARY

Optical interconnects are important to the future development of microelectronics. Volume grating couplers (VGCs) provide a compact, efficient coupling mechanism that is compatible with microelectronics fabrication processes. In this dissertation, some of the performance characteristics of VGCs are investigated. Also, integration of VGCs with Sea of Polymer Pillars (SoPP), an emerging high-density input/output interconnect technology, is demonstrated and its performance quantitatively investigated. First, the polarization-dependent performance of VGCs is analyzed, and the design constraints for achieving high-efficiency polarization-dependent and polarization-independent VGCs are examined. The effects of loss on VGC performance are also presented. Then, the wavelength response of VGCs and its dependence on grating parameters is quantitatively examined. Experimental demonstrations of polarization-dependent and polarization-independent VGCs are then presented. Finally, a VGC integrated with a SoPP is demonstrated and its performance characterized.

CHAPTER 1

INTRODUCTION

Optical interconnects are important for the future development of microelectronics and optoelectronics packaging. They are also important for VLSI, both for clock distribution and input/output data transfer [1–4]. As semiconductor circuits achieve higher speeds and complexities, they will be more limited by the speed of their interconnects than by their gate delays [1]. The use of optical interconnects may solve this problem and even enable new interconnect architectures. There are no fundamental physical barriers to the development of dense optical interconnections, for both on-chip and between-chip applications. However, cost-effective technological solutions will be necessary to make them a reality [3]. Free-space optical interconnects, have been extensively investigated [1, 2]. Due to their limitations in terms of alignment sensitivity, wavelength sensitivity, and other parameters [5], alternate solutions have been proposed. Several groups have proposed the use of substrate-mode interconnects in which light is guided through a thick substrate by total internal reflection [6]. Optical interconnects of this type have been demonstrated by Chen *et al.* [7] and by Yeh *et al.* [8]. Substrate modes are relatively simple to couple into, because any propagation angle larger than the critical angle is supported. However, for long distances, they are sensitive to source beam divergence, and signals transmitted in this way are difficult to split and to turn into various directions [9]. Thin film guided-wave optical interconnects are more difficult to couple light into, because only a discrete set of modes (and therefore, of coupling angles) are supported. However, once coupling is achieved, the light beams can be easily controlled to avoid divergence (using channel waveguides) and to route and split the signals through the use of integrated power splitters and directional couplers.

Efficient coupling of light into and out of optical waveguides is necessary in practical thin film guided-wave optical interconnect systems. Volume grating couplers (VGCs), first demonstrated by Kogelnik and Sosnowski [10], provide high-efficiency coupling and ease of manufacture in a compact device [11–14]. In order for VGCs to be used in practical optical interconnect systems, their performance capabilities and limitations must be understood. Therefore, it is the aim of this research to quantify their performance with respect to the crucial parameters of polarization and wavelength of the source light and to demonstrate their functionality in optical interconnect systems.

1.1 Background

1.1.1 Optical vs Electrical Interconnects

For the past few decades, electronic systems have used electrical wires as the interconnections between and within chips and boards. Continuing increases in the speed and complexity of these circuits, however, will eventually demand interconnection speeds beyond those achievable by electrical interconnects [1]. For example, a recent paper by Mule'*et al.* [15] identifies the $32nm$ technology generation of the 2002 International Technology Roadmap for Semiconductors (ITRS) [16] as the first generation in which alternate methods of clock signal distribution may be required. This paper further identifies the percentage of the clock period consumed by the global skew and short-term jitter (delay variations) of electrical interconnects as the main challenge to their continued use. In the following section some of the most important limitations of electrical interconnects are discussed. Then, the potential of optical interconnects to overcome these limitations, as well as the existing challenges to the implementation of optical interconnects, will be addressed.

1.1.1.1 Limitations of Electrical Interconnects

Some of the limitations of electrical interconnects are as follows:

1. Latency increases as interconnect width decreases and interconnect distance increases. As more components are compressed into an integrated circuit, interconnect distances increase and their lateral sizes decrease. Since both of these increase the capacitance and thus the latency of the interconnect with respect to other circuit components, they lead to the interconnect becoming a bottleneck for the system. Additionally, in fan-out applications, such as clock-distribution networks, latency increases as the number of destinations increases [1, 17].

2. System redesign is usually required as speed increases. In electrical interconnects, the loss, inductance, and crosstalk all can vary with frequency, so that the interconnects have to be redesigned every time a signal rate increase is required.

3. Crosstalk increases as interconnect width decreases and speed increases. Higher modulation frequencies, closer spacing between interconnects, and smaller interconnect dimensions all lead to higher interference between signals in adjacent interconnects.

4. Power dissipation increases with interconnect distance. This occurs because longer wires inevitably have higher resistance. Also, to avoid reflections from capacitive loads, line terminations (which increase power dissipation) may be necessary at higher signal rates [3].

5. Interconnect delays vary with temperature. Since the resistance of metals varies with temperature, the propagation delay of signals and the latency of electrical interconnects may change. At higher signal rates, this can seriously affect signal synchronization [3, 15].

1.1.1.2 Promise and Challenges of Optical Interconnects

Optical interconnects have the potential to address the limitations of electrical interconnects described in the above section. The advantages of optical interconnects, with respect to the limitations of electrical interconnects described above, are as follows:

1. **Latency:** In optical interconnects, unlike in electrical interconnects, latency does not increase with the number of components of the network [1]. Also in the case of optical interconnects, latency is not as strong a function of interconnect dimensions, since the speed of propagation of light depends mostly on the index of refraction of the material.

2. **System redesign:** The frequency of light waves is in the THz range. Interconnect signal frequencies are much smaller than this and therefore do not play a significant role in the design of the interconnect. Therefore, changing the signaling speed generally does not lead to a redesign as it does in electrical interconnects.

3. **Crosstalk:** In optical interconnects, increased modulation frequencies do not lead to an increase in crosstalk. This is because, as was mentioned before, modulation frequencies are very small compared to the carrier frequency of light. Also, photons do not interact as easily as electrons, and therefore electromagnetic interference is minimized.

4. **Power dissipation:** Especially for longer distances, optical interconnects have an advantage in that their total impedance remains constant as distance increases, while the resistance of electrical interconnects increases with distance [3]. Also, the propagation of light is not affected by the impedance of the receiver circuit and therefore line terminations are not needed [3, 18].

5. **Delay variations:** The index of refraction of optical media is much less temperature-sensitive than the resistance of electrical wires and therefore delay variations are much smaller in optical interconnects [3].

In order to gain widespread acceptance, optical interconnects must surmount certain technological challenges. These include the following:

1. **Detectors and receiver circuits:** Detectors and receiver circuits with low latency and low power dissipation must be developed. It is expected that a significant share of the power dissipation in an optical interconnect will occur in the detector/receiver circuit [19]. The use of detectors with low capacitance, such as inverted metal-semiconductor-metal (I-MSM) detectors is considered essential to this development.

2. **Optical sources:** Sources that are low-cost, easy to integrate, and efficient must be developed. Mode, polarization, and wavelength stability may also be required, depending on the characteristics of the specific system. Vertical-cavity surface-emitting lasers (VCSELs) [20] are good candidates to fulfill these requirements.

3. **Low-loss media:** Low-loss materials for the propagation of light that are compatible with semiconductor processes must be developed. For optical interconnects to work, light must propagate from one point to another. This may occur freely either in air or in a dielectric material or through total internal reflection as substrate modes or as thin-film guided waves. In the case of simple propagation through a dielectric, and in the case of substrate modes and thin-film guided waves, the propagation medium must be low-loss, low-cost, and compatible with the fabrication of the rest of the electronic system of which it will be a part. Several polymer materials have good characteristics as media for the propagation of light and fabrication processes compatible with microelectronics [21–23].

4. **Couplers:** For substrate mode and thin film guided-wave applications, efficient

couplers must be developed in order to get the optical signals into and out of the propagation medium without significant loss.

1.1.2 Types of Optical Interconnects

Three main types of optical interconnects for microelectronic systems have been proposed. They are classified by the nature of the propagation of the light, and are described below.

1.1.2.1 Freespace Optical Interconnects

In freespace optical interconnects, light propagates from source to detector through a bulk medium. A diagram of a freespace optical interconnect is shown in Fig. 1.1. Such an interconnect has the capacity for high interconnection density, but has disadvantages including the need for 3D alignment between detectors and signal beams and high crosstalk [5].

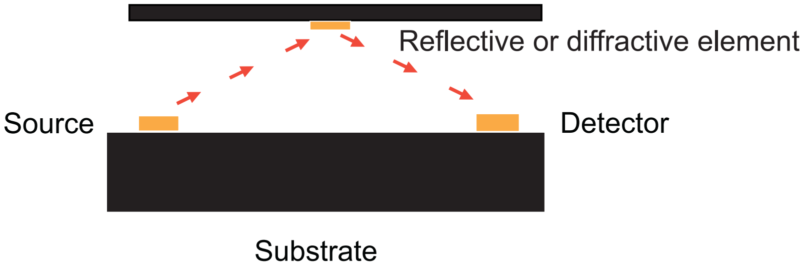

Figure 1.1: Diagram of a freespace optical interconnect.

1.1.2.2 Substrate-Mode Optical Interconnects

In a substrate-mode optical interconnect, a thick transparent substrate acts to confine the light. Through total internal reflection, light is prevented from escaping the substrate. A substrate-mode optical interconnect is shown in Fig. 1.2a. Light must be coupled from the source into the substrate and from the substrate to the detector. Substrate-mode optical interconnects are easy to couple light into because they effectively support many modes and therefore almost any propagation angle greater than the critical angle of the substrate is supported. These interconnects require only 2D alignment, are more robust than freespace optical interconnects, and have less crosstalk. However, substrate-mode optical interconnects cannot compensate for source divergence, and therefore collimated sources are needed, especially for longer distances [9]. These interconnects are also somewhat bulky and alignment sensitive.

1.1.2.3 Thin Film Guided-Wave Optical Interconnects

Thin film guided-wave optical interconnects are also based on total internal reflection. In this case, however, a high-index thin film is directly above a substrate and the film acts as the waveguide. Thin film guided-wave optical interconnects, like substrate-mode interconnects, have the advantages of requiring only 2D alignment, being robust, and having low crosstalk. A thin film guided-wave optical interconnect is shown in Fig. 1.2b. Because the waveguide is thin, only a discrete, limited number of modes (and therefore coupling angles) are allowed. This makes coupling light into and out of them a more difficult task than in the previous case. However, thin film waveguides can be patterned as channels with the use of standard photolithographic techniques. The use of channel waveguides allows more tolerance for source divergence than is possible with substrate-mode interconnects and also allows for the use of integrated optics devices such as power splitters and directional couplers to distribute and route signals. Because of these advantages, the research described in this thesis focuses only on thin film guided-wave optical interconnects.

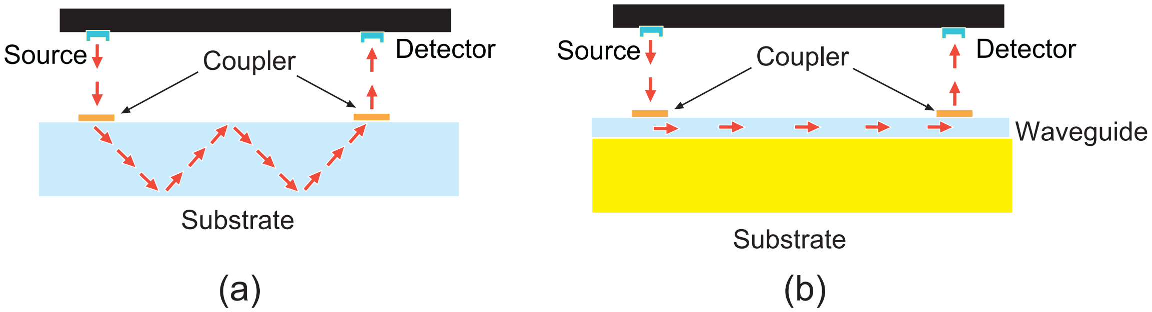

Figure 1.2: Diagrams of: a) substrate mode optical interconnect b) thin film guided-wave optical interconnect.

1.1.3 Types of Couplers for Guided-Wave Optical Interconnects

Three types of devices have been used as couplers for guided-wave optical waveguides. They are prism couplers, reflective couplers, and diffractive couplers.

1.1.3.1 Prism Couplers

A prism coupler is illustrated in Fig. 1.3. By bringing a prism into close proximity to the waveguide and orienting the input beam in a direction in which the tangential component (parallel to the prism boundary in contact with the waveguide) of its wavevector in the prism matches that of one of the waveguide modes, power can be coupled into the waveguide. The transfer of optical power through the small air gap between prism and waveguide is due to frustrated total internal reflection. In reciprocal fashion, light can also be coupled out [24]. Prism coupling requires very precise placement, and furthermore prisms are bulky devices. Therefore, they are not compatible with optical interconnects for microelectronic systems.

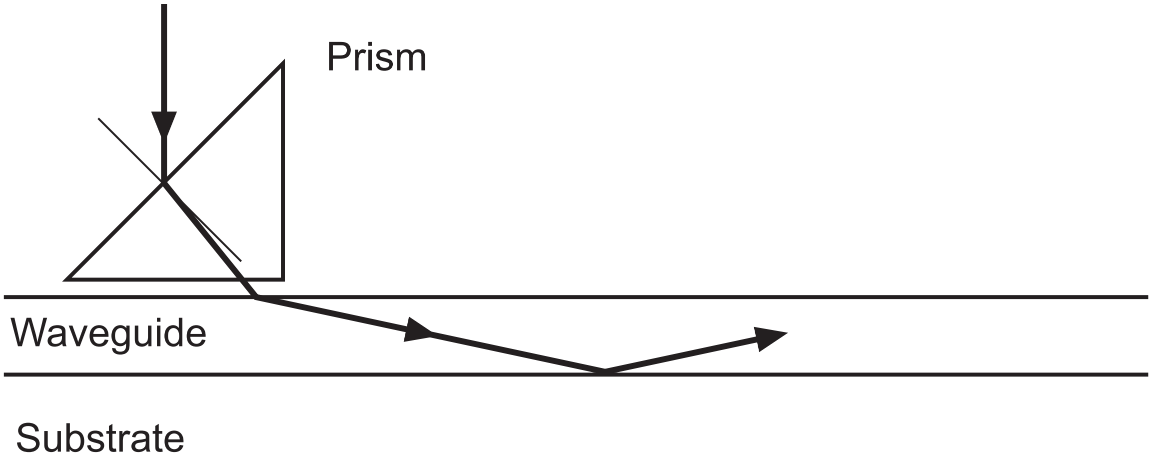

Figure 1.3: Diagram of a prism coupler

1.1.3.2 Reflective Couplers

In reflective couplers, light is coupled into or out of a waveguide by a reflective surface. For example, polymer waveguides can be cleaved at a 45° angle and then the cleaved surface can be coated with gold to increase reflectivity [25, 26]. Also, RIE etching at 45° has been used to produce reflective couplers in multimode polymer waveguides with high estimated efficiency [27, 28]. A diagram of a reflective coupler is shown in Fig. 1.4. Fabrication of high-quality reflective surfaces needed for high-efficiency coupling on polymer waveguides can be a labor-intensive process. Furthermore, this method only allows the use of multimode waveguides, and coupling is restricted to a narrow angular range [9].

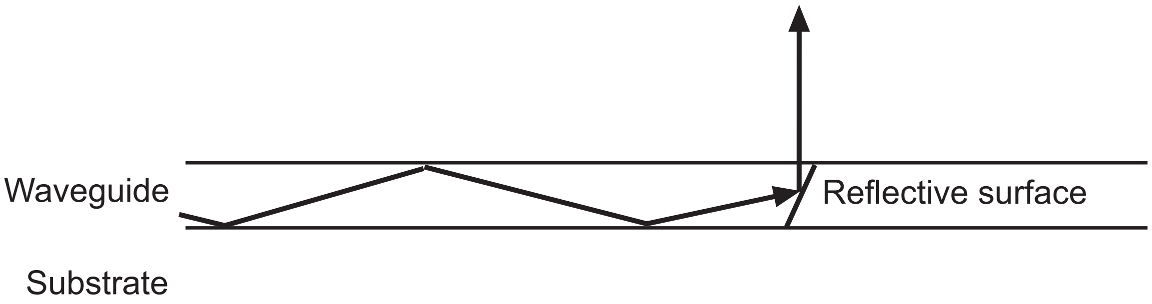

Figure 1.4: Diagram of a reflective coupler

1.1.3.3 Diffractive Couplers

Diffraction gratings can produce coupling into and out of optical waveguides. They are compact and flat, making them compatible with the planar device technology found in microelectronics. They can be designed to focus light that is being coupled out, and in reciprocal fashion to couple in efficiently light from divergent sources. An important consideration for grating couplers is preferential coupling. Since gratings in general diffract light into multiple orders, it is important in making an efficient coupler to maximize the power that is diffracted in the desired direction. The ratio of the power coupled in the desired direction to the total out-coupled power is called the preferential coupling ratio.

Surface-Relief Grating Couplers: Surface-relief gratings consist of a periodic variation in the surface of a material. A diagram of a surface-relief grating coupler is shown in Fig. 1.5a. Dakss *et al.* made the first demonstration of their use for coupling into thin-film waveguides [29]. These couplers can also perform focusing [30, 31]. In order to achieve a high preferential coupling ratio with surface-relief couplers, several configurations have been proposed. The first involves the use of a reflective layer in the substrate under the grating [32, 33]. This configuration has the disadvantage of large potential loss and more complicated fabrication, as well as more stringent tolerances on fabrication. The second configuration is that of a double grating [34–36]. Very accurate alignment of the two gratings with respect to each other is required, increasing the cost of fabrication. The third and last configuration involves the use of blazed (slanted) grating profiles. [32,37]. This configuration also presents significant challenges to fabrication due to the small periods required and the steep slant angles required on the blazed profile to achieve preferential-order coupling.

Volume Grating Couplers: Volume grating couplers consist of a periodic variation in the index of refraction of a material. A diagram of a volume grating coupler is shown in Fig. 1.5b. Their use as couplers was first demonstrated by Kogelnik *et al.* [10]. VGCs with preferential-order coupling and the combination of preferential-order coupling and focusing have been demonstrated [38–40]. VGCs with the slanted grating fringes required for preferential-order coupling have been fabricated through interferometric exposure without the use of complicated chemical processes [9]. Due to their functionality, versatility and ease of fabrication, this research focuses on VGCs.

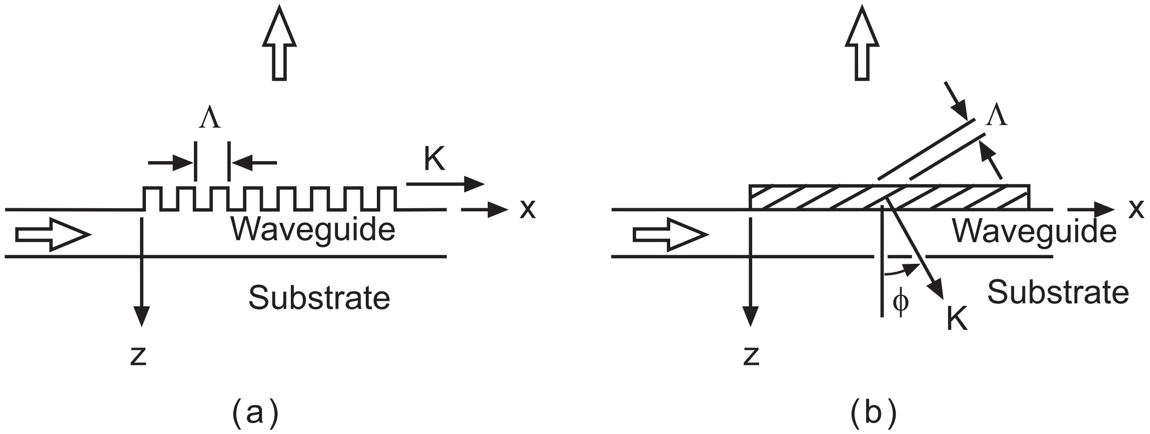

Figure 1.5: Diagrams of diffractive couplers: a) surface-relief grating coupler b) volume grating coupler.

1.1.4 Volume Grating Couplers in Optical Interconnects

Volume gratings have been proposed for use in numerous optical interconnection schemes [1,2,5,6,41–45]. The use of volume gratings in free-space optical interconnects was explored in the 1980s [1,2]. Their use has also been demonstrated in substrate-mode optical interconnects, by Chen *et al.* [7] and by Yeh *et al.* [8]. The use of thin film guided-wave optical interconnects with VGCs for in and out-coupling has also been proposed [41,45]. Recently, VGCs fabricated with polymer-dispersed liquid crystal have demonstrated electrically switchable outcoupling [46] from polymer waveguides. Focusing, preferential-order VGCs for this application also have been demonstrated [38–40]. More recently, grating-to grating coupling between two VGCs for board-to-chip interconnects has been demonstrated [47].

1.1.5 Analysis of Volume Grating Couplers

Harris *et al.* [48] performed an approximate analysis of VGCs using a modified Born approximation, the WKB scattering approach, and the reciprocity theorem. Ulrich [49], also using reciprocity, discussed conditions for maximizing coupling efficiency in a general way, using amplitude and power relations among incident and outgoing waves for a generic coupler, without trying to determine the coupling efficiencies. Wuthrich *et al.* [50] also used a Born approximation approach to derive the coupling efficiency of VGCs recorded with guided modes. All of the above analyses were not based on rigorous solutions of Maxwell's equations in the grating region. Peng *et al.* [51] used modal analysis to present the first rigorous formulation of VGCs on waveguides, using a leaky-mode analysis for unslanted gratings interacting evanescently with TE waveguide modes and later for both TE and TM modes [52]. This analysis treated sinusoidal permittivity variations only. Ogawa and Chang [53] used a perturbation analysis to determine the maximum efficiency of Kogelnik and Sosnowski's VGC [10]. This analysis treated slanted and unslanted volume gratings for TE polarized light. Wang and DiLaura [54] performed the first theoretical analysis of a volume coupler embedded in the waveguide. They used the thin grating decomposition method along with conventional waveguide analysis to study slanted volume gratings coupling TE light, but their method was restricted to couplers with low diffraction efficiency. An improved, leaky-mode approach to modeling these embedded volume out-couplers for TE light, using a two-wave coupled-wave analysis was performed by Driemeier [55]. This method neglects higher diffracted orders, but nonetheless works well for small index modulations. Two-dimensional analysis of VGCs, extending Kogelnik's work [56], has been performed by Solymar [57,58]. More recently, rigorous three-dimensional analysis including VGCs has been formulated by Matsumoto *et al.* [59]. Also, recent papers by Wu and Glytsis show a finite-difference frequency domain analysis technique which allows the rigorous analysis of VGCs with a small number of periods and/or with finite input beams for both outcoupling [60] and incoupling [61].

1.1.6 The Effects of Polarization on Volume Grating Couplers

VGCs are polarization-sensitive devices, as pointed out by Kogelnik [10]. The efficiency of volume Bragg gratings with respect to TE and TM polarized light has been studied in some detail. Kogelnik's treatment of Bragg diffraction predicts that for TM light the effective coupling constant will be reduced by a factor of the cosine of the angle between the incident and diffracted polarizations, with respect to the effective coupling constant of TE light [56]. This difference in efficiencies has been used to design diffractive polarizing beamsplitters [62,63], optical switches [64], and polarization sensors [65]. The effects of polarization sensitivity on substrate-mode VGCs have been analyzed using Kogelnik's theory [5] and the polarization effects have been used in the design of VGCs [66]. However, it has been demonstrated that rigorous analysis is required to model accurately the differences in efficiency between the TE and TM polarizations [67]. Polarization is an important parameter in fiber networks, and compatibility with fiber transmission is an important aspect of optical interconnections, as fibers interface with optical waveguides that are part of optical interconnects. However, a systematic, rigorous analysis of the effects of polarization differences on the performance of the various configurations of VGCs has not been conducted before the present research [68].

1.1.7 The Effects of Wavelength on Volume Grating Couplers

The effect of wavelength on the performance of VGCs has been studied in the context of substrate mode optical interconnects [69–73]. Kogelnik's diffraction analysis [56] was used in these cases to predict the efficiency and wavelength selectivity of VGCs performing bulk diffraction of waves by total internal reflection in thick substrates (on the order of $1mm$ or more). Huang *et al.* used a pair of VGs for wavelength-division multiplexing/demultiplexing [69], while Wang *et al.* used superimposed gratings in one location for the same purpose [70]. Wang and Lin exploited the change in coupling angle corresponding to change in wavelength to design achromatic couplers [71]. Liu and Chen demonstrated a dual and four-wavelength fanout routing networks using input and output VGCs [72, 73]. More recently, a stack of four VGs was used in a substrate mode configuration to design and fabricate a planar coarse wavelength division demultiplexer [74]. An analysis of the wavelength-dependent performance of thin film guided-wave VGCs has not been conducted before the present research [75].

1.1.8 Fabrication of Volume Grating Couplers

The interferometric method of fabricating VGCs has been in use for a long time [10]. It has been used to fabricate multiple VGCs in a path-folding configuration whereas light is coupled in through one VGC and out through another in the opposite direction from which it came [11], and in a path-shifting configuration in which it is coupled in through one VGC and out through another in the same from which it came [9]. The HRF-600X photopolymer from DuPont has been used to fabricate high-efficiency VGCs on polyimide waveguides [38–40]. This material has very important features for VGC fabrication, including a high refractive index modulation (as high as 0.03), high resolution ($5000 lines/mm$), and predictable, low exposure shrinkage ($\sim 3\%$) [76, 77]. The process of grating formation in this photopolymer has been described by Piazzolla, using a diffusion model [78]. More recently, a nonlocal diffusion model in conjunction with the Rigorous Coupled-Wave Analysis (RCWA) has been proposed to refine the understanding of grating formation and to provide optimum values for exposure intensities and times and curing temperatures and times [79]. Thus far, the limitations on its use have included the need for transparent substrates and the need for waveguide materials to which the HRF-600X adheres well [9].

1.2 Research Objectives

VGCs have shown promise as efficient input/output couplers for thin-film guided-wave optical interconnects [38–40]. The main objectives of this research are to further the quantitative understanding of the performance of VGCs, and to show that they can be successfully integrated with other elements of a practical optical interconnect system. The main contributions of this research are listed below:

1. The first rigorous quantitative analysis of the polarization-dependent performance of VGCs is presented. This analysis can be applied to waveguide coupler structures with an

arbitrary number of layers.

2. The first rigorous quantitative analysis of the effect of lossy materials on the performance of VGCs is presented.

3. The first rigorous quantitative analysis of the wavelength response of VGCs is presented. A quantitative study of the effects of the index of refraction, index modulation, and waveguide/grating thickness on the wavelength-dependent performance of VGCs is also presented for the first time.

4. The first design, fabrication and testing of a polarization-independent VGC for thin-film waveguides is presented.

5. The first measurement of birefringence in the index modulation of VGCs fabricated in polymers without liquid crystals is presented.

6. The first measurement of the wavelength-dependent performance of a VGC is presented here.

7. The first demonstration of the successful integration of VGCs with polymer pillar interconnect technology and the first measurement of the coupling through polymer pillars are presented.

1.3 Thesis Overview

This thesis is centered on the analysis, design, fabrication and testing of VGCs for optical interconnects. In Chapter 2, the rigorous coupled-wave analysis combined with the leaky-mode approach (RCWA-LM), is used to analyze the performance of VGCs. Also in this chapter, the effects of polarization, wavelength, and lossy materials on the performance of VGCs are examined. In Chapter 3, the design variables, method of design, and method of fabrication used are explained.

The testing configurations and the measurements made with them to characterize the performance of VGCs for this research are presented in Chapter 4. Input and output coupling testing configurations are presented. The equipment and methods used to measure polarization and wavelength dependence are discussed.

The design, fabrication, and testing of a polarization-dependent VGC are discussed in

Chapter 5. In Chapter 6, the same is done for a polarization-independent VGC. Also in this chapter, measurements indicating the presence of birefringence in the index modulation of the fabricated polarization-independent couplers are discussed. In Chapter 7, the measurement of the wavelength response of a VGC and its comparison to the performance predicted by RCWA-LM analysis is shown.

In Chapter 8, the integration of a VGC with polymer pillars and the measurement of the performance of the coupler/pillar system are discussed. Conclusions and possible directions for future research are presented in Chapter 9.

CHAPTER 2

ANALYSIS OF VOLUME GRATING COUPLERS

The analysis of VGCs presented in this thesis is based on the rigorous coupled-wave analysis, in conjunction with a leaky-mode approach (RCWA-LM). In this chapter, the structures under analysis and the formulation used to perform the calculations are presented. The manner in which the performance of VGCs is affected by the polarization,wavelength of light, and by the lossiness of coupler materials is presented.

2.1 Analysis of Volume Grating Couplers for TE and TM Polarized Light

In this research, the two VGC structures shown in Figs. 2.1a and 2.1b are analyzed for each polarization. Both structures are based on a glass substrate and have an air superstrate. In both cases, light in the waveguide is incident (from the left) on the grating coupler. In the configuration of Fig. 2.1a, the VG is located in a layer adjacent to the high-index waveguide layer ("VG in Cover Layer" configuration). In the configuration of Fig. 2.1b, the VG is embedded in the waveguide layer ("VG in Waveguide" configuration). Guided modes supported by the coupler structure are usually leaky modes which radiate power away from the structure. This radiation constitutes the mechanism by which light is coupled out of the waveguide. The structure in Fig. 2.1a can be designed to support several leaky modes, with only one confined to the waveguide region, while the structure in Fig. 2.1b can be designed to support only the fundamental leaky mode at the design wavelength λ_o. Mathematically, the radiation can be represented by a complex propagation constant for each leaky mode. The complex propagation constant $\tilde{\beta} = \beta - j\alpha$, where β and α are both real, is calculated using the RCWA-LM [80]. This analysis of VGCs begins with the assumption of a multilayer waveguide/coupler structure such as the one shown in Fig. 2.2. The m-th layer in the structure (excluding the superstrate and substrate) is treated as a volume grating with grating vector $\vec{K}_m = K_x\hat{x} + K_{m,z}\hat{z}$. This grating vector determines the period and slant angle of the m-th grating. Homogeneous layers can be considered as special cases of gratings with zero modulation.

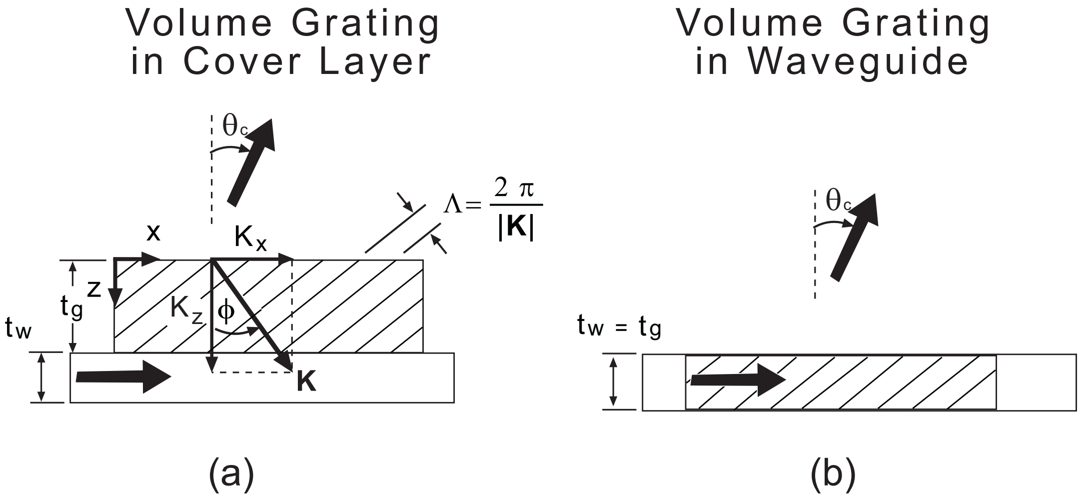

Figure 2.1: Diagrams of the two VGC configurations discussed in this thesis: (a) volume grating in the cover layer, (b) volume grating in the waveguide. The grating vector **K** as well as the period Λ and slant angle ϕ are shown. The outcoupling angle is θ_c. The thickness of the grating layer is t_g, and the thickness of the waveguide layer is t_w.

In this analysis, the fields in each region are of the form

$$\vec{U}_m = \hat{y} U_m(z,x) e^{-j\tilde{\beta}x}, \tag{2.1}$$

where $\vec{U}$ represents the $\vec{E}$ field for TE polarized light and the $\vec{H}$ field for TM polarized light. For the m-th waveguide layer (see Fig. 2.2)

$$U_m(z,x) = \sum_i S_{m,i}(z)\, e^{-j\vec{\sigma}_{m,i}\cdot\vec{r}}, \qquad m = 2, ..., M+1 \tag{2.2}$$

where $\vec{\sigma}_{m,i} = \tilde{k}_{x,i}\hat{x} - iK_{m,z}\hat{z}$, with $\tilde{k}_{x,i} = \tilde{\beta} - iK_x$, and

$$S_{m,i}(z) = \sum_j C_j^m w_{i,j}^m e^{\lambda_j^m z}, \tag{2.3}$$

where $w_{i,j}^m$ and λ_j^m are the eigenvectors and eigenvalues of the fields in the m-th layer, and C_j^m are their respective coefficients, all obtained from RCWA analysis [80]. For the superstrate region

$$\vec{U}_1 = \hat{y} \sum_i R_i\, e^{-j\vec{k}_{1,i}\cdot\vec{r}}, \tag{2.4}$$

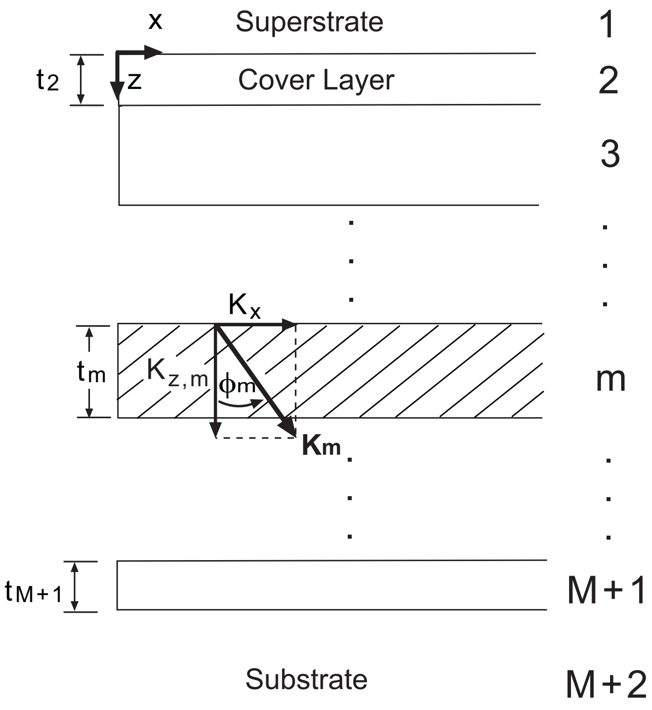

Figure 2.2: Schematic diagram for the analysis of coupler structures with an arbitrary number of layers and gratings.

where R_i are the amplitudes of the diffracted orders in the superstrate region, and the wavevectors are defined as

$$\vec{k}_{1,i} \quad = \quad \tilde{k}_{x,i}\hat{x} + \tilde{k}_{1,zi}\hat{z}, \tag{2.5}$$

where

$$\tilde{k}_{1,zi} \quad = \quad \sqrt{k_o^2 n_1^2 - \tilde{k}_{x,i}^2} \tag{2.6}$$

if $Re\{\tilde{k}_{1,zi}\} - Im\{\tilde{k}_{1,zi}\} < 0$, or

$$\tilde{k}_{1,zi} \quad = \quad -\sqrt{k_o^2 n_1^2 - \tilde{k}_{x,i}^2} \tag{2.7}$$

if $Re\{\tilde{k}_{1,zi}\} - Im\{\tilde{k}_{1,zi}\} > 0$ [81].

For the substrate [(M+2)-th layer in Fig. 2.2]

$$\vec{U}_{M+2} = \hat{y} \sum_i T_i \, e^{-j\vec{k}_{M+2,i}\cdot(\vec{r} - d\hat{z})}, \tag{2.8}$$

where $d = \sum_m t_m$, with t_m the thickness of the m-th layer, M is the total number of layers in the structure (not including the superstrate and the substrate), and T_i are the amplitudes of the diffracted orders in the substrate region. The wavevectors are

$$\vec{k}_{M+2,i} = \tilde{k}_{x,i}\hat{x} + \tilde{k}_{M+2,zi}\hat{z}, \tag{2.9}$$

where

$$\tilde{k}_{M+2,zi} = \sqrt{k_o^2 n_1^2 - \tilde{k}_{x,i}^2} \tag{2.10}$$

if $Re\{\tilde{k}_{M+2,zi}\} - Im\{\tilde{k}_{M+2,zi}\} > 0$, or

$$\tilde{k}_{M+2,zi} = -\sqrt{k_o^2 n_1^2 - \tilde{k}_{x,i}^2} \tag{2.11}$$

if $Re\{\tilde{k}_{M+2,zi}\} - Im\{\tilde{k}_{M+2,zi}\} < 0$ [81].

Using the electric and magnetic field components of the optical waves in the various regions of the structure and the electromagnetic boundary conditions, the problem can be cast as a matrix equation of the form $\overline{\overline{\overline{\mathbf{M}}}}(\tilde{\beta})\boldsymbol{V} = \mathbf{0}$, where $\boldsymbol{V} = [\boldsymbol{R}\boldsymbol{C_1} \ldots \boldsymbol{C_M}\boldsymbol{T}]^T$ and $\overline{\overline{\overline{\mathbf{M}}}}$ is a $2(M+1)N \times 2(M+1)N$ matrix, where N is the number of diffracted orders retained in the analysis. $\boldsymbol{R} = [R_{-P}, ..., R_P]$ and $\boldsymbol{T} = [T_{-P}, ..., T_P]$ are vectors of size N, where $P = (N-1)/2$. These vectors correspond to the complex amplitudes of the diffracted plane waves in the superstrate and substrate, respectively, while the $\boldsymbol{C_m}$ vectors of size $2N$ correspond to the amplitude components of the fields in the inner layers of the structure. For a non-trivial solution of this matrix equation, the determinant of $\overline{\overline{\overline{\mathbf{M}}}}$ must be zero. Thus by solving $\det\left[\overline{\overline{\overline{\mathbf{M}}}}(\tilde{\beta})\right] = 0$, where "det" denotes the determinant, $\tilde{\beta}$ can be determined. This is a numerically sensitive problem because there may be multiple $\tilde{\beta}$ solutions corresponding to various modes or non-physical modes. The Muller method [82] of finding the complex zeros of a mathematical function has been adopted to find an approximate solution. This is feasible provided an adequate initial guess is available. The real propagation constant β of the guided mode in the case of zero modulation in all layers is usually a good starting point, since the real part of $\tilde{\beta}$ is typically close to β (within $10^{-3}\mu m^{-1}$ for index modulations less than 0.05). The Muller method is much more efficient than the Sequential Quadratic Programming [83] techniques previously used [9, 68], thus vastly reducing computation times.

Once $\tilde{\beta}$ has been determined, it is used to calculate the power distribution of the radiation diffracted outside the coupler system. Since $\det\left[\overline{\overline{\mathbf{M}}}(\tilde{\beta})\right] = 0$, the components of $\boldsymbol{V} = [\boldsymbol{R}\boldsymbol{C_1} \ldots \boldsymbol{C_M}\boldsymbol{T}]^T$ can be determined only as a function of a common arbitrary constant. For simplicity, this constant can be selected to be unity. In the present case, $R_1 = 1$ (any component of $\boldsymbol{V}$ can be selected without affecting the final result). In this way the R_i and T_i amplitudes are values proportional to the first-order superstrate diffracted amplitude R_1. Then, using $\overline{\overline{\mathbf{M}}}(\tilde{\beta})\boldsymbol{V} = \mathbf{0}$ and eliminating this variable and one of the equations from the system, and using $\tilde{\beta}$ as the solution of this reduced system, relative values for all the R_i and T_i coefficients can be obtained. These coefficients are then used to calculate the relative power distribution among the propagating diffracted orders. Relative values for each Poynting vector (PV) are calculated according to

$$PV_{sup,i} = |R_i|^2 Re\{-k_{1,zi}\} \tag{2.12}$$

for reflected orders (into the superstrate), and

$$PV_{sub,i} = |T_i|^2 Re\{k_{M+2,zi}\} p \tag{2.13}$$

for transmitted orders (into the substrate), where $p = 1$ for TE and $p = n_1^2/n_{M+2}^2$ for TM polarization. Next, the relative values of non-propagating orders ($|Re\{k_{x,i}\}| > k_o n_1$ for superstrate and $|Re\{k_{x,i}\}| > k_o n_{M+2}$ for substrate orders) are set to zero. The relative power calculation is completed by normalizing the relative powers of the propagating orders with respect to their sum. The fraction of the out-coupled power that is directed into the desired order is called the preferential coupling ratio, and is designated $\eta_{\ell,i}$ [38], where ℓ can be either the superstrate (sup) or the substrate (sub), and i is the diffracted order. The resulting equation is

$$\eta_{\ell,i} = PV_{\ell,i}/(\sum_i PV_{sup,i} + \sum_i PV_{sub,i}). \tag{2.14}$$

The coupling efficiency ($CE_{\ell,i}$), defined as the fraction of the guided power P_o at the beginning of the coupler that is diffracted into the desired order after a certain length

L, can be calculated once $\tilde{\beta}$ and the power distribution are known, and it is given by [38]

$$CE_{\ell,i} = \eta_{\ell,i}(1 - e^{-2\alpha L}). \tag{2.15}$$

2.2 Analysis of Volume Grating Couplers with Lossy Materials

In the case of a lossy grating, the complex component of the propagation constant $\tilde{\beta}$ is the sum of two elements that comprise its imaginary component. One is the radiation component α that was previously discussed, and the other is the component due to loss in the material, designated α_{loss}. In order to calculate $CE_{l,i}$ in this case, $\tilde{\beta}$ is calculated separately for the same structure both with and without loss. Both calculated values for $\tilde{\beta}$ will have approximately the same real component, but their imaginary components will differ. This difference corresponds approximately to α_{loss}. When calculating the coupling efficiency of a lossy coupler, α_{loss} must be taken into account. The power in the mode is being attenuated by both effects, yet only α contributes to the out-coupling. By modifying the previous equation to take this into account,

$$CE_{\ell,i} = \eta_{\ell,i}\frac{\alpha}{\alpha + \alpha_{loss}}[1 - e^{-2(\alpha+\alpha_{loss})L}] \tag{2.16}$$

is obtained.

2.3 Polarization-Dependence of Volume Grating Coupler Performance

The performance of VGCs with “VG in the cover layer” and “VG in the waveguide” for TE and TM polarized light has been evaluated and compared using the two structures in Fig. 2.1. The waveguide material is assumed to be Ultradel 9020D, a polyimide [21], with $n = 1.56$. The grating material is DuPont’s HRF600X photopolymer, with $n = 1.50$ and an index modulation $\Delta n = 0.02$. Both structures have a glass substrate with $n = 1.4567$ and air superstrate ($n = 1$). The structure with a “VG in the cover layer” (Fig. 2.1a) has a grating layer of thickness $t_g = t_2 = 10\mu m$ and a waveguide thickness $t_w = t_3 = 0.4\mu m$. The structure with a “VG in the waveguide” (Fig. 2.1b) has $t_g = t_w = t_2 = 1.8\mu m$. The free-space wavelength used is $\lambda_o = 1\mu m$. In Fig. 2.3, the calculated normalized electric field of a TE polarized leaky wave in the "VG in the cover layer" configuration can be seen. Note the radiation into the superstrate and substrate from the leaky mode.

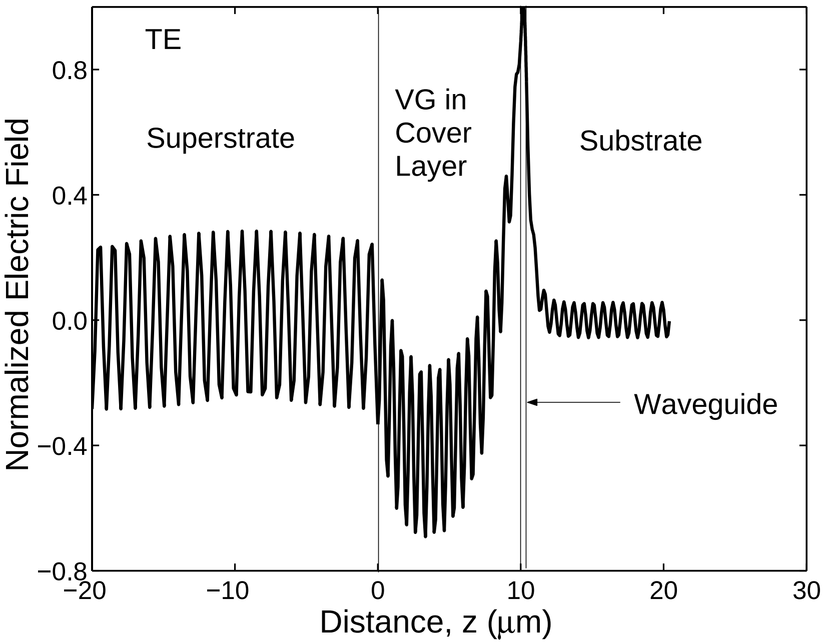

Figure 2.3: Electric field plot of leaky mode in a VG in the cover layer structure. Note the waves radiating into the superstrate and the substrate.

As expected from Kogelnik's theory [56], for angles close to normal to the surface of the structure, the coupling coefficient for TM polarized light is drastically lower than for TE light in both configurations. This is seen in Fig. 2.4 for the "VG in the cover layer" structure and in Fig. 2.5 for the "VG in the waveguide" structure. In Fig. 2.5, it is observed that the lowest coupling coefficient for TM polarized light in the structure with "VG in the waveguide" occurs 12° off normal. This corresponds to a beam angle inside the grating region of 8° off normal. By calculating the angle at which the waves inside the grating region are impinging on the grating/superstrate boundary, it can be seen that they are at an angle of 8° from the boundary, so at an out-coupling angle of 8° from normal, the lowest coupling between the diffracted and guided waves would be expected as predicted in Kogelnik's theory [56].

For angles farther from normal, of 40° or more, the coupling coefficients are comparable. The increase in the coupling coefficient with out-coupling angle for TM polarized light

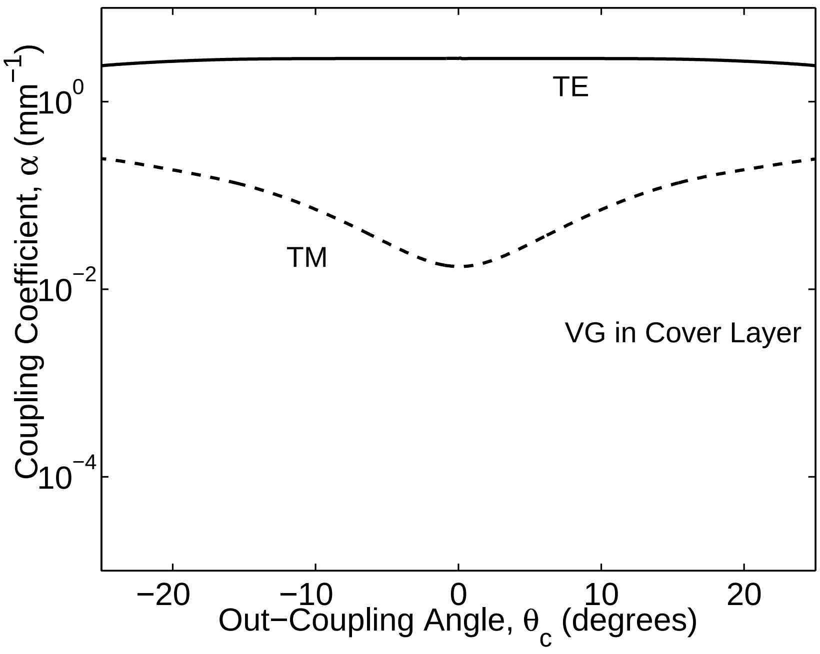

Figure 2.4: Coupling coefficient versus out-coupling angle for the VG in the cover layer structure. A minimum for TM polarization occurs close to 0°. For TE polarization, the coupling coefficient remains relatively constant as the out-coupling angle is varied.

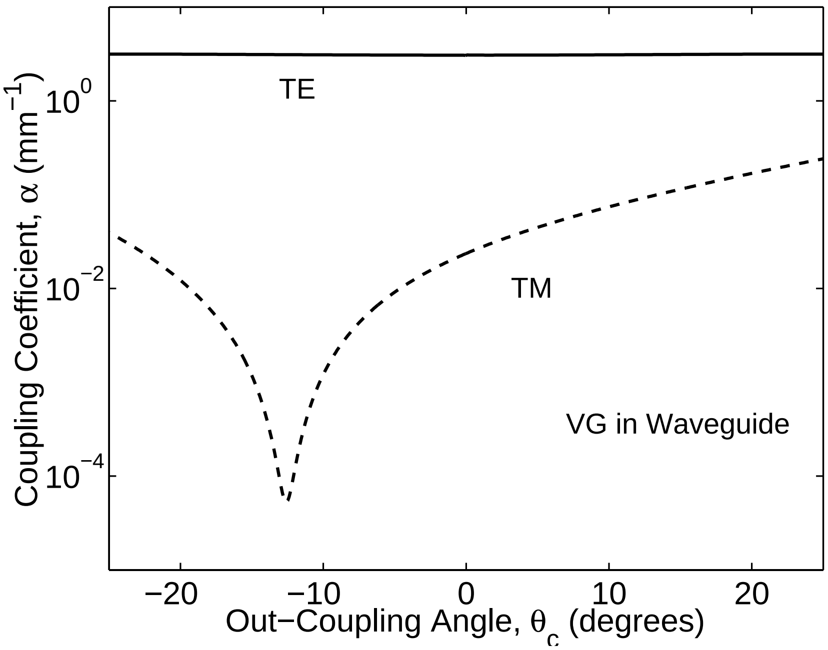

Figure 2.5: Coupling coefficient versus out-coupling angle for the VG in the waveguide structure. A minimum for TM polarization occurs at −12°. For TE polarization, the coupling coefficient remains relatively constant as the out-coupling angle is varied.

continues up to the physical limit of 90°. However, the coupling efficiency begins to degrade long before this limit, as the preferential coupling is lost and light begins to be coupled into more than one order. It can also be noted that for the configurations presented here, the coupling coefficients for "VG in the cover layer" and "VG in the waveguide" are very similar. This is because the thickness of the grating in the case of "VG in the cover layer" is larger than in the case of "VG in the waveguide." This compensates for the fact that the grating located in the waveguide interacts with more of the beam power than the grating located in the cover layer.

Figure 2.6 shows the coupling coefficients versus grating slant angles for TE polarized light for the two configurations, and here a difference between the two can be noted: the coupling coefficient for the "VG in the waveguide" structure has a much wider FWHM. This may be explained by the fact that in this case the grating located in the waveguide is thinner than the grating located in the cover layer.

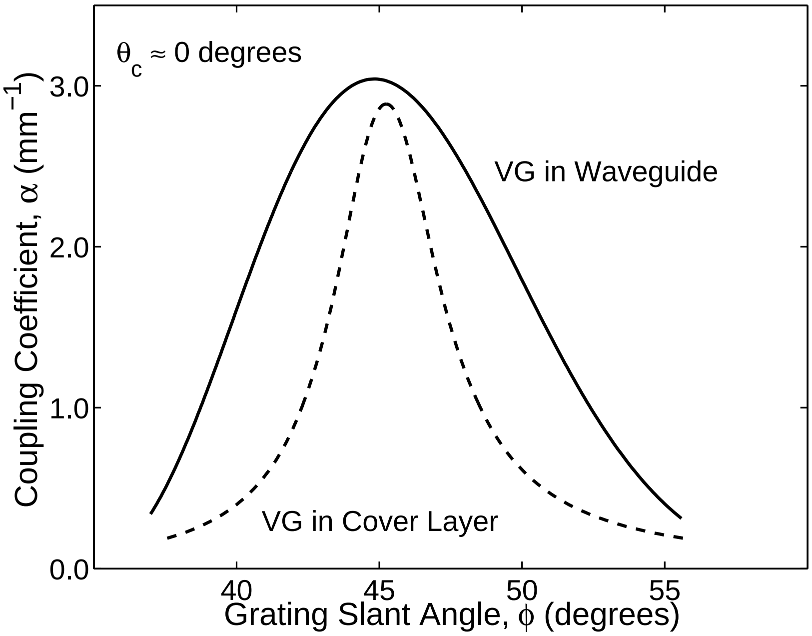

Figure 2.6: Coupling coefficient versus grating slant angle for vertical coupling for the VG in the cover layer and the VG in the waveguide configurations. The VG in the waveguide curve has a slightly higher peak and a considerably wider FWHM than the VG in the cover layer curve.

Figure 2.7 shows calculated coupling efficiencies versus out-coupling angles for TE and

TM light in the "VG in the cover layer" structure, while Fig. 2.8 does the same for the "VG in the waveguide" structure. The gratings simulated in these plots have been optimized for maximum coupling coefficient of the TM polarization. High efficiencies can be achieved for TE light for a wide variety of angles, while for TM light, comparable efficiencies are restricted to angles greater than 40°. The intersection of efficiency lines for TE and TM couplers of the same lengths suggests that a polarization-insensitive coupler working at an off-normal angle can be designed and fabricated. Figure 2.9 shows the coupling efficiency versus coupler length for a "VG in the cover layer" structure with an out-coupling angle of 46.7° and for a "VG in the waveguide" structure with an out-coupling angle of 54.4°. It can be seen that in both cases the coupling efficiencies are within 1.5 % for TE and TM polarized light. Table 2.1 shows design values and calculated performance characteristics for polarization-dependent and polarization-independent VGCs.

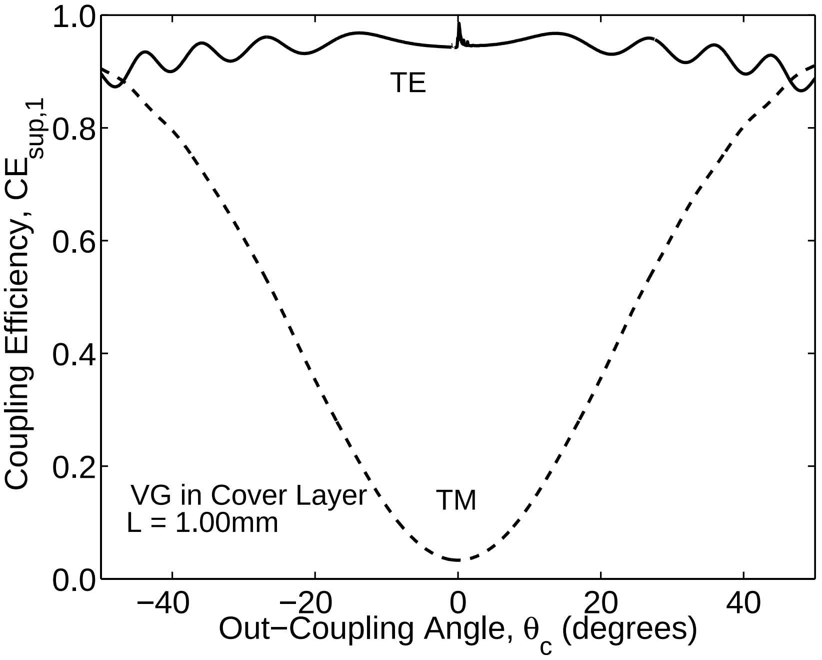

Figure 2.7: Coupling efficiency versus out-coupling angle for a VG in the cover layer structure of $L = 1mm$. Coupling efficiency for TE polarization remains higher for all angles in this range. For TM polarization, coupling efficiency with increasing out-coupling angle, reaching parity with TE polarization near $\theta_f = 46.7°$.

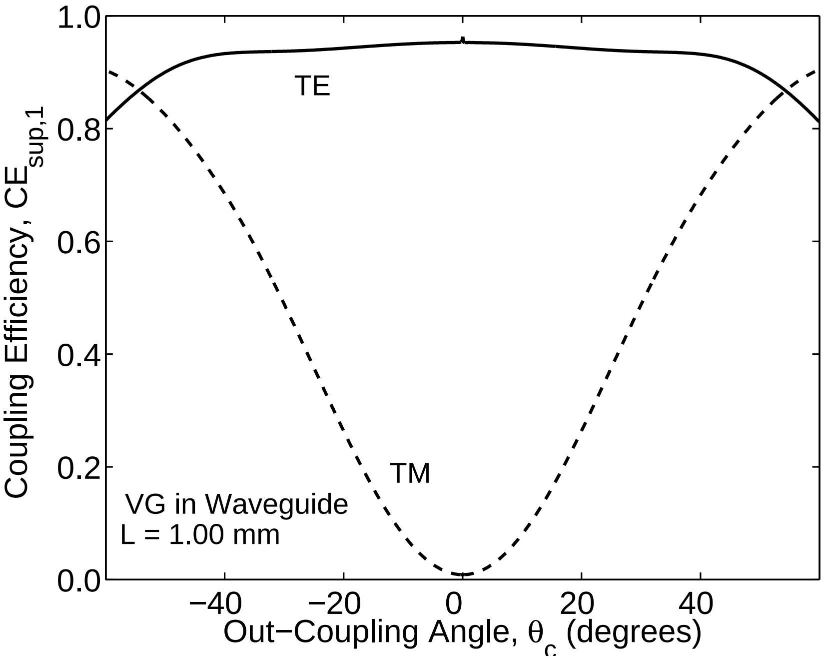

Figure 2.8: Coupling efficiency versus out-coupling angle for a VG in the waveguide structure of $L = 1mm$. Coupling efficiency for TE polarization remains higher for all angles in this range. For TM polarization, coupling efficiency with increasing out-coupling angle, reaching parity with TE polarization near $\theta_f = 54.4°$.

Table 2.1: Design Values and Calculated Performance Characteristics of $L = 1mm$ Polarization-Dependent and Polarization-Independent VGCs for $\lambda_o = 1\mu m$.

Parameter	PD VG in CL	PD VG in WG	PI VG in CL	PI VG in WG
$K_x(\mu m^{-1})$	9.55	9.34	4.88	4.22
$K_z(\mu m^{-1})$	9.47	9.40	8.26	7.93
$\Lambda(\mu m)$	0.467	0.475	0.655	0.699
$\phi(°)$	45.2	44.8	30.6	28.0
$\theta_c(°)$	−0.90	−0.09	46.7	54.4
$\alpha_{TE}(mm^{-1})$	2.886	3.042	3.331	3.582
$\alpha_{TM}(mm^{-1})$	0.018	0.004	1.090	1.015
η_{TE}	0.946	0.967	0.881	0.867
η_{TM}	0.954	0.980	0.997	0.998
CE_{TE}	0.943	0.965	0.879	0.867
CE_{TM}	0.034	0.009	0.884	0.867

PD = Polarization-dependent, PI = Polarization-independent, VG = Volume grating, CL = Cover layer, WG = Waveguide.

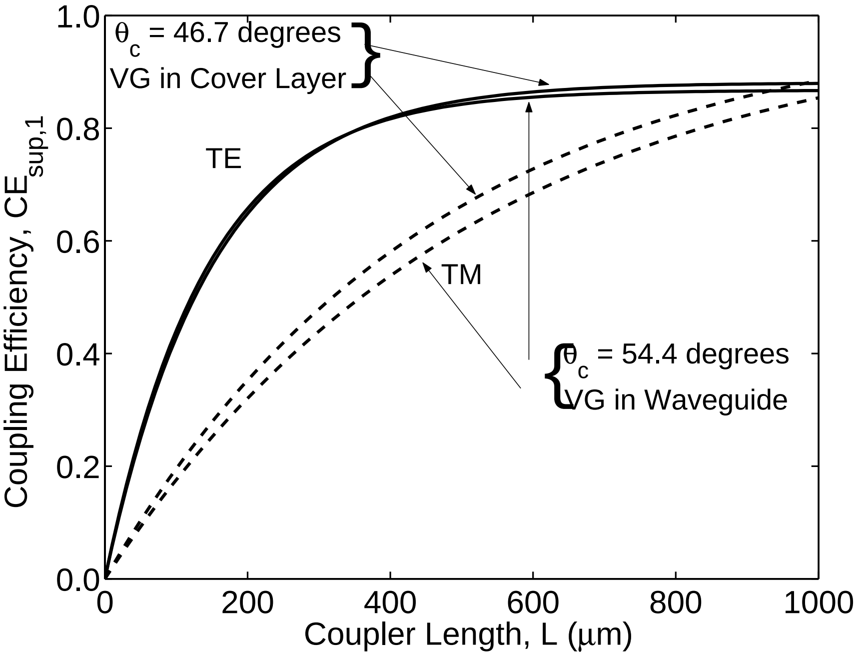

Figure 2.9: Coupling efficiency versus coupler length for couplers designed to be polarization independent in the VG in the cover layer and the VG in the waveguide configurations. The coupling coefficient is larger for TE than for TM polarization in both cases, which explains why TE coupling efficiencies saturate faster.

2.4 The Effect of Loss on Volume Grating Coupler Performance

To examine the effects of loss, coupling efficiencies for vertical out-coupling in both configurations when assuming lossless gratings versus gratings with $5dB/cm$ loss, as estimated for the DuPont HRF 600X [84], have been considered. Figure 2.10 shows the coupling efficiencies of the lossless and lossy VGCs for the case of a "VG in the waveguide" structure. It can be observed that the difference between the two is less than 3%. This indicates that the effect of loss is small compared to the effect of the coupling. The effects of loss are even smaller in the case of a "VG in the cover layer" structure, where the difference in CE is less than 0.3%.

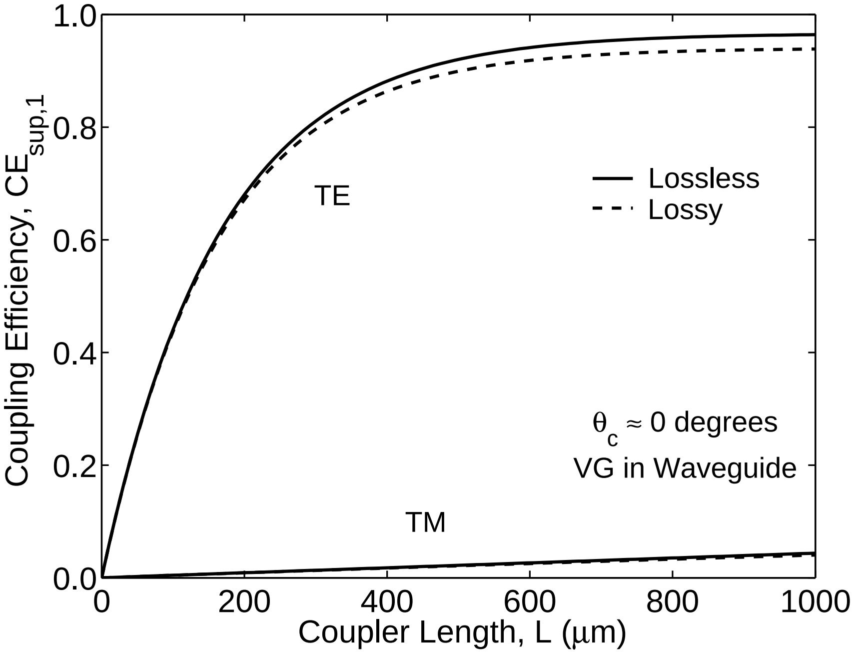

Figure 2.10: Coupling efficiency versus coupler length for lossless and lossy VGCs in the VG in the waveguide configuration. The small effect of absorption losses in the coupler material can be seen. Polarization-dependent coupling is also clear since $\theta_f \approx 0°$.

2.5 The Wavelength Dependence of Volume Grating Coupler Performance

To examine the wavelength dependence of VGC performance, the two VGC structures shown in Figs. 2.1a and 2.1b are analyzed for a range of wavelengths around their design wavelength of $\lambda_o = 1\mu m$ [75]. As in the previous sections, the waveguide material is taken to be Ultradel 9020D, a polyimide, with $n = 1.56$. The grating material is DuPont HRF600X photopolymer, with $n = 1.50$ and an index modulation of $\Delta n = 0.02$. Both structures have a glass substrate with $n = 1.4567$ and air superstrate ($n = 1$). The structure with a "VG in the cover layer" (Fig. 2.1a) has a grating layer thickness $t_g = 10\mu m$ and a waveguide thickness $t_w = 0.4\mu m$. The structure with a "VG in the waveguide" (Fig. 2.1b) has $t_g = t_w = 1.8\mu m$ and its waveguide/grating material is the DuPont HRF600X photopolymer. In both cases, the waveguide thicknesses (t_w) have been chosen such that the structures will support only one waveguide mode.

Outcoupling at 0° and at 45° for TE and TM polarized light for each of the two structures described above is considered. The design of the gratings is based on the fundamental TE mode of each waveguide, and the resulting diffraction performance for the fundamental TE and TM modes is described.

2.5.1 Wavelength-dependence in the "VG in the cover layer" configuration

Figure 2.11 shows the CE vs. λ for TE and TM polarized light for the "VG in the cover layer" configuration with $\theta_c = 0°$ and coupler lengths $L = 100\mu m$ and $L = 500\mu m$. The $L = 100\mu m$ length was chosen to illustrate partial outcoupling of the light, and $L = 500\mu m$ was chosen to illustrate nearly complete outcoupling of the light. For $L = 100\mu m$, the magnitude of the wavelength response for TM polarized light is relatively small, due to the small coupling angles [68]. For $L = 500\mu m$, the magnitude of the TM response is larger, although still weaker than the corresponding TE response. Figure 2.12 shows the CE vs. λ with $\theta_c = 45°$ for the same configuration and the same two lengths. The cutoff in the wavelength response seen close to $\lambda = 0.64\mu m$ for both polarizations is due to the fact that for this and shorter wavelengths, the resulting diffracted beam has a wavevector magnitude larger than the allowed wavevector magnitude in the superstrate ($\beta(\lambda) - K_x \geq k_o n_c$) and the beam is therefore totally internally reflected at the superstrate/grating interface. The magnitude of the wavelength response for TM polarized light is comparable to that for TE polarized light in this case, as is expected for large coupling angles [68]. It must be noted that in both cases the VGC exhibits a very wide wavelength response, with a FWHM (in the case of $\theta_c = 0°$, $L = 500\mu m$, and TE polarization) of $305nm$. The length of the device has a significant effect on the width of the bandpass. For $\theta_c = 0°$, $L = 100\mu m$, and TE polarization, the FWHM is $178nm$. For a similar grating, but with bulk diffraction, the FWHM of the wavelength bandpass would be much narrower, less than $10nm$. The much wider wavelength bandpass in the case of the VGC configuration illustrates the difference between the leaky-mode interaction of the VGC and the bulk diffraction of an incident wave by a volume grating.

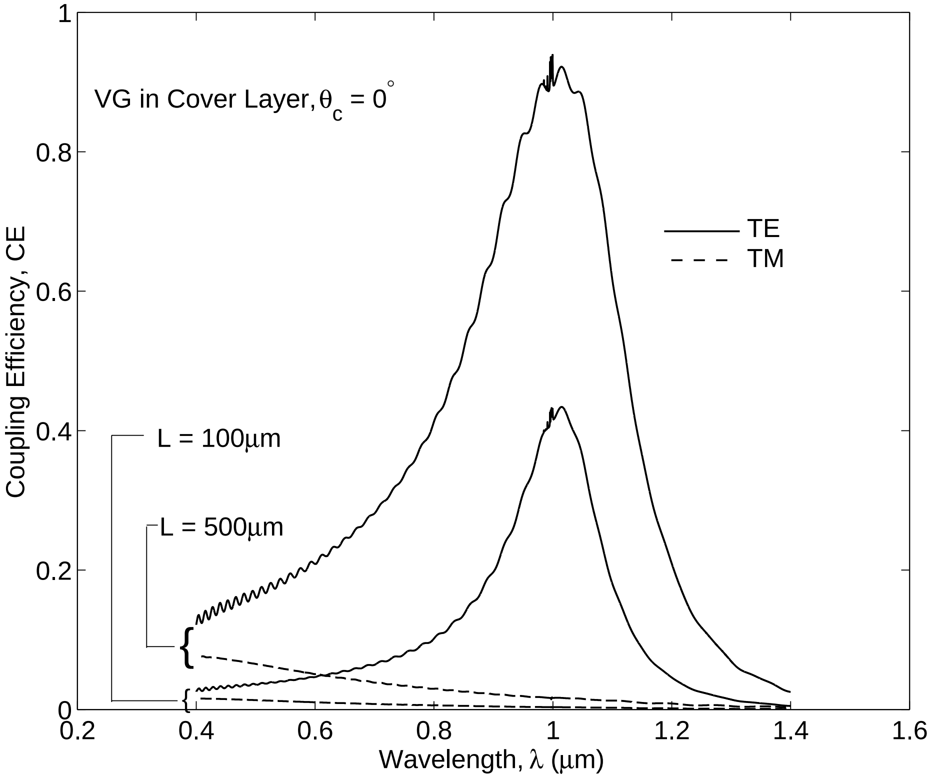

Figure 2.11: Coupling efficiency versus wavelength for TE and TM polarized light in the "VG in the cover layer" structure, with normal outcoupling for the design wavelength $\lambda_o = 1\mu m$.

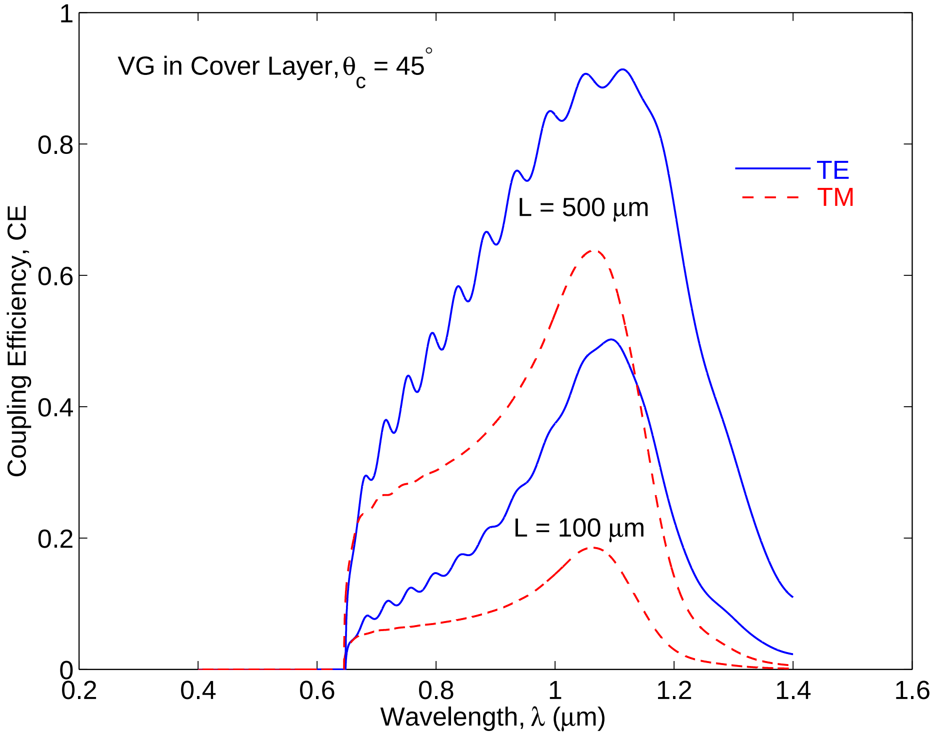

Figure 2.12: Coupling efficiency versus wavelength for TE and TM polarized light in the “VG in the cover layer” structure, with outcoupling at 45° for the design wavelength $\lambda_o = 1\mu m$.

2.5.2 Wavelength-dependence in the "VG in the waveguide" configuration

Figure 2.13 shows the CE vs. λ for TE and TM polarized light for the "VG in the waveguide" configuration with $\theta_c = 0°$ and coupler lengths $L = 100\mu m$ and $L = 500\mu m$. The TM characteristic has two peaks in this case, due to the trade-off between proximity to the Bragg condition and angular distance between the incident and diffracted waves in the VGC, both of which are major determinants of its strength. Figure 2.14 shows the CE vs. λ with $\theta_c = 45°$ for the same polarizations and lengths. The cutoff in the wavelength response seen close to $\lambda = 0.64\mu m$ for both polarizations is the result of the same conditions described above for the "VG in the cover layer" configuration. It must be noted that in both cases the VGC exhibits an even wider wavelength bandpass than in the "VG in the cover layer" configuration, with a FWHM (in the case of $\theta_c = 0°$, $L = 500\mu m$, and TE polarization) of $525nm$.

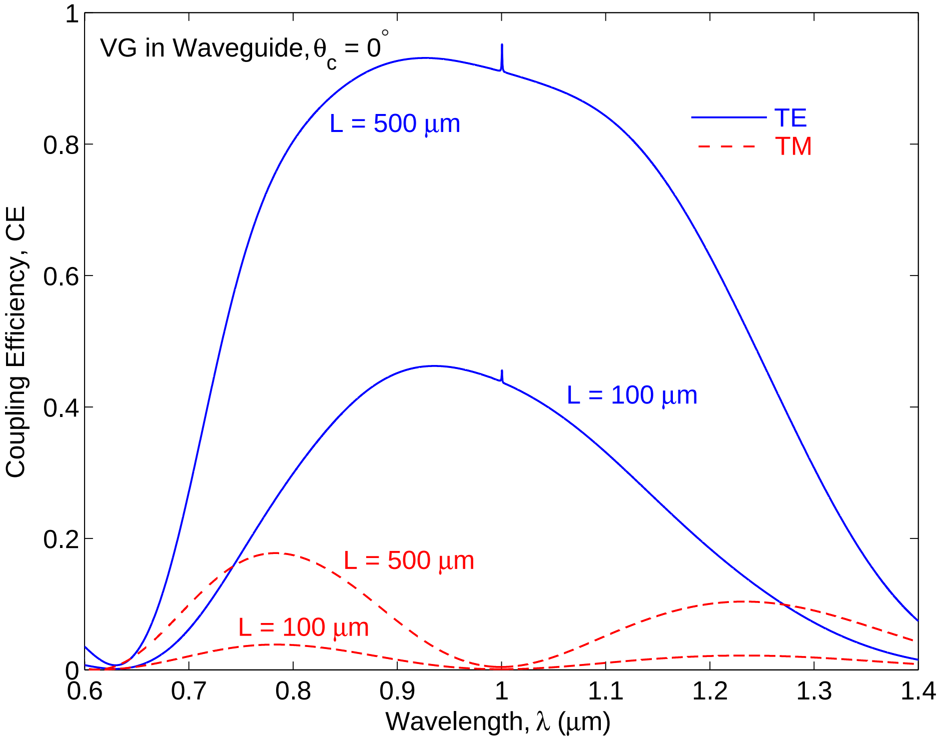

Figure 2.13: Coupling efficiency versus wavelength for TE and TM polarized light in the "VG in the waveguide" structure, with normal outcoupling for the design wavelength $\lambda_o = 1\mu m$.

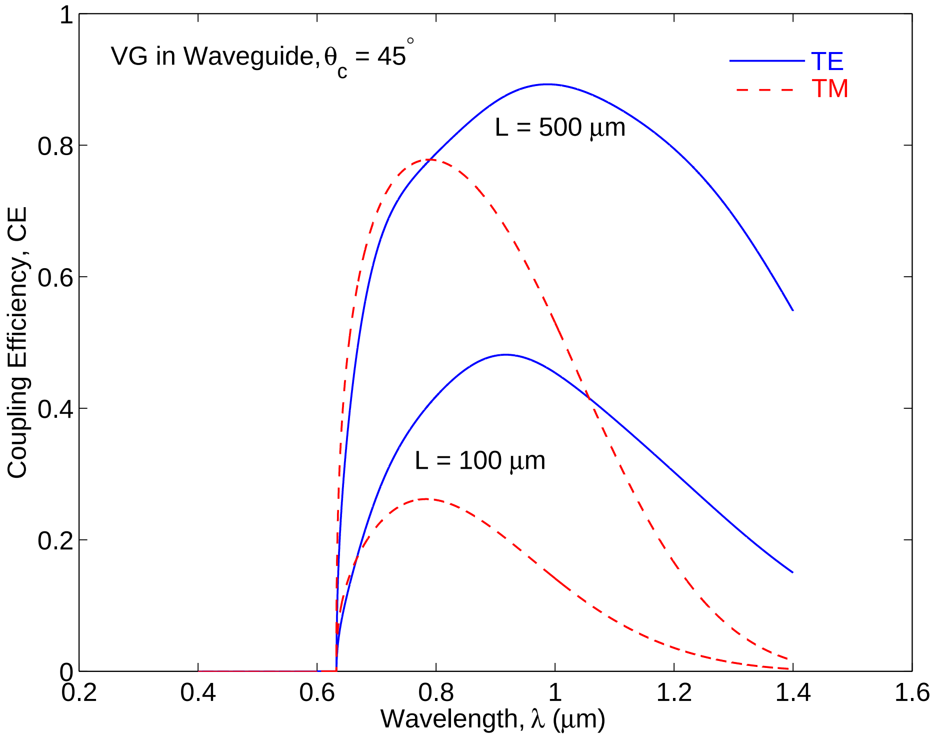

Figure 2.14: Coupling efficiency versus wavelength for TE and TM polarized light in the "VG in the waveguide" structure, with outcoupling at 45° for the design wavelength $\lambda_o = 1\mu m$.

2.5.3 Effects of index modulation, waveguide index, and grating thickness

In order to understand how the wavelength response of VGCs can be made narrower or broader, the effects of varying several physical parameters of the VGCs discussed above have been studied. The wavelength sensitivity of VGCs can be affected by several factors: the index modulation of the volume grating, the relative index of the waveguide and grating in the "VG in the cover layer" configuration, the thickness of the waveguide and of the grating in the "VG in the cover layer" configuration, and the thickness of the waveguide/grating layer in the "VG in the waveguide" configuration. The effects of the index modulation for both configurations, the effect of the waveguide index for a fixed grating index for the "VG in the cover layer" configuration, and the effect of the thickness of the waveguide/grating layer in the "VG in the waveguide" configuration have been studied. In order to make meaningful comparisons between couplers, the CEs of couplers of various lengths but with very similar CEs ($\sim 90\%$) are plotted side-by-side.

2.5.3.1 Effect of index modulation

Figure 2.15 shows plots of CE vs. λ for VGCs in the "VG in the cover layer" configuration of coupler length $L = 500\mu m$ for the original index modulation $\Delta n = 0.02$ and $L = 50\mu m$ for $\Delta n = 0.06$. The FWHM widths of the two structures are similar, with the first being $305nm$, and the second one $282nm$ (7.5% narrower). Thus it can be seen that for the "VG in the cover layer" configuration, the index modulation has a minor effect on the width of the wavelength bandpass for couplers with similar CEs.

Figure 2.16 shows plots of CE vs. λ for VGCs in the "VG in the waveguide" configuration of coupler length $L = 500\mu m$ for $\Delta n = 0.02$, and $L = 50\mu m$ for $\Delta n = 0.06$. The FWHM bandpass widths of the two structures are similar, with the first being $525nm$, and the second one $500nm$ (4.8% narrower). Thus it can be seen that for the "VG in the waveguide" configuration, the effect of the index modulation on the width of the wavelength bandpass is small for couplers with similar CEs.

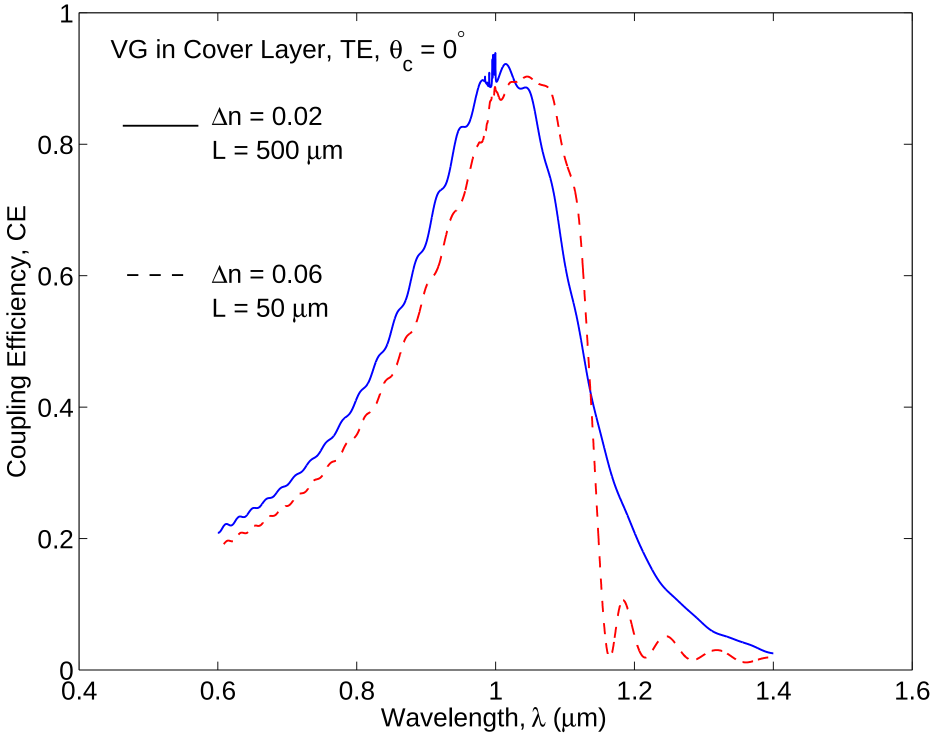

Figure 2.15: Coupling efficiency versus wavelength for TE polarized light in the "VG in the cover layer" structure, with normal outcoupling for the design wavelength $\lambda_o = 1\mu m$. The structure with $\Delta n = 0.06$ has a slightly narrower FWHM bandpass than the original structure with $\Delta n = 0.02$.

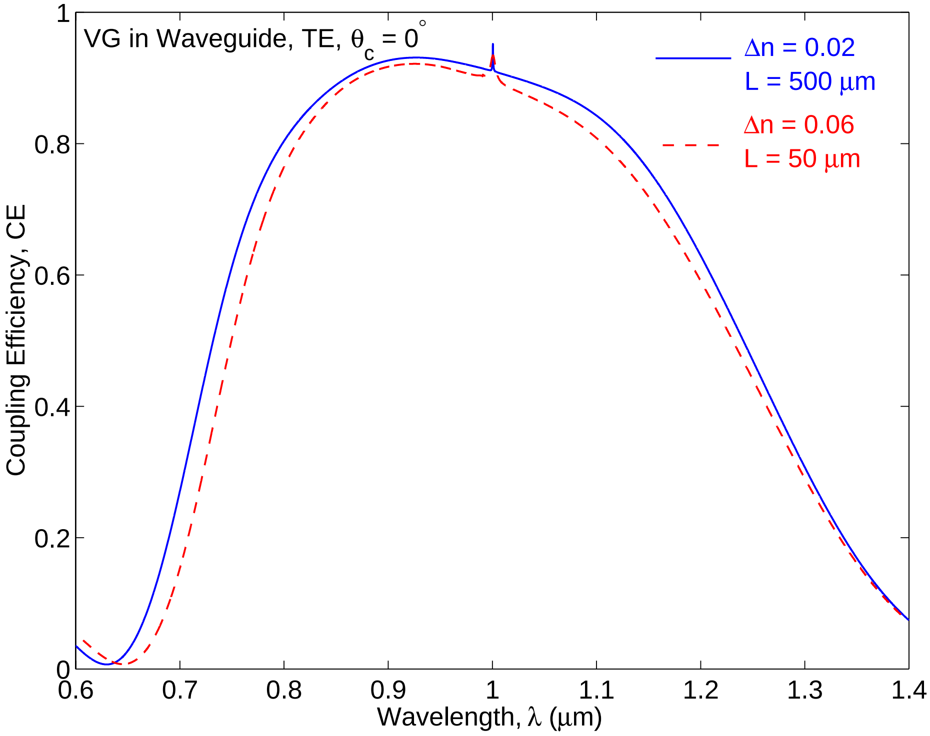

Figure 2.16: Coupling efficiency versus wavelength for TE polarized light in the "VG in the waveguide" structure, with normal outcoupling for the design wavelength $\lambda_o = 1\mu m$. The structure with $\Delta n = 0.06$ has a slightly narrower FWHM bandpass than the original structure with $\Delta n = 0.02$.

2.5.3.2 Effect of waveguide index in the "VG in the cover layer" configuration

Figure 2.17 shows plots of CE vs. λ for VGCs in the "VG in the cover layer" configuration of lengths $L = 500\mu m$ for the original waveguide index $n = 1.56$ and $L = 300\mu m$ for a waveguide index $n = 1.55$. The second coupler, with a FWHM of $205nm$, has a 33% narrower bandpass than the original coupler. Although this is still a considerably wide wavelength bandpass, this indicates that changes in the index of refraction of the waveguide have a relatively strong effect on the wavelength response in the "VG in the cover layer" configuration. This indicates that the index difference between waveguide and coupler can be optimized to obtain narrower or wider wavelength responses.

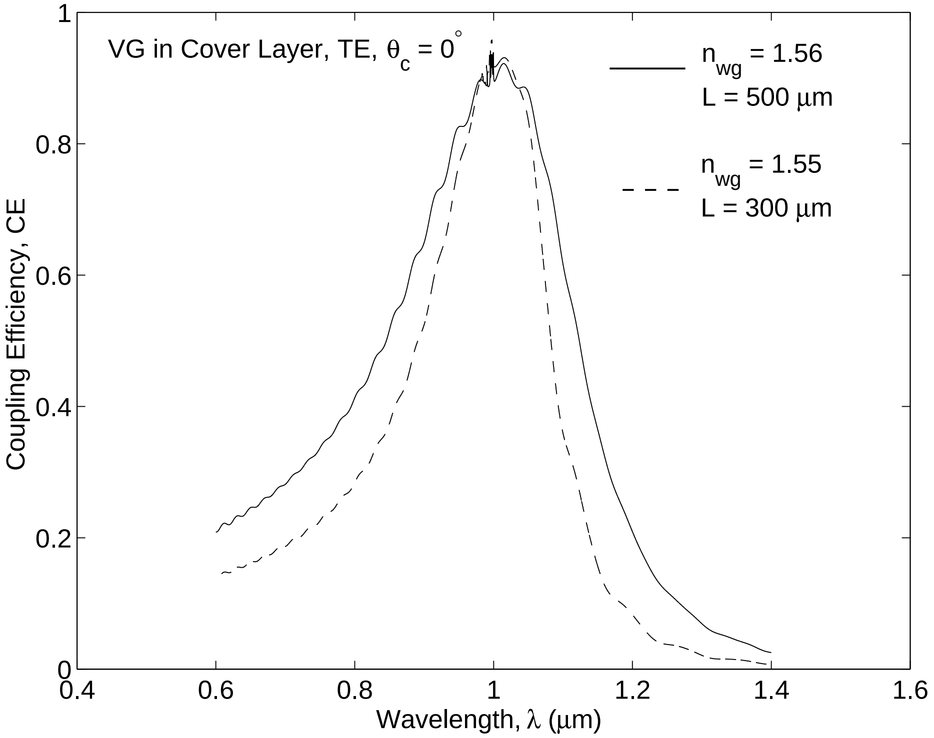

Figure 2.17: Coupling efficiency versus wavelength for TE polarized light in the "VG in the cover layer" structure, with normal outcoupling for the design wavelength $\lambda_o = 1\mu m$. The structure with $n_{wg} = 1.55$ has a significantly narrower FWHM bandpass than the original structure with $n_{wg} = 1.56$.

2.5.3.3 Effect of waveguide/grating thickness in the "VG in the waveguide" configuration

To illustrate the effect of the waveguide/grating thickness in the "VG in the waveguide" configuration, the CE vs. λ for volume gratings of various thicknesses are plotted. In the case of "VG in the cover layer," the effect of the thickness is not expected to be as significant since beyond a given thickness (depending on the thickness and index of the waveguide), the "effective thickness" of the grating that interacts evanescently with the leaky mode becomes fixed. Figure 2.18 shows plots of CE vs. λ for VGCs in the "VG in the waveguide" configuration of length $L = 500\mu m$ for the original waveguide/grating thickness $t_{wg} = t_g = 1.8\mu m$, $L = 300\mu m$ for $t_{wg} = t_g = 3\mu m$, and $L = 150\mu m$ for $t_{wg} = t_g = 6\mu m$. The respective FWHM bandpasses are $525nm$, $338nm$ (35% lower), and $173nm$ (67% lower). The wavelength bandpass becomes significantly narrower with increasing thickness. This is consistent with the behavior of volume gratings in bulk diffraction, where thicker gratings have a narrower wavelength bandpass.

2.6 Summary

In this chapter, the RCWA-LM method of analysis used for examining the performance of VGCs was presented. The first rigorous quantitative analysis of the angle-dependent polarization dependence of VGCs has been performed. It is shown that both polarization-dependent and polarization-independent VGCs can be designed. The first quantification of the effects of lossy materials on the performance of VGCs has also been performed. It has been found that for grating material with $5dB/cm$ loss, as estimated for the DuPont HRF 600X [84], the effect of the loss is small.

The wavelength-dependence of VGC performance has also been examined in a rigorous, quantitative manner for the first time. VGCs have been found to have much larger FWHM bandpasses than similar volume gratings display in bulk diffraction configurations. The effects of the waveguide index of refraction, the grating index modulation and the waveguide/grating thickness on the bandpass width have also been studied. It has been found that the waveguide/grating thickness in the "VG in the waveguide" configuration has

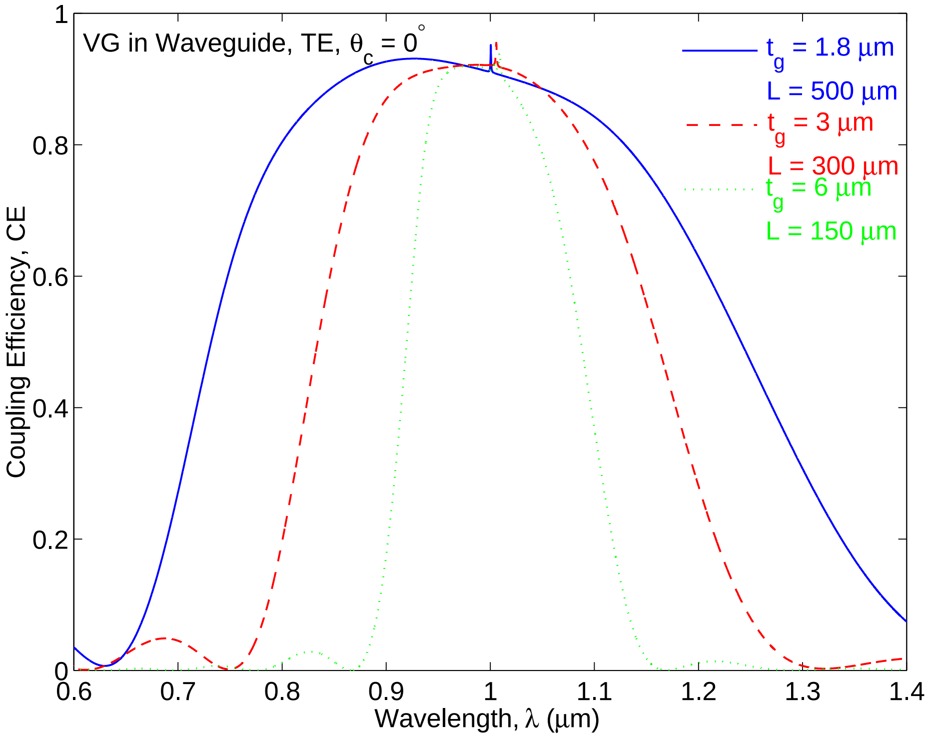

Figure 2.18: Coupling efficiency versus wavelength for TE polarized light in the "VG in the waveguide" structure, with normal outcoupling for the design wavelength $\lambda_o = 1\mu m$. The structures with $t_{wg} = 3\mu m$ and $t_{wg} = 6\mu m$ have significantly narrower FWHM bandpass than the original structure with $t_{wg} = 1.8\mu m$.

a strong effect on the wavelength bandpass, while the index modulation has a very weak effect on the wavelength bandpass of VGCs.

CHAPTER 3

DESIGN AND FABRICATION OF VOLUME GRATING COUPLERS

In this chapter, the methods employed to produce the VGCs described throughout this dissertation are described. The design method to obtain grating vectors for a given structure is presented. Also, a detailed fabrication procedure for VGCs is presented, including the design of the fabrication configuration, its alignment, sample preparation, exposure process and curing.

3.1 Grating Vector Design

Given the indices of refraction of the substrate, waveguide and grating layers, and the superstrate, as well as the thicknesses of the waveguide and grating layers, the desired grating vector components can be determined once the outcoupling angle is chosen.

The outcoupling angle θ_c is given by

$$\theta_c \quad = \quad \arcsin(\frac{\beta - K_x}{k_o n_{sup}}). \tag{3.1}$$

The value of K_x is thus set for a given β (which in turn depends on the structure parameters) and outcoupling angle.

Since the K_x component of the grating vector is used to determine the outcoupling angle, only the K_z component is left to optimize the strength of the coupling [9]. A very good approximation to the value of K_z that optimizes coupling is given by what can be called in this case an Guided Wave Bragg Condition (GWBC). This differs from the well-known Bragg condition for bulk diffraction in that the incident wave in this case is the mode guided in the waveguide. Figure 3.1 shows a diagram of the GWBC. The equation describing the GWBC is

$$K_z \quad = \sqrt{(k_o n_g)^2 - (\beta - K_x)^2}. \tag{3.2}$$

The HRF-600X material used for grating fabrication in this dissertation incurs a shrinkage of $\delta = 3\%$ during exposure and curing. This does not noticeably affect the K_x component of the grating because of its large dimensions in the plane. However, the K_z component is affected, and after exposure and curing, $K_z = K_{z,orig}/(1-\delta)$, where $K_{z,orig}$ is the originally recorded K_z component. Therefore, pre-compensation is needed for this shrinkage. This is accomplished by recording $K_{z,orig}$ to obtain K_z as the final result.

This procedure can be used to design couplers with any outcoupling angle. It will be used in subsequent chapters in the design of polarization-dependent and polarization-independent couplers.

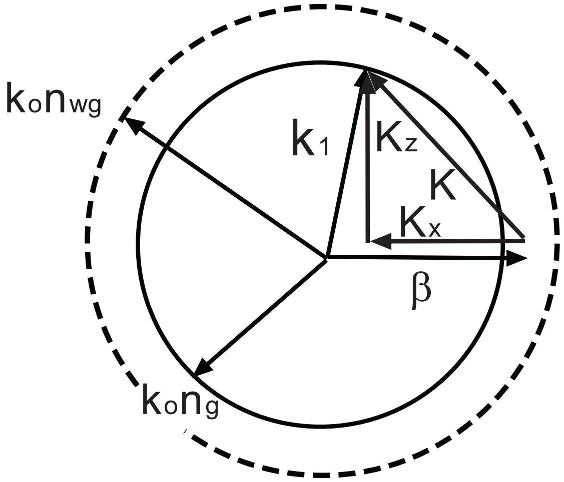

Figure 3.1: The guided wave Bragg condition (GWBC).

3.2 Volume Grating Coupler Fabrication

In this section all the phases of grating fabrication are described. First, the design of the interferometric recording configuration used to fabricate the gratings is presented. Next, the alignment procedure for the recording configuration is covered. Then, the sample preparation and recording are described. Finally, the post-exposure curing of the VGCs is presented.

3.2.1 Grating Recording Configuration Design

In order to fabricate the VGCs described in this research, the interferometric recording configuration shown in Fig. 3.2 is used. Light from a single-line $363.8nm$ laser is spatially filtered and then collimated to obtain a uniform phase-front. The light is then redirected to a polarizing beamsplitter which is preceded by a first half-wave plate and then followed by another half-wave plate. This configuration produces two beams whose power ratio can be accurately controlled. These two beams are then redirected with mirrors toward the recording sample. A prism must be placed in front of the sample in order to be able to achieve the angles between the beams that are required to produce the K_x and K_z values discussed above. Anti-reflection coated fused silica prisms are used for this purpose. Finally, another prism is placed behind the sample in order to minimize reflections from the sample-air interface that could affect the pattern being recorded. A photograph of the interferometric recording configuration is shown in Fig. 3.3. With fixed recording wavelength and refractive indices of the samples and prisms, the angle between the two recording beams and the angle of rotation of the sample (with respect to these two beams) that produces the required K_x and K_z can be determined. First, the wavevector components of the two interfering beams required to produce the grating vector $K = K_x + K_z = k_{1,w} - k_{2,w}$ are calculated, where $k_{1,w}$ and $k_{2,w}$ are the wavevectors of the two writing beams.

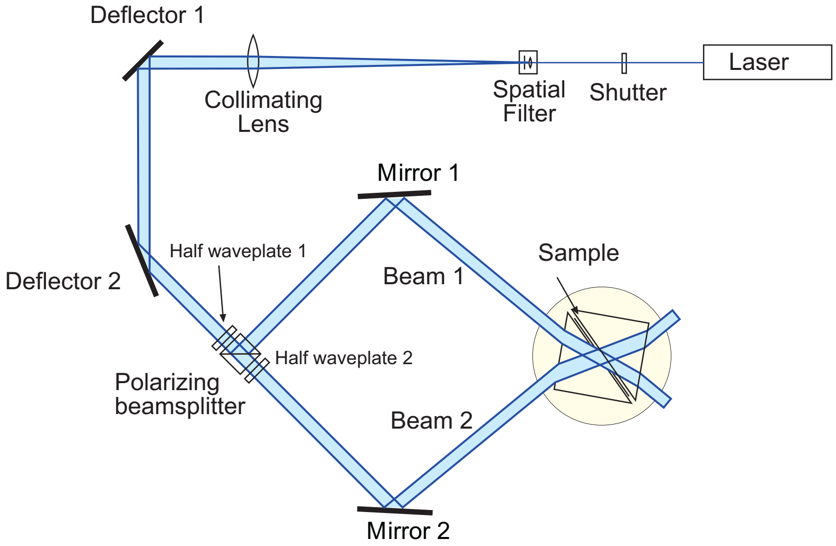

Figure 3.2: Diagram of the grating recording configuration.

From the above equation, it is surmised that

$$K_x = k_{x1,w} - k_{x2,w}, \tag{3.3}$$

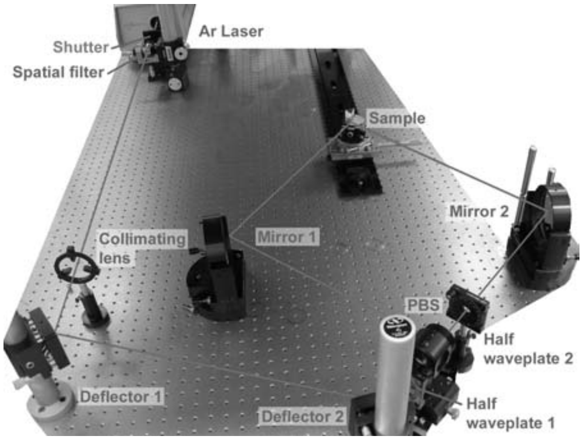

Figure 3.3: Photograph of the grating recording configuration. The path of the laser beam has been traced over the image.

and

$$K_z \quad = \quad k_{z1,w} - k_{z2,w}. \tag{3.4}$$

Is is also known that $|\vec{k}_{1,w}| = |\vec{k}_{2,w}| = k_{o,w}n_{g,w}$, so

$$k_{o,w}^2 n_{g,w}^2 \quad = \quad k_{x1,w}^2 + k_{z1,w}^2, \tag{3.5}$$

and

$$k_{o,w}^2 n_{g,w}^2 \quad = \quad k_{x2,w}^2 + k_{z2,w}^2. \tag{3.6}$$

With these four equations and with the design values of K_x, K_z, for the recording wavelength of $\lambda_w = 363.8nm$ and index of the grating material at the recording wavelength of $n_{g,w} = 1.535$ [9], the following wavevectors are determined: $k_{x1,w}, k_{z1,w}, k_{x2,w}$, and $k_{z2,w}$.

From these wavevectors, the incidence angles of the recording beams are

$$\theta_{g,1} \quad = \quad \arctan(\frac{k_{x1,w}}{k_{z1,w}}), \tag{3.7}$$

and

$$\theta_{g,2} \quad = \quad \arctan(\frac{k_{x2,w}}{k_{z2,w}}). \tag{3.8}$$

By applying Snell's Law at the grating-air interface, it is found that sufficiently oblique angles of incidence in the grating material cannot be produced from air. Thus, a prism is used so that the beams with the necessary incidence angles can impinge on the sample. A right angle, fused silica prism, with an anti-reflection coating, is used. The index of the prism at the recording wavelength $\lambda_w = 363.8nm$ is $n_p = 1.47$. Figure 3.4 shows a diagram of the air-prism-grating configuration. Applying Snell's Law at the grating-prism interface, the needed beam angles in the prism, $\theta_{p,1} = \arcsin[\sin(\theta_{g,1})n_{g,w}/n_p]$ and $\theta_{p,2} = \arcsin[\sin(\theta_{g,2})n_{g,w}/n_p]$, are obtained. From the geometry of the prism and Snell's Law, the following angles for the air-prism interface are obtained: $\theta_{air,1} = \arcsin[n_p \sin(\theta_{p,1} - 45°)]$ and $\theta_{air,2} = \arcsin[n_p \sin(45° - \theta_{p,2})]$. The sum of these two angles is the total angle between the two beams, $\Delta\theta = \theta_{air,1} + \theta_{air,2}$, while the difference between the two is the rotation angle of the sample with respect to the bisector of the two beams, $\psi = (\theta_{air,1} - \theta_{air,2})/2$.

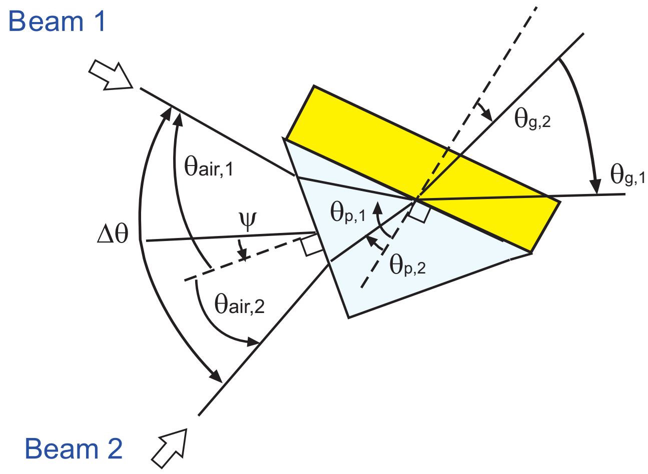

Figure 3.4: Diagram of the air-prism-grating configuration. Use of the prism allows the recording of gratings with slant angles that are not possible with an air-grating interface alone.

3.2.2 Grating Recording Configuration Alignment

Once the proper design of the recording configuration has been determined, the alignment of the recording configuration and the recording of the grating can be accomplished. The alignment of the recording configuration is a sensitive process which must be carried out carefully. The alignment procedure is as follows:

With the laser on, the spatial filter is positioned and adjusted to get good throughput in a straight path to Deflector 1 in Fig. 3.2. The collimating lens is put in place and a collimation tester is used to verify that the beam is collimated. Deflector 1 is used to direct the collimated beam towards Deflector 2. Stiff paper cards are used to mark the center lines of both deflectors. Then Deflector 2 is adjusted to ensure that the beam is aimed at the center line of Mirror 2. Then Deflector 2 is adjusted vertically to ensure that the beam is horizontal. The first half-wave plate is placed in the path of the beam while verifying that the position of the beam on Mirror 2 is unaffected. Then, the polarizing beamsplitter (PBS) is placed in the path of beam and turned so that center of Beam 1 is on the center line of Mirror 1. After checking that the center of Beam 2 (the original beam) is still in place, the horizontal path of both beams is verified and the PBS or Deflector 2 are adjusted if necessary. The next step is to place the second half-wave plate between the PBS and Mirror 2. The path of Beam 2 must remain unaffected after this step. Then the second half-wave is rotated until its output is TE polarized (same as Beam 1).

To maximize the index modulation of the grating, the ratio of the powers of the two beams incident on the sample must be close to unity [78]. In order to ensure this, the ratio of the powers in the beams must be adjusted to compensate for the different angles at which they are incident on the sample. The ratio is $R = P_1/P_2 = \cos\theta_{g,2}/\cos\theta_{g,1}$, where P_1 and P_2 are the measured powers in Beam 1 and Beam 2, respectively. To adjust the power ratio, the power in each beam is measured and the first half-wave plate is adjusted iteratively until the proper ratio is obtained.

To continue the alignment procedure, a mirror slide is placed in front of the hypotenuse of the prism on the rotation stage. Then the translation stage is adjusted so that the center at the base of the prism is at the center of the rail. Next, the marker from Mirror 1 is removed and the path of Beam 2 is blocked before it reaches Mirror 2. The mirror slide is initially placed at a longitudinal distance between the mirrors and the sample calculated by using the distance between Mirrors 1 and 2 (about $280mm$, in this configuration) together with the recording configuration design angle $\Delta\theta$. A card is used to mark the center line of the rotation stage and aim Beam 1 at it, adjusting the angle of Mirror 1 for this purpose. Then a card is placed partially in the path of Beam 1 after Mirror 1 and the rotation stage is adjusted to achieve retro-reflection. Then, the rotation stage is adjusted by the angle

$\Delta\theta/2$ towards Mirror 2. The longitudinal position of the rotation stage is adjusted until Beam 1 is reflected to the center line of Mirror 2. The previous four steps are repeated until no further longitudinal adjustment is needed for Beam 1 to reflect to the center line of Mirror 2. Now, the marker from Mirror 2 is removed and Mirror 2 is rotated until a cross pattern, in between two patterns of vertical lines, is seen at the other side of the PBS. If necessary, the rotation stage may be vertically adjusted to ensure the beams are horizontal for the complete round-trip path. Now, the mirror slide is removed from the prism and the prism rotated by 135° minus the design angle ψ. To finish the alignment, a dummy sample is placed behind the prism, and the second prism is pressed against it. The longitudinal and lateral positions of the sample are then adjusted to achieve suitable intersection of the two beams on the sample. Since it is important that the front prism in the arrangement have clean surfaces, and it is easier to clean the prisms when they are not on the rotation stage, the second prism is used as the front prism. To do this, a 180° rotation is performed before or after the longitudinal and lateral alignments.

3.2.3 Sample Preparation

The HRF600X photopolymer comes in laminate sheets, of which a piece of the appropriate size can be laminated onto a substrate or waveguide either prior to or after exposure. Before exposure, the thinner of the two Mylar cover sheets is removed. Lamination to the substrate or waveguide can be done either manually with a roller, or with a laminating machine such as the HiVAC-600, by E & H Laminators.

3.2.4 Grating Recording

Once the recording configuration has been aligned, the sample can be put in place and recording can proceed. An exposure dosage of $70mJ/cm^2$ [9] and an exposure intensity of $0.24mW/cm^2$ [60] have been determined to produce a strong index modulation on this photopolymer and are used in these exposures. Using a syringe, a few drops (4 to 6) of index matching oil are placed on the sample, and then it is positioned flush against the first prism. For the VGC to have a straight edge, a slide with a metal mask covering part of it may be placed against the prism, with the sample then placed against the mask. In this case, the index matching oil is also used between the prism and the slide, and between the slide and the sample. Then, the index matching oil is applied to the second prism and the second prism is placed flush against the sample. Two rubber bands, one near the bottom of the prisms and one near the top, are used to compress the sample between them and produce better contact between the prisms, mask, and sample. Care must be taken to ensure that the slide and the front prism are clean in order to avoid any distortion or dimming of the incident beams. To allow for the relaxation of stresses, the exposure is not started until at least $90sec$ after the rubber bands have been put in place.

After exposure, the sample is carefully removed. First the rubber bands are removed and then the second prism and the sample are slid out. The sample is thoroughly rinsed with isopropanol to remove the index matching oil and then dried with nitrogen gas. The sample is then given a $100mJ/cm^2$ uniform UV exposure to set the grating pattern. Then, the sample is cured on a hot plate at $150°C$ for $90min$. The second, thicker Mylar cover can then be removed. There have been reports in the literature about distortions in the grating pattern during curing, possibly caused by the Mylar layer [85]. However, these problems were not encountered in this research by following the above procedure. Finally, the portion of the photopolymer material that lies before the edge of the grating itself can be removed by carefully cutting it with a sharp blade and then peeling it away.

3.3 Summary

In this chapter, we have described the general design and fabrication steps taken to fabricate the VGCs investigated in this research. The design method to obtain grating vectors for a given structure was discussed. The K_x component of the grating vector determines the outcoupling angle, while the K_z component can be adjusted for optimal outcoupling using the GWBC. The design of the fabrication configuration and its alignment were also discussed. Finally, sample preparation, exposure, and curing were reviewed. The specific design parameters used for the VGCs fabricated for this research will be presented in subsequent chapters, where the individual VGCs are discussed.

CHAPTER 4

MEASUREMENT CONFIGURATIONS

In this chapter, the configurations and methods used to measure the performance of the VGCs discussed in this thesis are described. First the input coupling testing configuration is presented. Then, the outcoupling configuration is discussed. This configuration used to measure the polarization dependence/independence of the VGCs, as well as the wavelength-dependent performance of a VGC.

4.1 VGC Input Coupling Testing Configuration

In order to determine the outcoupling angle of a fabricated coupler, the testing configuration shown in Fig. 4.1 is used. Light transmitted through the sample (not diffracted) is measured for a range of incident angles. Significant dips in this transmission correspond to incoupling to the modes supported by sample being tested. The angle of incoupling for each mode (which is the same angle at which light from that mode is outcoupled) is described by Eq. (3.1). Each mode has a different propagation constant β. Since the indices and thicknesses of the sample are known, then with the propagation constant β of each mode, this measurement allows the fabricated K_x component of the grating vector to be determined.

4.2 VGC Output Coupling Testing Configuration

In order to measure the coupling coefficients of the VGCs, the testing configuration shown in Fig. 4.2 has been constructed. A fiber-pigtailed laser diode is used as the source. A polarization control bench, consisting of a half-wave plate and a linear polarizer, coupled to a length of polarization-maintaining fiber allows for control of the polarization of the light coupled into the waveguide. Light coming out of the surface of the sample is filtered by another polarizer and then collected by a digital camera attached to a microscope which looks down on the sample. A photograph of this measurement configuration is shown in Fig.

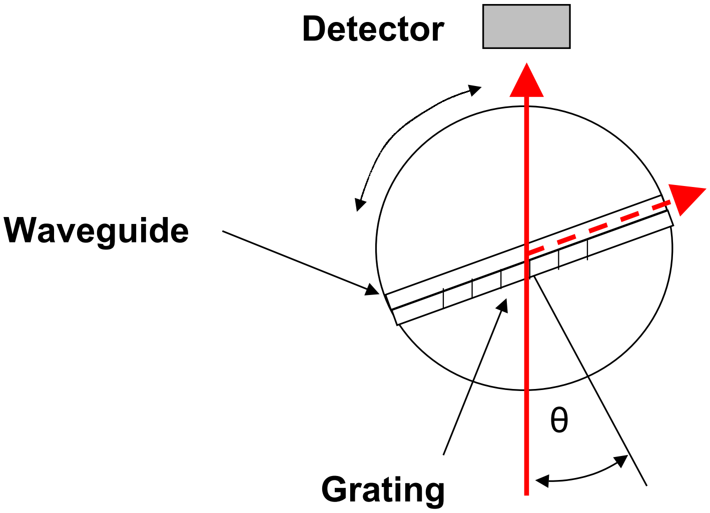

Figure 4.1: Diagram of grating incoupling testing configuration.

4.3. A close-up photograph showing the fiber, sample, polarizer, and microscope objective is shown in Fig. 4.4. The light collected includes both scattered light and the light being outcoupled by the grating, with the scattered light being dominant only when there is little or no outcoupling. In such a case, the loss coefficient due to scattering and absorption can be measured. The images collected provide an intensity profile of the light at the surface of the VGC. The microscope can be rotated over a wide range of angles above the sample so that light outcoupled at angles far from normal to the coupler (as in the case of the polarization-independent couplers described in this thesis) can be captured. The imaging method is an alternative to the fiber scanning method in which a multimode fiber is scanned over to surface of the VGC to determine its intensity profile, as seen in Fig. 4.5. The imaging method is faster because it collects all the data in one shot. Another advantage of the one-shot data collection is that the effect of input power fluctuation over time is eliminated.

The coupling coefficient α of the coupler is related to the normalized measured intensity profile by the equation

$$I_{sup,1}(x) = e^{-2(\alpha+\alpha_{loss})x}, \tag{4.1}$$

where $I_{sup,1}(x)$ is the normalized (to the peak value) measured surface intensity profile, and α_{loss} is the loss coefficient associated with the DuPont HRF 600X photopolymer's absorption and scattering. The sum of the coefficients and α_{loss} is found by making a robust bisquare linear least-squares exponential fit to the measured outcoupled surface intensity profile [83, 86]. The exponential coefficient of the fit is equal to $2(\alpha + \alpha_{loss})$. Each intensity value in a profile is determined by adding the values of all pixels from the captured image at each position along the length of the sample. Robust bisquare linear least squares regression minimizes the sensitivity of standard linear least-squares regression to the presence of outliers [86] and therefore helps minimize the effect of waveguide defects and other scatterers on the measurement. By measuring a similar waveguide sample with no coupler, the α_{loss} can be found. In that case, the exponential coefficient is equal to $2\alpha_{loss}$. The known loss coefficient can then be used to obtain α.

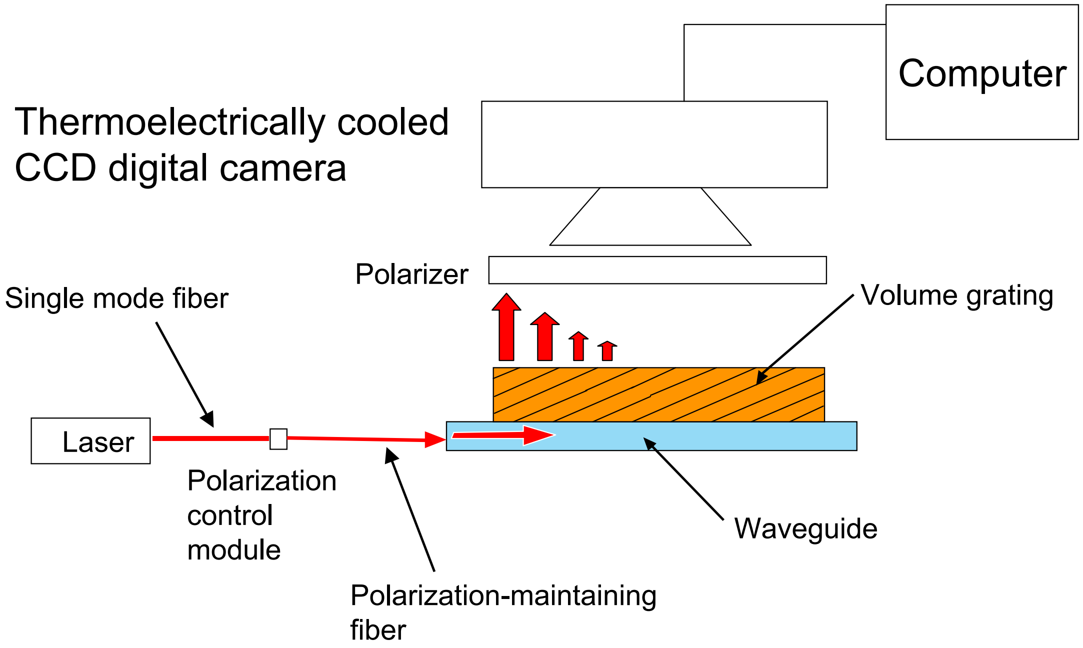

Figure 4.2: Diagram of the imaging VGC outcoupling testing configuration. TE or TM polarized light is end-fire coupled into the waveguide, and the microscope-attached camera collects the light being coupled out.

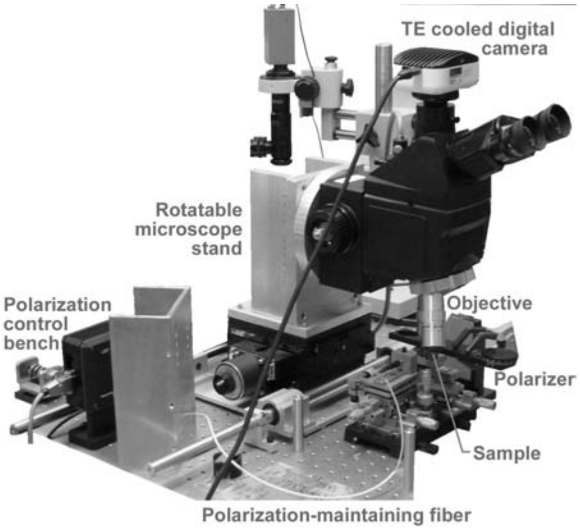

Figure 4.3: Photograph of the imaging VGC outcoupling testing configuration.

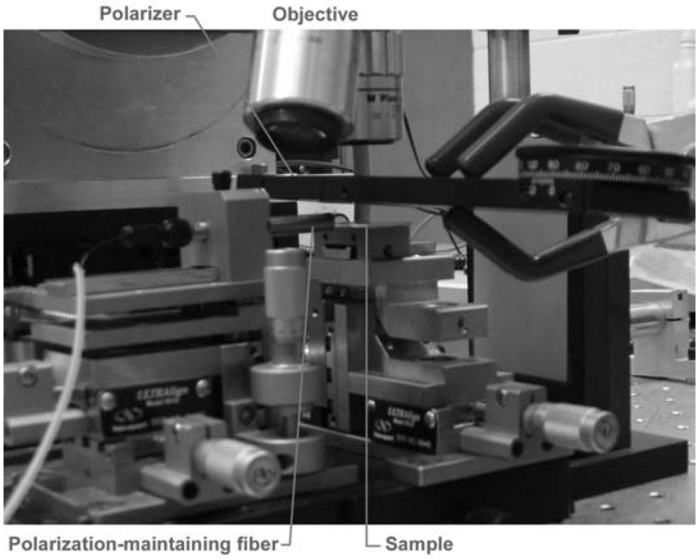

Figure 4.4: Close-up photograph of the imaging VGC outcoupling testing configuration showing the fiber, sample, polarizer and objective.

By using the measured value of α and the calculated value of η (which is primarily determined by the geometry of the coupler and thus unlikely to deviate from the expected value), CE_{TE} and CE_{TM} can be calculated for a coupler of a given length.

In order to measure the wavelength-dependent performance of a VGC, a tunable wavelength source can be used. The intensity profile of the light at the surface of the VGC can then be imaged for each wavelength included in the measurement, and the α for each can thus be found.

4.3 Summary

In this chapter, the incoupling and outcoupling testing configurations used to measure the performance of VGCs fabricated for this research have been reviewed. The advantages of the imaging outcoupling configuration and its application of the measurement of the outcoupling of TE and TM polarized light, as well as light of varying wavelength, have been discussed.

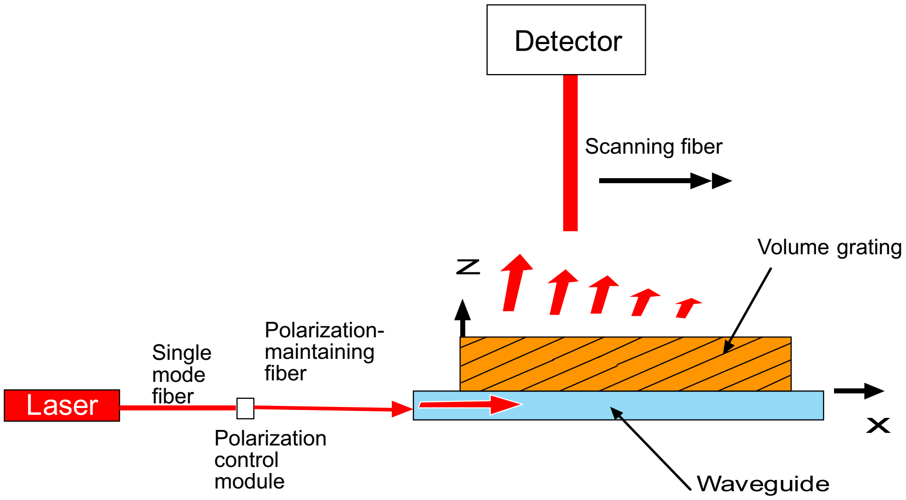

Figure 4.5: Diagram of the fiber scanning VGC outcoupling testing configuration. TE or TM polarized light is end-fire coupled into the waveguide, and the scanning fiber collects the light being coupled out.

CHAPTER 5

POLARIZATION-DEPENDENT VOLUME GRATING COUPLER

In this chapter, the design, fabrication and testing of a $L = 400\mu m$ polarization-dependent VGC are presented. The design parameters of the coupler and of the fabrication configuration are discussed first. The fabrication of polymer waveguides and VGCs in the "VG in the Waveguide" configuration are then presented. The results of input coupling testing, done to determine the input/output coupling angle of the fundamental waveguide mode and thus the K_x component of the grating, are discussed next. The measured results of outcoupling performance for TE and TM polarized light are then presented. Finally, the measured results of outcoupling performance at room temperature ($22°C$)and at a temperature of $71°C$ for a VGC of the same design for TE polarized light are presented.

5.1 Design of Polarization-Dependent VGC

In this section, the design of a polarization-dependent VGC is presented. This VGC, as well as all the other fabricated couplers presented in this thesis, is in the "VG in the Waveguide" configuration, as shown in Fig. 2.1b. For ease of testing of this device, it was designed for operation at $\lambda_o = 635nm$.

5.1.1 Waveguide

The waveguide material is the Avatrel 2190P polymer manufactured by Promerus, LLC; a negative-tone photodefinable polyolefin with $n = 1.52$ [87, 88]. The grating material is DuPont's HRF600X photopolymer, with $n = 1.50$ [9]. For the grating design, $\Delta n = 0.015$ is assumed. The structure has a glass substrate with $n = 1.4567$ and air superstrate ($n = 1$). The structure has a waveguide/grating layer of thickness $t_w = t_g = 5.8\mu m$, supporting 7 modes. The modes in the Avatrel waveguide have slightly larger propagation constants than those in the HRF600X photopolymer because of the Avatrel's higher index of refraction. The reflection at the interface between the two materials, however, is expected to be small. Although the analysis, design, and testing techniques described in this thesis can be applied individually to each mode, the focus of this research is on the fundamental mode in the structure. This mode has a propagation constant of $\beta_0 = 14.83\mu m^{-1}$ in the unmodulated photopolymer.

5.1.2 Grating Design

As can be seen in Fig. 2.5, a VGC outcoupling at an angle close to 0° will display a strong polarization-dependence, with strong outcoupling of TE polarized light and very weak outcoupling of TM polarized light. Therefore, the design of a polarization-dependent VGC can be achieved simply by designing a VGC with an outcoupling angle close to 0°. As we have seen, the outcoupling angle can be set by proper design of the K_x component of the grating vector. Using the propagation constant of the fundamental waveguide mode $\beta_0 = 14.83\mu m^{-1}$, an outcoupling angle $\theta_c = 0.2°$ and Eq. (3.1), a value of $K_x = 14.80\mu m^{-1}$ is obtained. The value of $K_z = 14.84\mu m^{-1}$ is then set by Eq. (3.2). Table 5.1 shows the parameters and calculated performance of the polarization-dependent VGC.

Table 5.1: Design values and calculated performance characteristics of $L = 400\mu m$ polarization-dependent VGC for $\lambda_o = 635nm$.

Parameter	**Value**
$K_x(\mu m^{-1})$	14.80
$K_z(\mu m^{-1})$	14.84
$\Lambda(\mu m)$	0.30
$\phi(°)$	44.9
$\theta_c(°)$	0.2
$\alpha_{TE}(mm^{-1})$	12.51
$\alpha_{TM}(mm^{-1})$	0.0001
η_{TE}	0.976
η_{TM}	0.965
CE_{TE}	0.976
CE_{TM}	0.00008

5.2 Fabrication of Polarization-Dependent VGC

In this section, the fabrication of the polarization-dependent VGC is presented. The parameters used in the interferometric exposure configuration used to fabricate the grating design discussed above are presented. This is followed by a brief discussion of the fabrication of the waveguide.

5.2.1 Fabrication Parameters

Once the design parameters of the polarization-dependent VGC were known, the design of the interferometric exposure configuration was performed, following the procedure described in Sec. 3.2.1. The parameters obtained are shown in Table 5.2. With these parameters available, the grating recording configuration, shown in Fig. 3.2, was aligned following the procedure described in Sec. 3.2.2.

Table 5.2: Design Parameters for Interferometric Exposure Fabrication of Polarization-Dependent VGC for $\lambda_o = 635nm$.

Parameter	**Value**
$K_x(\mu m^{-1})$	14.80
$K_z(\mu m^{-1})$	14.84
$K_{z,exp}(\mu m^{-1})$	14.39
$\theta_{g1}(^\circ)$	67.12
$\theta_{g2}(^\circ)$	21.29
$Area\ 1(cm^2)$	2.02
$Area\ 2(cm^2)$	0.84
$\theta_1(^\circ)$	45.76
$\theta_2(^\circ)$	34.60
$\Delta\theta(^\circ)$	80.36
$\psi(^\circ)$	5.58
$Ratio$	2.40

5.2.2 Sample Preparation and Exposure

A $6\mu m$ sheet of HRF600X photopolymer was laminated on to a square $25mm$ x $25mm$ x $1mm$ thick glass substrate as described in Sec. 3.2.3. Then the sample was subjected to interferometric exposure, uniform exposure and curing, as described in Sec. 3.2.4. Photopolymer shrinkage during the curing, as discussed in Sec. 3.1, results in a final grating thickness $t_g = 5.8\mu m$.

5.2.3 Waveguide Fabrication

A $6\mu m$ thick slab waveguide of Avatrel 2190P polymer was fabricated on the substrate with the polarization-dependent VGC already on it. A diagram of this two-material waveguide and grating in the "VG in the Waveguide" configuration can bee seen in Fig. 5.1. First, the AP3000 adhesion promoter from Dow Chemical was spun onto the substrate at $3000RPM$ for $30sec$. Immediately following this, a 25% solution of Avatrel in mesitylene was spun on at $200RPM$ for $5sec$ and then $500RPM$ for $40sec$. A syringe with a $0.2\mu m$ filter was used to deposit the Avatrel solution on the substrate [87]. The sample was then placed on a hot plate at $100°C$ for $10min$ and finally cured at $150°C$ for $90min$.

5.3 Measurements of Polarization-Dependent VGC

In this section, the measurements performed on the polarization-dependent VGC are discussed. First, the incoupling measurement is presented. It was used to measure the K_x component of the fabricated coupler and to get an initial assessment of the strength of the fabricated coupler. Then, the output coupling results for TE and TM polarized light and are presented and discussed.

5.3.1 Input Coupling Measurements of Polarization-Dependent VGC

Incoupling testing was performed with a HeNe laser source of freespace wavelength $\lambda = 632.8nm$. The propagation constant for the fundamental mode in this structure at this wavelength is $\beta_0 = 14.89\mu m^{-1}$. A plot of the normalized transmitted intensity through the sample obtained by using the input coupling configuration described in Sec. 4.1 is shown in Fig. 5.2. The rightmost resonance in the plot corresponds to the fundamental waveguide mode, and occurs at the angle $\theta_{c,0} = 1.68°$. By Eq. (3.1), a measured value of $K_x = 14.59\mu m^{-1}$ is obtained for the fabricated coupler.

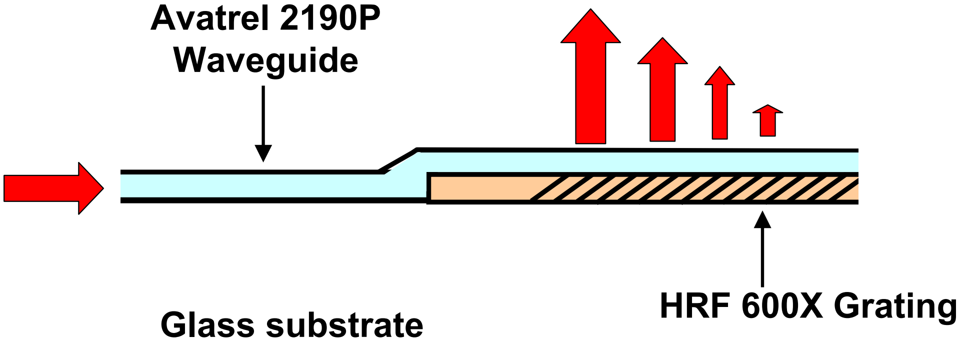

Figure 5.1: The two-material waveguide and VGC in the "VG in the Waveguide" configuration.

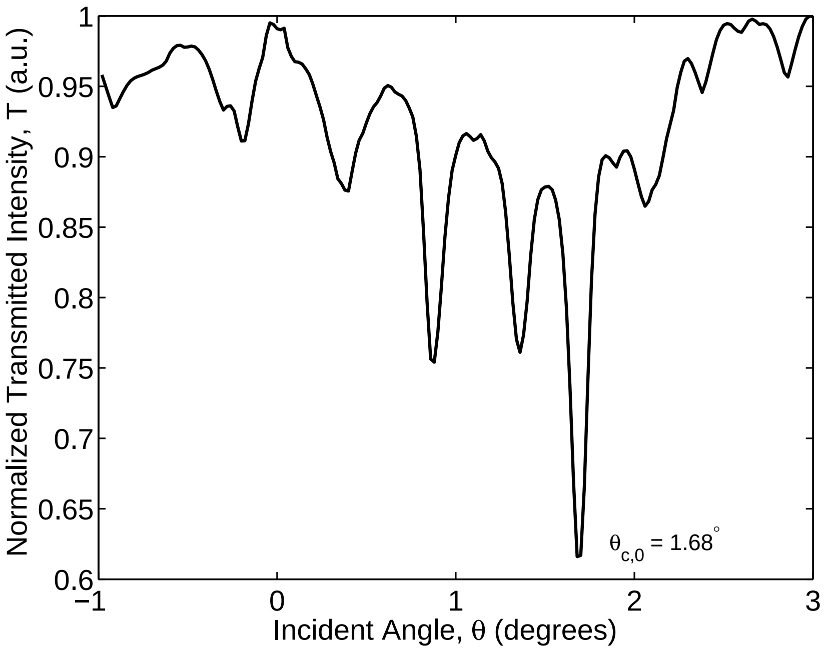

Figure 5.2: Plot of normalized transmitted intensity versus incident angle for the fabricated polarization-dependent VGC.

5.3.2 Output Coupling Measurements of Polarization-Dependent VGC

Outcoupling testing was performed with the configuration presented in Sec. 4.2, using a laser diode with $\lambda_o = 635nm$ as the source. A thermoelectrically cooled Olympus Q-Color3 digital camera was used to capture the sample images. Measurements were made using TE and then TM polarized light to determine the coupling coefficients for each.

5.3.2.1 TE Output Coupling Measurement of Polarization-dependent VGC

The normalized surface intensity profile measured for TE polarized outcoupled light, and the exponential fit to these data are shown in Fig. 5.3. The exponential fit to the data yields a decay factor of $7.51mm^{-1}$. This decay factor is equal to the exponential term in Eq. (4.1), yielding

$$2(\alpha + \alpha_{loss}) = 7.51mm^{-1}, \tag{5.1}$$

The loss coefficient for TE polarized light guided in a $5.8\mu m$ thick film of DuPont HRF 600X photopolymer was measured by the same imaging method and found to be $\alpha_{loss,TE} =$

$0.073mm^{-1}$. Inserting this value into Eq. (5.1) yields a measured $\alpha_{TE} = 3.68mm^{-1}$.

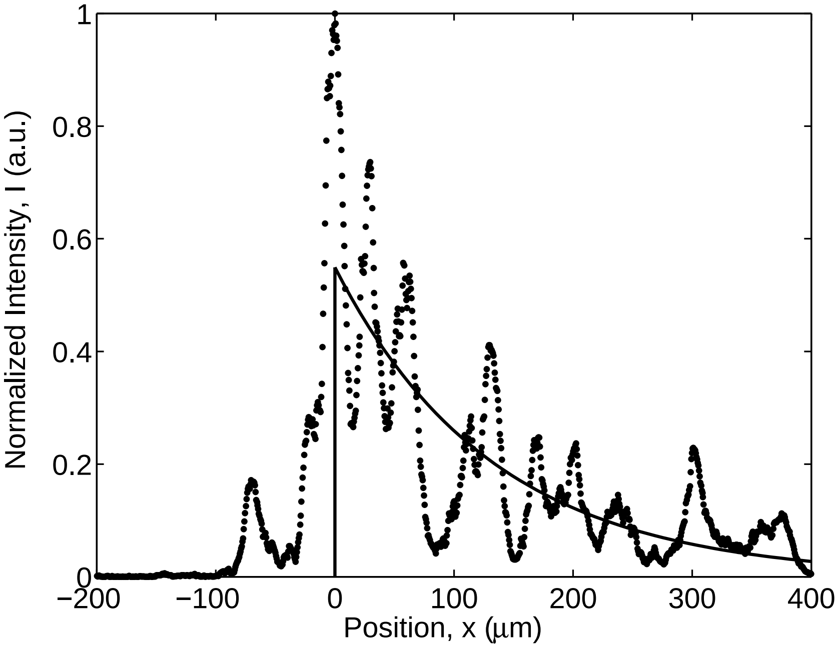

Figure 5.3: Measured normalized surface intensity profile of polarization-dependent VGC for TE polarized light and exponential fit.

Inserting the measured values of $\alpha_{TE} = 3.68mm^{-1}$ and $\alpha_{loss,TE} = 0.073mm^{-1}$, the calculated value of $\eta_{TE} = 0.976$ and the length $L = 400\mu m$ into Eq. (2.16), a $CE_{TE} = 0.909$ is determined for this coupler.

5.3.2.2 TM Output Coupling Measurement of Polarization-dependent VGC

The surface intensity profile measured for TM polarized outcoupled light, and the exponential fit to these data are shown in Fig. 5.4. The exponential fit to the data yields a decay factor of $0.408mm^{-1}$. This decay factor is equal to the exponential term in Eq. (4.1), yielding

$$2(\alpha + \alpha_{loss}) = 0.408mm^{-1}, \tag{5.2}$$

The loss coefficient for TM polarized light guided in a $5.8\mu m$ thick film of DuPont HRF 600X photopolymer was measured by the same imaging method and found to be $\alpha_{loss,TM} = 0.061mm^{-1}$. Inserting this value into Eq. (5.2) yields a measured $\alpha_{TM} = 0.143mm^{-1}$.

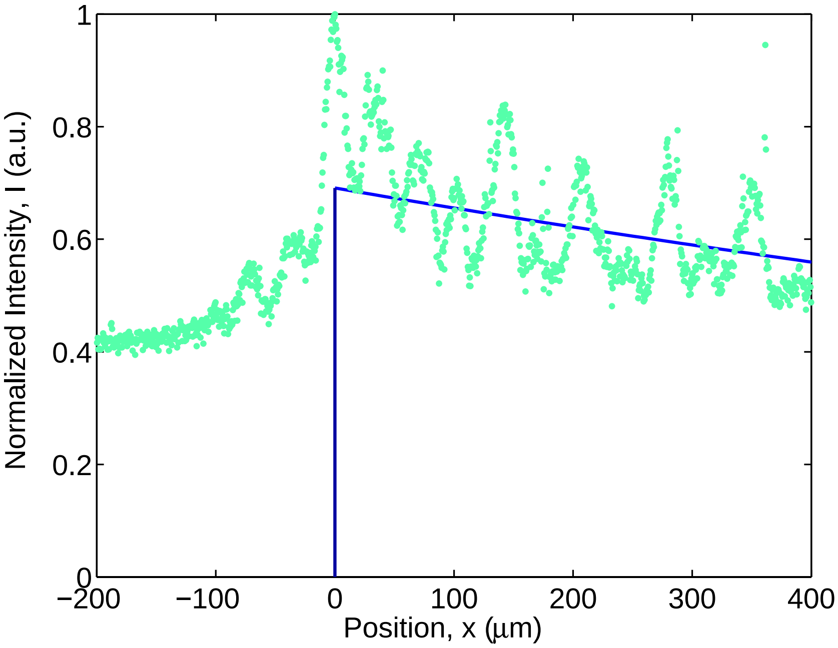

Figure 5.4: Measured normalized surface intensity profile of polarization-dependent VGC for TM polarized light and exponential fit.

Inserting the measured values of $\alpha_{TM} = 0.183mm^{-1}$ and $\alpha_{loss,TM} = 0.061mm^{-1}$, the calculated value of $\eta_{TM} = 0.965$ and the length $L = 400\mu m$ into Eq. (2.16), a $CE_{TM} = 0.102$ is determined for this coupler.

5.4 Measurements of TE Outcoupling Performance at Room Temperature and Elevated Temperature

In this section, the measurements performed at room temperature and elevated temperature on a VGC are discussed. First, the incoupling measurement is presented. It was used to measure the K_x component of the fabricated coupler and to get an initial assessment of the strength of the fabricated coupler. Then, the output coupling results for TE polarized light at room temperature and at elevated temperature are presented and discussed.

5.4.1 Input Coupling Measurement of VGC for Room Temperature and Elevated Temperature Measurement

Incoupling testing was performed with a HeNe laser source of freespace wavelength $\lambda = 632.8nm$. The propagation constant for the fundamental mode in this structure at this wavelength is $\beta_0 = 14.89\mu m^{-1}$. A plot of the normalized transmitted intensity through the sample obtained by using the input coupling configuration described in Sec. 4.1 is shown in Fig. 5.5. The rightmost resonance in the plot corresponds to the fundamental waveguide mode, and occurs at the angle $\theta_{c,0} = -0.05°$. By Eq. (3.1), a measured value of $K_x = 14.90\mu m^{-1}$ is obtained for the fabricated coupler.

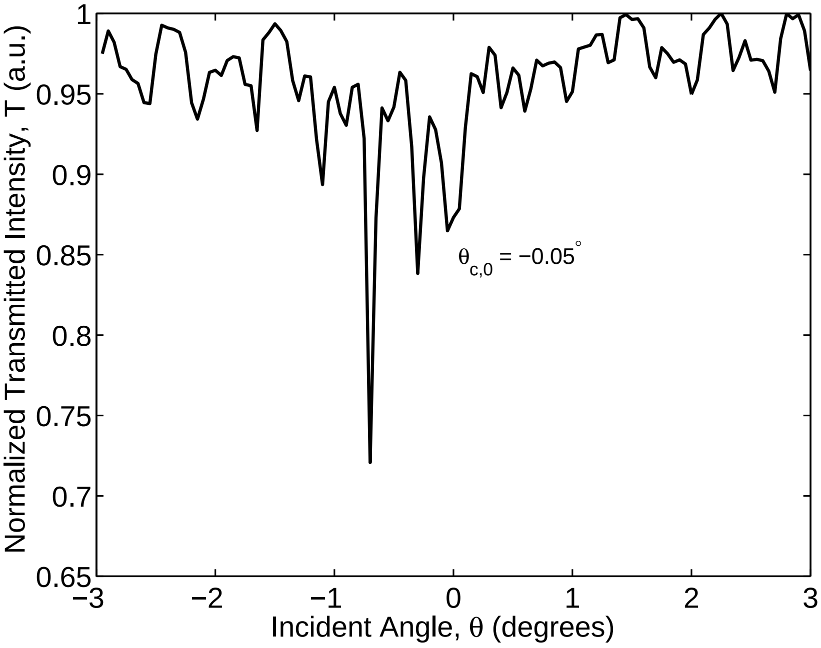

Figure 5.5: Plot of normalized transmitted intensity versus incident angle for the fabricated VGC used in the room temperature and elevated temperature measurement.

5.4.2 Output Coupling Measurements at Room Temperature and Elevated Temperature

Outcoupling testing was performed with the configuration presented in Sec. 4.2, using a laser diode with $\lambda_o = 635nm$ as the source. A thermoelectrically cooled Olympus Q-Color3 digital camera was used to capture the sample images. Measurements were made using TE polarized light at a room temperature of $T = 22°C$ and at an elevated temperature of $T = 71°C$.

The normalized surface intensity profile measured at room temperature, and the exponential fit to these data are shown in Fig. 5.6. The exponential fit to the data yields a decay factor of $11.97mm^{-1}$. This decay factor is equal to the exponential term in Eq. (4.1), yielding

$$2(\alpha + \alpha_{loss}) = 11.97mm^{-1}, \tag{5.3}$$

Inserting the loss coefficient $\alpha_{loss,TE} = 0.073mm^{-1}$ measured for the $5.8\mu m$ thick photopolymer film into Eq. (5.3) yields a measured $\alpha_{TE} = 5.91mm^{-1}$.

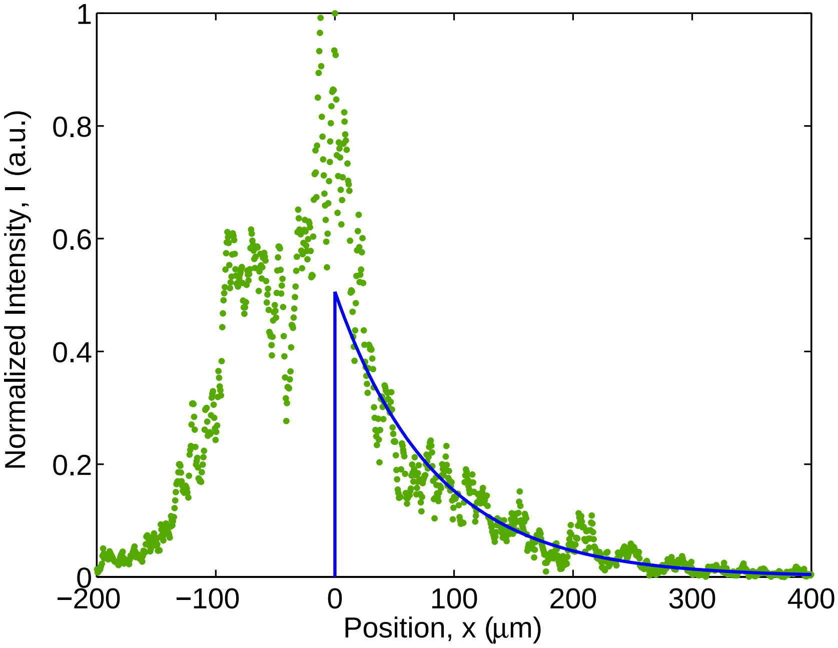

Figure 5.6: Measured normalized surface intensity profile a VGC at room temperature $T = 22°C$ for TE polarized light and exponential fit.

Inserting the measured values of $\alpha_{TE} = 5.91mm^{-1}$ and $\alpha_{loss,TE} = 0.073mm^{-1}$, the calculated value of $\eta_{TE} = 0.976$ and the length $L = 400\mu m$ into Eq. (2.16), a $CE_{TE} = 0.956$ is determined for this coupler at room temperature.

The normalized surface intensity profile measured at $T = 71°C$, and the exponential fit to these data are shown in Fig. 5.7. The exponential fit to the data yields a decay factor of $11.90mm^{-1}$. This decay factor is equal to the exponential term in Eq. (4.1), yielding

$$2(\alpha + \alpha_{loss}) = 11.90mm^{-1}, \tag{5.4}$$

Inserting the loss coefficient $\alpha_{loss,TE} = 0.073mm^{-1}$ measured for the $5.8\mu m$ thick photopolymer film into Eq. (5.4) yields a measured $\alpha_{TE} = 5.88mm^{-1}$. It is assumed in this calculation that the loss coefficient $\alpha_{loss,TE}$ does not differ at $T = 71°C$ from its value at room temperature.

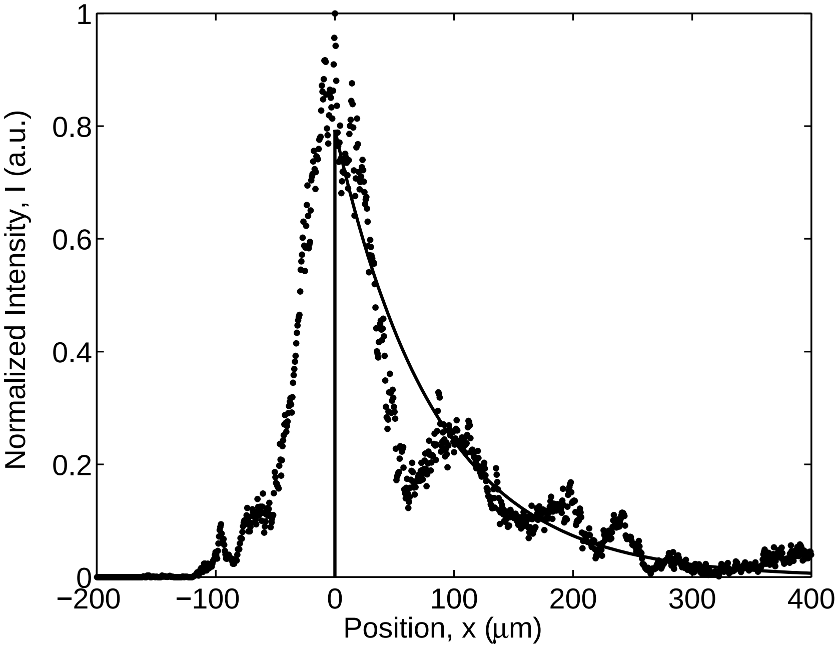

Figure 5.7: Measured normalized surface intensity profile a VGC at a temperature $T = 71°C$ for TE polarized light and exponential fit.

Inserting the measured values of $\alpha_{TE} = 5.88mm^{-1}$ and $\alpha_{loss,TE} = 0.073mm^{-1}$, the calculated value of $\eta_{TE} = 0.976$ and the length $L = 400\mu m$ into Eq. (2.16), a $CE_{TE} = 0.956$ is determined for this coupler at temperature $T = 71°C$.

The measurements done at room temperature $T = 22°C$ and at $T = 71°C$ indicate that between these temperatures the performance of the fabricated remained fairly constant. The coupling coefficient α_{TE} was reduced by only 0.6% for $T = 71°C$ with respect to its value at $T = 22°C$, with the resulting coupling efficiency CE_{TE} for length $L = 400\mu m$ being essentially the same.

5.5 Summary

The design, fabrication, and testing of a $L = 400\mu m$ polarization-dependent VGC have been presented. The design parameters of the coupler were discussed first. The calculated performance parameters for the designed coupler showed very high efficiency for TE polarized light and negligible efficiency for TM polarized light. Grating and waveguide fabrication were discussed next. The two-material waveguide-grating fabrication sequence was introduced. Gratings were first fabricated on glass substrates, with the waveguides subsequently being spun on adjacent to the gratings. Measurement results were presented next. These results are summarized in Table 5.3. Finally, measurement results indicating that the performance of VGCs does not change significantly between room temperature $T = 22°C$ and an elevated temperature of $T = 71°C$ were presented.

Table 5.3: Measured performance characteristics of $L = 400\mu m$ polarization-dependent VGC for $\lambda_o = 635nm$.

Parameter	**Value**
$\theta_c(°)$	1.68
$K_x(\mu m^{-1})$	14.59
$\alpha_{TE}(mm^{-1})$	3.68
$\alpha_{TM}(mm^{-1})$	0.143
CE_{TE}	0.909
CE_{TM}	0.102

CHAPTER 6

POLARIZATION-INDEPENDENT VOLUME GRATING COUPLER

In this chapter, the design, fabrication and testing of a $L = 1mm$ polarization-independent VGC are presented. The polymer waveguides discussed in this and subsequent chapters of this thesis all have the same design parameters and have been fabricated in the same manner as those presented in Ch. 5. The design parameters of the coupler and of the fabrication configuration are discussed first. The results of input coupling testing, done to determine the input/output coupling angle of the fundamental waveguide mode and thus the K_x component of the grating, are discussed next. Then, the measured results of outcoupling performance for TE and TM polarized light are presented. Finally, measurement results indicating the existence of birefringence in the index modulation of the fabricated polarization-independent VGCs are presented.

6.1 Design of Polarization-Independent VGC

In this section, the design of a polarization-independent VGC is presented. This VGC, as well as all the other fabricated couplers presented in this thesis, is in the "VG in the Waveguide" configuration, as shown in Fig. 2.1b. For ease of testing of this device, it was designed for operation at $\lambda_o = 635nm$.

As can be seen in Fig. 2.5, a VGC outcoupling at an angle away from 0° may display a degree of polarization-independence, with strong outcoupling of TE polarized light and substantial outcoupling of TM polarized light. Therefore, the design of a polarization-independent VGC can be achieved designing a VGC with an outcoupling away 0°. Outcoupling angles close to 45° are ideal for this purpose, as seen in Fig. 2.5. However, because of the very large angles required between the interfering beams in their fabrication, they are difficult to fabricate. An outcoupling angle $\theta_c = 30°$ was thus chosen for this design because, while being easier to fabricate, it would still produce mostly polarization-independent outcoupling.

The outcoupling angle can be set by proper design of the K_x component of the grating vector. Using the propagation constant of the fundamental waveguide mode $\beta_0 = 14.83\mu m^{-1}$, an outcoupling angle $\theta_c = 30°$ and Eq. (3.1), a value of $K_x = 9.89\mu m^{-1}$ is obtained. The value of $K_z = 13.99\mu m^{-1}$ is then set by Eq. (3.2). It has been shown that the coupling coefficient has a wide tolerance for variations in the K_z component, however; and it was found that a slightly different value of $K_z = 13.50\mu m^{-1}$ produced similar results but was easier to fabricate, as it required smaller angles between the interfering beams. Therefore, the design value $K_z = 13.50\mu m^{-1}$ was chosen. Table 6.1 shows the design parameters and calculated performance of the polarization-independent VGC.

Table 6.1: Design values and calculated performance characteristics of $L = 1mm$ polarization-independent VGC for $\lambda_o = 635nm$.

Parameter	Value
$K_x(\mu m^{-1})$	9.89
$K_z(\mu m^{-1})$	13.50
$\Lambda(\mu m)$	0.38
$\phi(°)$	36.2
$\theta_c(°)$	30.0
$\alpha_{TE}(mm^{-1})$	13.87
$\alpha_{TM}(mm^{-1})$	1.25
η_{TE}	0.940
η_{TM}	0.974
CE_{TE}	0.940
CE_{TM}	0.894

6.2 Fabrication of Polarization-Independent VGC

In this section, the fabrication of the polarization-independent VGC is discussed. Sample preparation and waveguide fabrication were performed in exactly the same way as in the previous chapter, and thus discussion of them is omitted. The parameters of the interferometric exposure configuration used to fabricate the grating design discussed above are presented.

Once the design parameters of the polarization-independent VGC were known, the design of the interferometric exposure configuration was developed, following the procedure described in Sec. 3.2.1. The parameters obtained are shown in Table 6.2. With these parameters available, the grating recording configuration, seen in Fig. 3.2, was aligned following the procedure described in Sec. 3.2.2.

Table 6.2: Design parameters for interferometric exposure fabrication of polarization-independent VGC for $\lambda_o = 635nm$.

Parameter	**Value**
$K_x(\mu m^{-1})$	9.89
$K_z(\mu m^{-1})$	13.50
$K_{z,exp}(\mu m^{-1})$	13.10
$\theta_{g1}(^\circ)$	70.98
$\theta_{g2}(^\circ)$	34.92
$Area\ 1(cm^2)$	2.41
$Area\ 2(cm^2)$	0.96
$\theta_1(^\circ)$	59.34
$\theta_2(^\circ)$	12.23
$\Delta\theta(^\circ)$	71.58
$\psi(^\circ)$	23.55
$Ratio$	2.52

6.3 Measurements of Polarization-Independent VGC

In this section, the measurements performed on the polarization-independent VGC are discussed. First, the incoupling measurement is presented. It was used to measure the K_x component of the fabricated coupler and to get an initial assessment of the strength of the fabricated coupler. Then, the output coupling results for TE and TM polarized light and are presented and discussed.

6.3.1 Input Coupling Measurements of Polarization-independent VGC

Incoupling testing was performed with a HeNe laser source with freespace wavelength $\lambda = 632.8nm$. The propagation constant for the fundamental mode in this structure at this wavelength is $\beta_0 = 14.89\mu m^{-1}$. A plot of the normalized transmitted intensity through the sample obtained by using the input coupling configuration described in Sec. 4.1 is shown in Fig. 6.1. The rightmost resonance in the plot corresponds to the fundamental waveguide mode, and occurs at the angle $\theta_{c,0} = 30.04°$. By Eq. (3.1), a measured value of $K_x = 9.91\mu m^{-1}$ is obtained for the fabricated coupler.

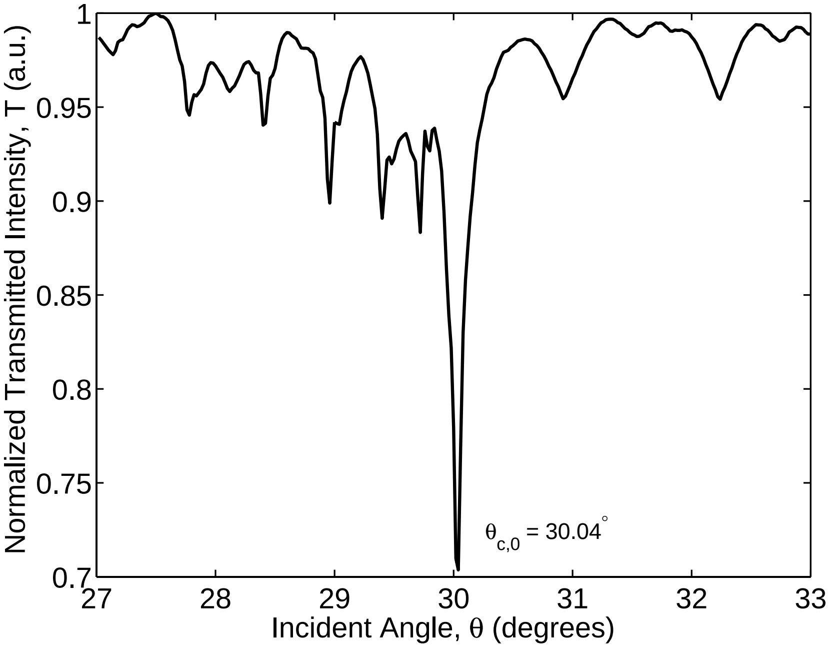

Figure 6.1: Plot of normalized transmitted intensity versus incident angle for the fabricated polarization-independent VGC.

6.3.2 Output Coupling Measurements of Polarization-independent VGC

Outcoupling testing was performed with the configuration presented in Sec. 4.2, using a laser diode with $\lambda_o = 635nm$ as the source. A thermoelectrically cooled Olympus Q-Color3 digital camera was used to capture the sample images. Measurements were made using TE and then TM polarized light to determine the coupling coefficients for each.

6.3.2.1 TE Output Coupling Measurement of Polarization-Independent VGC

The normalized surface intensity profile measured for TE polarized outcoupled light, and the exponential fit to these data are shown in Fig. 6.2. The exponential fit to the data yields a decay factor of $8.86mm^{-1}$. This decay factor is equal to the exponential term in

Eq. (4.1), yielding

$$2(\alpha + \alpha_{loss}) = 8.86mm^{-1}, \tag{6.1}$$

Inserting the loss coefficient $\alpha_{loss,TE} = 0.073mm^{-1}$ measured for the $5.8\mu m$ thick photopolymer film into Eq. (6.1) yields a measured $\alpha_{TE} = 4.36mm^{-1}$.

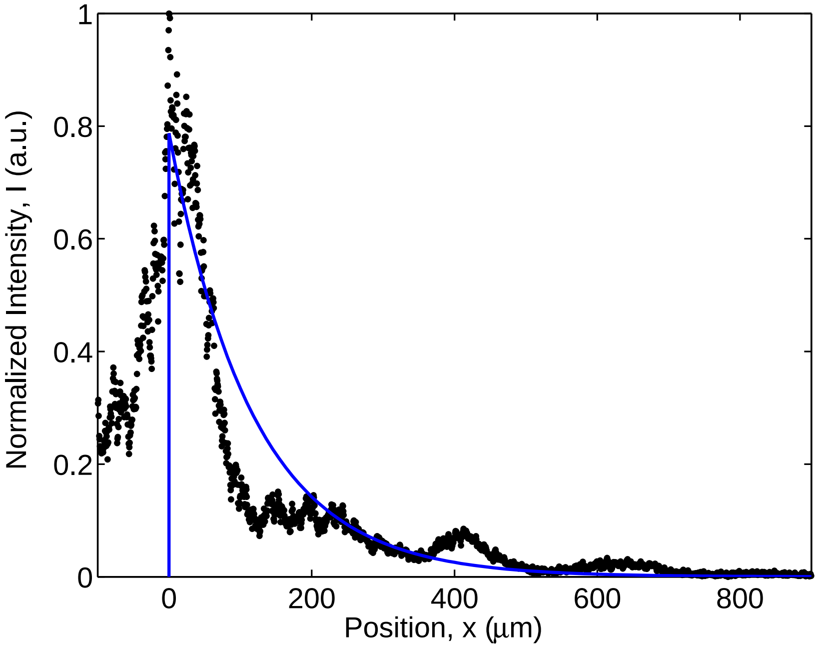

Figure 6.2: Measured normalized surface intensity profile of polarization-independent VGC for TE polarized light and exponential fit.

Inserting the measured values of $\alpha_{TE} = 4.36mm^{-1}$ and $\alpha_{loss,TE} = 0.073mm^{-1}$, the calculated value of $\eta_{TE} = 0.940$ and the length $L = 1mm$ into Eq. (2.16), a $CE_{TE} = 0.924$ is determined for this coupler.

6.3.2.2 TM Output Coupling Measurement of Polarization-independent VGC

The surface intensity profile measured for TM polarized outcoupled light, and the exponential fit to these data are shown in Fig. 6.3. The exponential fit to the data yields a decay factor of $2.28mm^{-1}$. This decay factor is equal to the exponential term in Eq. (4.1), yielding

$$2(\alpha + \alpha_{loss}) = 2.28mm^{-1}, \tag{6.2}$$

Inserting the loss coefficient $\alpha_{loss,TM} = 0.061mm^{-1}$ measured for the $5.8\mu m$ thick photopolymer film into Eq. (6.2) yields a measured $\alpha_{TM} = 1.08mm^{-1}$.

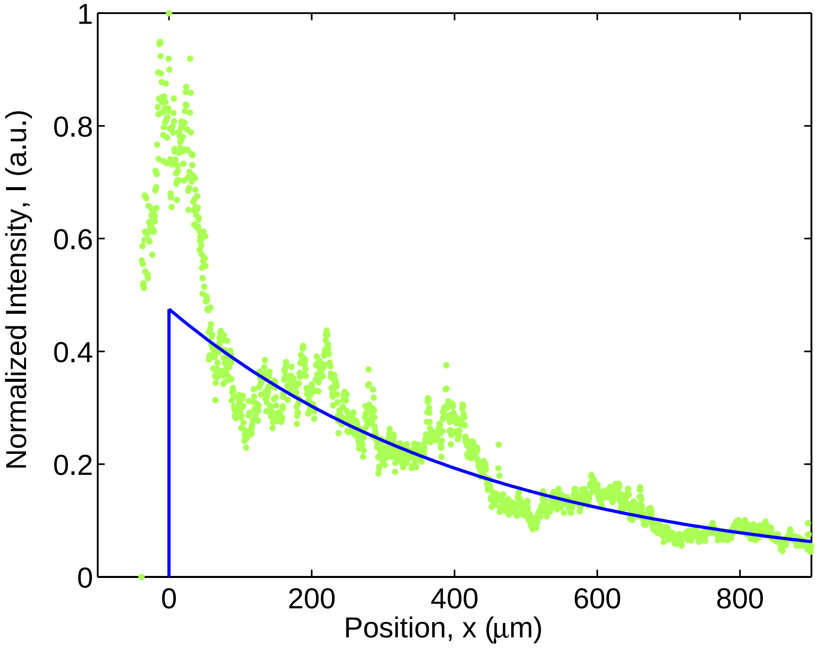

Figure 6.3: Measured normalized surface intensity profile of polarization-independent VGC for TM polarized light and exponential fit.

Inserting the measured values of $\alpha_{TM} = 1.08mm^{-1}$ and $\alpha_{loss,TM} = 0.061mm^{-1}$, the calculated value of $\eta_{TM} = 0.974$ and the length $L = 1mm$ into Eq. (2.16), a $CE_{TM} = 0.827$ is determined for this coupler.

6.4 Birefringence in the Index Modulation of Volume Grating Couplers Fabricated in the HRF-600X Photopolymer

Volume gratings formed with liquid crystal components have been shown to have a strong birefringence in their index modulation [89]. This birefringence strongly impacts the efficiency of the gratings for the TE and TM polarizations, as each effectively experiences a different index modulation. However, birefringence in the index modulation of ordinary (not based on liquid crystals) polymers used in the fabrication of VGCs has been assumed to be nonexistent [67, 90]. Form birefringence, caused not by material properties but by the presence of the grating itself, has been studied and measured in subwavelength volume gratings fabricated in photopolymer materials, and it has been found to be on the order of 0.001 [91].

In this section, measurement results are presented that point to the existence of birefringence in the index modulation of VGCs fabricated in the HRF-600X photopolymer. This birefringence would be helpful for the fabrication of polarization-independent VGCs because it would result in higher coupling coefficients for TM polarized light than would be otherwise expected.

By finding the values of the index modulation Δn that produce the measured coupling coefficients for α_{TE} and α_{TM} obtained in the above section, the Δn for each case can be calculated. For TE polarization, $\alpha_{TE} = 4.36mm^{-1}$, and this corresponds to $\Delta n_{TE} = 0.0097$. For TM polarization, $\alpha_{TM} = 1.08mm^{-1}$, and this corresponds to $\Delta n_{TM} = 0.0141$. This indicates a 45% higher modulation for TM polarized light than for TE polarized light. Two additional measurements were made: one on a sample of the same design as the one above, and one on a VGC designed for outcoupling near 44°. Table 6.3 presents the design values and calculated performance of the VGC designed for outcoupling at $\theta_c = 43.8°$.

Table 6.3: Design values and calculated performance characteristics of an $L = 1mm$ polarization-independent VGC for $\lambda_o = 635nm$ with $\theta_c = 43.8°$.

Parameter	**Value**
$K_x(\mu m^{-1})$	7.98
$K_z(\mu m^{-1})$	12.50
$\Lambda(\mu m)$	0.42
$\phi(°)$	32.6
$\theta_c(°)$	43.8
$\alpha_{TE}(mm^{-1})$	3.63
$\alpha_{TM}(mm^{-1})$	1.70
η_{TE}	0.908
η_{TM}	0.990
CE_{TE}	0.907
CE_{TM}	0.957

The first sample had a measured $\alpha_{TE} = 4.97mm^{-1}$. The modulation fit for this value is $\Delta n_{TE} = 0.0103$. The TM coupling coefficient measured was $\alpha_{TM} = 0.92mm^{-1}$, which fit a value of $\Delta n_{TM} = 0.0131$. For the second sample, a measured $\alpha_{TE} = 3.37mm^{-1}$ was found. The modulation fit for this value is $\Delta n_{TE} = 0.0104$. The TM coupling coefficient measured was $\alpha_{TM} = 1.79mm^{-1}$, which fit a value of $\Delta n_{TM} = 0.0154$. For the three samples measured, the average Δn_{TM} was higher than the average Δn_{TE} by 39%. Table 6.4 shows the Δn values measured for each sample an the average Δn_{TE} and Δn_{TM}.

Table 6.4: Δn_{TE} and Δn_{TM} values from three measured VGCs designed for polarization-independent coupling.

	Δn_{TE}	Δn_{TM}	$\Delta n_{TM}/\Delta n_{TE}$
Sample 1	0.0097	0.0141	1.4536
Sample 2	0.0103	0.0131	1.2718
Sample 3	0.0105	0.0154	1.4667
Average	0.0102	0.0142	1.3922

6.5 Summary

The design, fabrication, and testing of an $L = 1mm$ polarization-independent VGC have been presented. The design parameters of the coupler were discussed first. The calculated performance parameters for the designed coupler showed very high efficiency for both TE and TM polarized light. Measurement results were presented next. These results are summarized in Table 6.5. Finally, measurement results indicating that there is birefringence in the index modulation of the fabricated VGCs were presented. The index modulation found for TM polarized light was 39% higher than for TE polarized light.

Table 6.5: Measured performance characteristics of an $L = 1mm$ polarization-independent VGC for $\lambda_o = 635nm$.

Parameter	**Value**
$\theta_c(^\circ)$	30.04
$K_x(\mu m^{-1})$	9.91
$\alpha_{TE}(mm^{-1})$	4.36
$\alpha_{TM}(mm^{-1})$	1.08
CE_{TE}	0.924
CE_{TM}	0.827

CHAPTER 7

MEASUREMENT OF THE WAVELENGTH-DEPENDENT RESPONSE OF A VOLUME GRATING COUPLER

In this chapter, the design, fabrication and wavelength-dependent performance of a VGC operating at wavelengths near $1520nm$ for TE polarized light will be presented. First, the design and then the fabrication parameters of the coupler will be covered. The results of input coupling testing, done to determine the K_x component of the grating, are discussed next. Then, the outcoupling measurement results and their agreement with calculated values will be discussed.

7.1 Design of VGC for Operation at $\lambda_o = 1520nm$

In this section, the design of a VGC for vertical outcoupling at $\lambda_o = 1520nm$ is presented. This VGC, as well as all the other fabricated couplers presented in this thesis, is in the "VG in the Waveguide" configuration, as shown in Fig. 2.1b. The availability of a suitable tunable laser source with a tuning range between $1440nm$ and $1590nm$ determined the design wavelength of $\lambda_o = 1520nm$. At this wavelength, the index of refraction of the HRF 600X photopolymer was measured with a Metricon prism-coupling system to be $n_g = 1.49$. For this index, and the processed photopolymer film thickness $t_g = 5.8\mu m$, two modes are supported by the structure. As before, only the fundamental waveguide mode will be discussed. The propagation constant of this mode is $\beta_0 = 6.13\mu m^{-1}$. Inserting this value, and the outcoupling angle $\theta_c = 0.1^\circ$ into Eq. (3.1), a value of $K_x = 6.13\mu m^{-1}$ is obtained. The value of $K_z = 6.15\mu m^{-1}$ is then set by Eq. (3.2). Table 7.1 shows the parameters and calculated performance of this VGC for $\lambda_o = 1520nm$ and TE polarization.

Table 7.1: Design values and calculated TE performance characteristics of $L = 1mm$ VGC for $\lambda_o = 1520nm$.

Parameter	**Value**
$K_x(\mu m^{-1})$	6.13
$K_z(\mu m^{-1})$	6.15
$\Lambda(\mu m)$	0.72
$\phi(°)$	44.9
$\theta_c(°)$	0.1
$\alpha_{TE}(mm^{-1})$	2.50
η_{TE}	0.971
CE_{TE}	0.965

7.2 Fabrication of VGC for Operation at $\lambda_o = 1520nm$

In this section, the fabrication of the VGC operating at $\lambda_o = 1520nm$ is discussed. Sample preparation and waveguide fabrication were performed in precisely the same way as in previous chapters, and thus discussion of them is ommitted. The parameters used in the interferometric exposure configuration used to fabricate the grating design discussed above are presented.

Once the design parameters of the polarization-independent VGC were known, the design of the interferometric exposure configuration was performed, following the procedure described in Sec. 3.2.1. The obtained parameters are shown in Table 7.2. With these parameters available, the grating recording configuration, seen in Fig. 3.2, was aligned following the procedure described in Sec. 3.2.2.

7.3 Measurements of VGC for Operation at $\lambda_o = 1520nm$

In this section, the measurements performed on the designed VGC for operation at $\lambda_o = 1520nm$ are discussed. First, the incoupling measurement is presented. It was used to measure the K_x component of the fabricated coupler and to get an initial assesment of the strength of the fabricated coupler. Then, the output coupling results for TE polarized light in the wavelength range of $1440nm$ to $1590nm$ are presented and discussed.

Table 7.2: Design Parameters for Interferometric Exposure Fabrication of a VGC operating at $\lambda_o = 1520nm$.

Parameter	**Value**
$K_x(\mu m^{-1})$	6.13
$K_z(\mu m^{-1})$	6.15
$K_{z,exp}(\mu m^{-1})$	5.97
$\theta_{g1}(^\circ)$	53.52
$\theta_{g2}(^\circ)$	34.96
$Area\ 1(cm^2)$	1.32
$Area\ 2(cm^2)$	0.96
$\theta_1(^\circ)$	17.95
$\theta_2(^\circ)$	12.18
$\Delta\theta(^\circ)$	30.13
$\psi(^\circ)$	2.89
$Ratio$	1.38

7.3.1 Input Coupling Measurements of VGC for Operation at $\lambda_o = 1520nm$

Incoupling testing was performed with a HeNe laser source with wavelength $\lambda = 632.8nm$. The propagation constant for the fundamental mode in this structure at this wavelength is $\beta_0 = 14.89\mu m^{-1}$. A plot of the normalized transmitted intensity through the sample obtained by using the input coupling configuration described in Sec. 4.1 is shown in Fig. 7.1. The rightmost resonance in the plot corresponds to the fundamental waveguide mode, and occurs at the angle $\theta_{c,0} = 59.40^\circ$. By Eq. (3.1), a measured value of $K_x = 6.34\mu m^{-1}$ is obtained for the fabricated coupler.

7.3.2 Output Coupling Measurements of VGC for Operation at $\lambda_o = 1520nm$

Outcoupling testing was performed with the configuration presented in Sec. 4.2, using a HP 8168F tunable laser the source. A Hamamatsu C2741 IR vidicon video camera attached to a computer via a frame grabber was used to capture the sample images. Images captured in this way had significant noise. In order to minimize noise in the captured images, two techniques were employed. The first was to make each image used in these measurements the average of 20 raw images taken through the system. The second technique used consisted of subtracting from the measurement image taken at each wavelength an image (also average

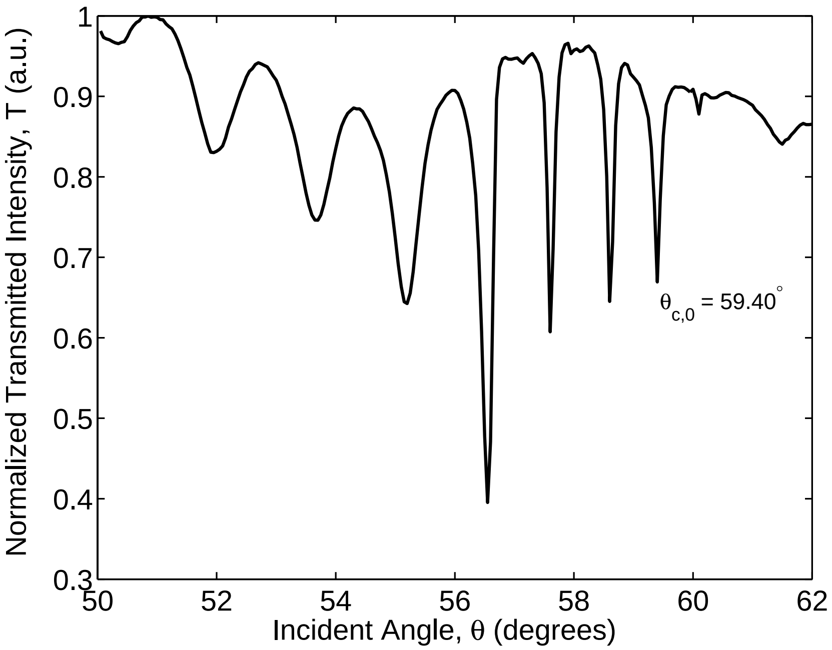

Figure 7.1: Plot of normalized transmitted intensity versus incident angle at $\lambda = 632.8nm$ for the fabricated VGC designed for $\lambda_o = 1520nm$.

of 20 raw images) taken with the source turned off. Measurements were made using TE polarized light to determine the coupling coefficients for wavelengths in the $1440nm$ to $1590nm$with a separation of $10nm$ between measurements.

7.3.2.1 Output Coupling Measurements of VGC for Operation at $\lambda_o = 1520nm$ at Design Wavelength

The normalized surface intensity profile measured for outcoupled light at $\lambda_o = 1520nm$, and the exponential fit to this data are shown in Fig. 7.2. The exponential fit to the data yields a decay factor of $4.36mm^{-1}$. This decay factor is equal to the exponential term in Eq. (4.1), yielding

$$2(\alpha + \alpha_{loss}) = 4.36mm^{-1}, \tag{7.1}$$

Inserting the loss coefficient $\alpha_{loss,TE} = 0.073mm^{-1}$ measured for the $5.8\mu m$ thick photopolymer film (at $\lambda = 635nm$, but expected to be similarly small) into Eq. (7.1) yields a measured $\alpha_{TE} = 2.11mm^{-1}$.

Inserting the measured values of $\alpha_{TE} = 2.11mm^{-1}$ and $\alpha_{loss,TE} = 0.073mm^{-1}$, the

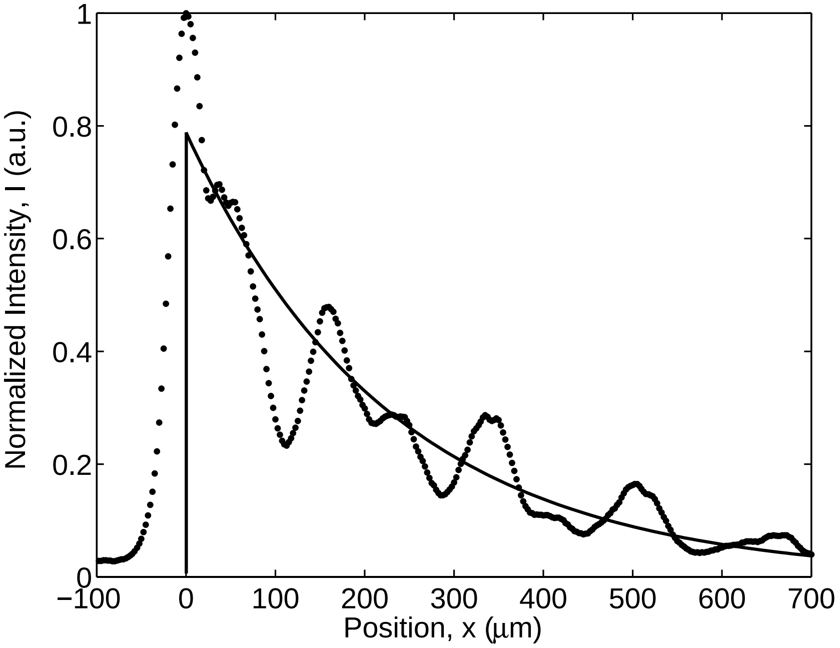

Figure 7.2: Measured normalized surface intensity profile of a VGC operating at $\lambda_o = 1520nm$ and exponential fit.

calculated value of $\eta_{TE} = 0.971$ and the length $L = 1mm$ into Eq. (2.16), a $CE_{TE} = 0.935$ is determined for this coupler. The measured performance characteristics of this coupler at $\lambda_o = 1520nm$ are shown in Table 7.3.

Table 7.3: Measured performance characteristics of $L = 1mm$ VGC for $\lambda_o = 1520nm$.

Parameter	**Value**
$\theta_c(°)$	59.40
$K_x(\mu m^{-1})$	6.34
$\alpha_{TE}(mm^{-1})$	2.11
CE_{TE}	0.935

7.3.2.2 Output Coupling Measurements of VGC for Operation at $\lambda_o = 1520nm$ in the $1440nm$ to $1590nm$ Wavelength Range

The same outcoupling measurement described above for $\lambda_o = 1520nm$ was repeated every $10nm$ in the range between $\lambda = 1440nm$ and $\lambda = 1590nm$. Figure 7.3 shows a plot of the measured coupling coefficients versus wavelengths. It also includes a plot of the calculated coupling coefficients versus wavelength for the VGC design described above, with a $\Delta n = 0.014$. There is good agreement between the two.

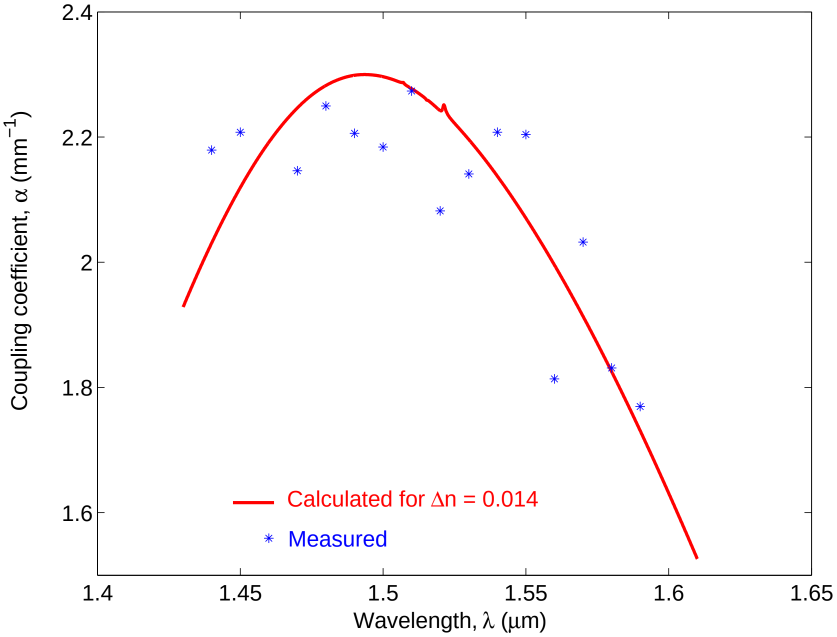

Figure 7.3: Measured and calculated coupling coefficients versus wavelength for fabricated VGC with a design wavelength $\lambda_o = 1520nm$.

7.4 Summary

The design, fabrication and testing of a $L = 1mm$ VGC operating at $\lambda_o = 1520nm$ have been presented. More importantly, the wavelength-dependence of the coupling coefficient has been measured and compared to calculated results, with good agreement betwen the two. The design parameters of the coupler were discussed first. The calculated performance parameters for the designed coupler at $\lambda_o = 1520nm$ were then presented. The measurement method and results were presented next. The measurements confirm the analytical prediction of a rather wide bandwidth for VGC outcoupling, as described in Sec. 2.5.

CHAPTER 8

VOLUME GRATING COUPLERS INTEGRATED WITH POLYMER PILLARS FOR OPTICAL INTERCONNECTS: DEMONSTRATION AND PERFORMANCE MEASUREMENT

Sea of Leads is an ultrahigh density ($> 10^4/cm^2$) compliant chip input/output (I/O) interconnection technology that has shown great promise in terms of reliability, electrical performance, manufacturing throughput, and cost [92]. Sea of Polymer Pillars (SoPP) is a newer chip I/O interconnection technology that incorporates many of the advantages of SoL and adds the ability to serve as dual electrical/optical I/O interconnects. For optical interconnects, one of the main advantages of polymer pillars is their high tolerance to coefficient of thermal expansion mismatches which can lead to misalignments detrimental to optical performance [93, 94]. A circular polymer pillar (PP) consists of a cylinder of transparent polymer that stands vertically on a substrate. They can be fabricated in a wide variety of sizes, and because of the high index contrast between the pillar polymer index of refraction ($n_p = 1.52$) [94] and that of air, they can guide light along their axis [93]. A photograph of a PP with a height of $102\mu m$ and a diameter of $55\mu m$ is shown in Fig. 8.1. PPs with a square base have also been fabricated.

In order to couple light between pillars and waveguides running horizontally along chips and substrates, high efficiency couplers are needed. In this chapter, we demonstrate the ability of VGCs to be integrated with PPs, and test the transmission efficiency of pillars for light being outcoupled from a polymer waveguide by a VGC.

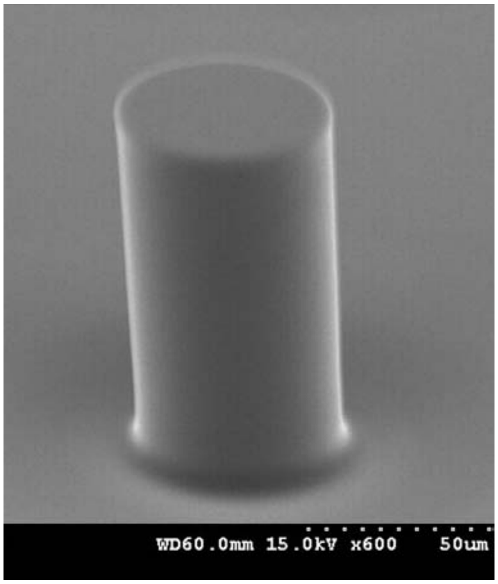

Figure 8.1: Polymer pillar with a height of $102 \mu m$ and a diameter of $55 \mu m$ [94].

8.1 Volume Grating Coupler Outcoupling Through a Polymer Pillar

Equation (2.16) describes outcoupling from a VGC into an air superstrate. If light is being coupled into a PP, the structure and dimension of the pillar must be taken into account in order to calculate the efficiency of coupling into the pillars. Figure 8.2 is a diagram of the relevant dimensions for a circular pillar which sits on top of a VGC. Only light propagating within the width of the pillar is considered in this analysis, which also assumes that the VG begins exactly at the edge of the pillar closest to the waveguide and that the power distribution of the light in the waveguide is uniform in the y direction.

The coupling is first modeled for an element of width dy and length x_1. For this i-th element, the fraction of the power coupled from the waveguide to the pillar is the coupling efficiency, CE_i, which can be modeled as

$$CE_i = \eta \frac{\alpha}{\alpha + \alpha_{loss}} e^{-2(\alpha+\alpha_{loss})(R-\frac{x_1}{2})}[1 - e^{-2(\alpha+\alpha_{loss})x_1}], \tag{8.1}$$

where the term $e^{-2(\alpha+\alpha_{loss})(R-\frac{x_1}{2})}$ corresponds to the power coupled out of the grating before the pillar begins and therefore not available for coupling into the pillar. The total coupling

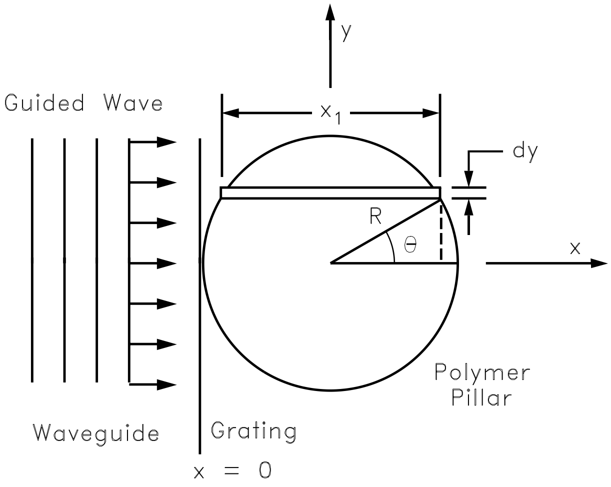

Figure 8.2: Waveguide propagating light in the x direction incident upon a volume grating coupler with a circular polymer pillar on top of it.

efficiency for power in the waveguide into power in the pillar is then

$$CE = 2\eta \frac{\alpha}{\alpha + \alpha_{loss}} \int_{y=0}^{R} e^{-2(\alpha+\alpha_{loss})(R-\frac{x_1}{2})}[1 - e^{-2(\alpha+\alpha_{loss})x_1}]dy. \tag{8.2}$$

With

$$x_1 = 2R\cos\theta, \tag{8.3}$$

$$y = R\sin\theta \tag{8.4}$$

and

$$dy = R\cos\theta d\theta, \tag{8.5}$$

the total coupling efficiency from waveguide to pillar is then modeled as

$$CE = 2\eta R \frac{\alpha}{\alpha + \alpha_{loss}} \int_{\theta=0}^{\pi/2} e^{-2R(\alpha+\alpha_{loss})(1-\cos\theta)} [1 - e^{-4(\alpha+\alpha_{loss})R\cos\theta}] \cos\theta d\theta. \qquad (8.6)$$

This integral can be solved numerically to calculate the coupling efficiency into a pillar. For a square pillar, making the same assumptions regarding the power in the waveguide and the relative positions of the edge of the pillar and the beginning of the VGC as above, Eq. (2.16) can be applied simply by making L equal to the dimension of the pillar along the x direction.

8.2 Sample Fabrication

The waveguide and VGC design and fabrication methods used in this chapter are exactly the same as those described in Ch. 5. After a substrate with a polymer slab waveguide and a VGC had been fabricated, PPs were fabricated on top of them. Pillars were fabricated with the Avatrel 2000P polynorbornene by Promerus, LLC [88]. Their fabrication involves spin coating of a polymer film, soft baking, mask exposure of the film, hard baking, spray developing and a thermal cure at $200°C$ [93]. Pillars of $40\mu m$ height and $25\mu m$ diameter were fabricated on a $71\mu m$ pitch on top of both the waveguide and VGC regions of the sample.

8.3 Sample Testing

8.3.1 Volume Grating Coupler Input Coupling Measurement

Incoupling testing was performed with a HeNe laser source with source wavelength $\lambda = 632.8nm$ on the waveguide/grating substrate prior to pillar fabrication. The propagation constant for the fundamental mode in this structure at this wavelength is $\beta_0 = 14.89\mu m^{-1}$. A plot of the normalized transmitted intensity through the sample obtained by using the input coupling configuration described in Sec. 4.1 is shown in Fig. 8.3. The rightmost resonance in the plot corresponds to the fundamental waveguide mode, and occurs at an angle $\theta_{c,0} = 0.14°$. By Eq. (3.1), a measured value of $K_x = 14.86\mu m^{-1}$ is obtained for the fabricated coupler.

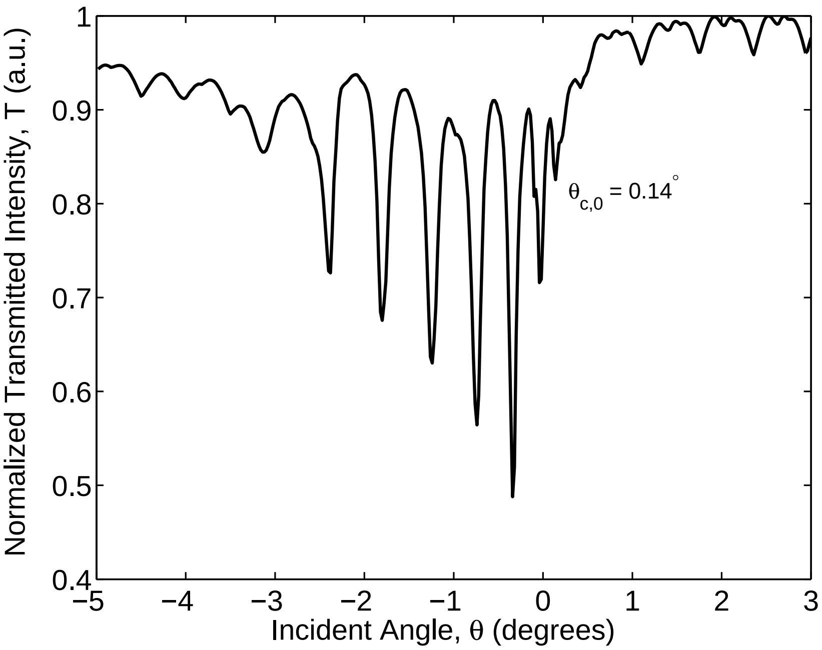

Figure 8.3: Plot of normalized transmitted intensity versus incident angle for the fabricated VGC to be integrated with polymer pillars.

8.3.2 Measurement of Volume Grating Coupler Output Coupling Through Polymer Pillars

Outcoupling testing was performed with the configuration presented in Sec. 4.2, using a laser diode with $\lambda_o = 635nm$ as the source. A thermoelectrically cooled Olympus Q-Color3 digital camera was used to capture the sample images. Measurements were made using TE polarized light to determine the coupling coefficient of the VGC and also to compare the power coupled out through a pillar to the power coupled out directly into air.

The normalized surface intensity profile measured for light outcoupled directly through the surface of the coupler, and the exponential fit to this data are shown in Fig. 8.4. The exponential fit to the data yields a decay factor of $14.81mm^{-1}$. By the same procedure used in Sec. 5.3.2.1, a measured value of$\alpha_{TE} = 7.33mm^{-1}$ is obtained. The normalized surface intensity profile along a row of 12 pillars (with the data taken from each pillar tip surface), and the exponential fit to this data are shown in Fig. 8.5. The exponential fit to the data yields a decay factor of $11.06mm^{-1}$. By the same procedure used in Sec. 5.3.2.1, a measured value of $\alpha_{TE} = 5.46mm^{-1}$ is obtained. The exponential decay seen in the intensity at the pillar tips indicates pillar-to-pillar uniformity in the transmission of the outcoupled light. Since it has many more data points, the first measurement ($\alpha_{TE} = 7.33mm^{-1}$) is taken as the more reliable indicator of the coupling of the fabricated VGC. With a calculated $\eta_{TE} = 0.976$, the measured value of $\alpha_{loss,TE} = 0.073mm^{-1}$ for the intrinsic loss in the photopolymer, and using Eq. (2.16), a value of $CE_{TE} = 0.299$ is obtained for a coupler length of $L = 25\mu m$, the diameter of one pillar in this sample. A surface plot of the output intensity of the tip of a single pillar is shown in Fig. 8.6.

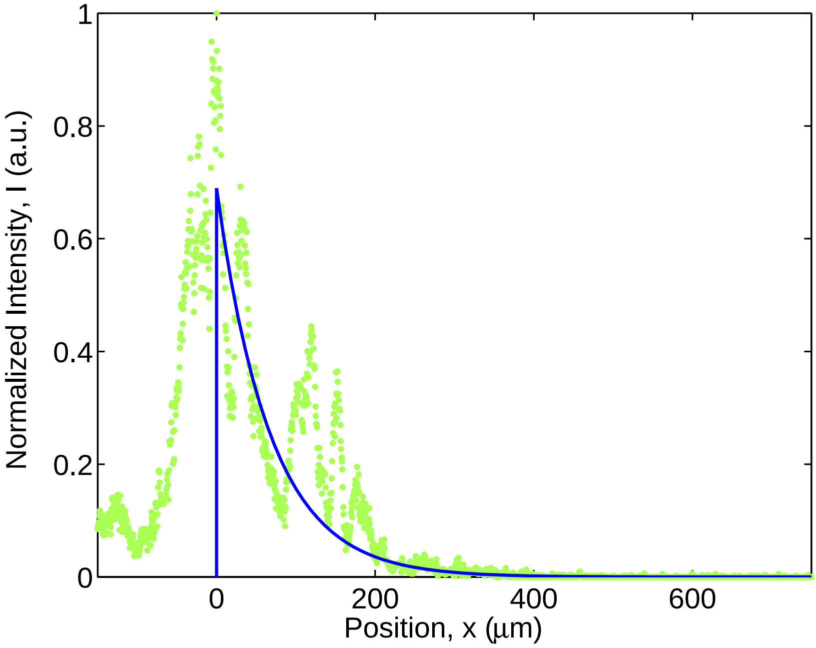

Figure 8.4: Measured normalized surface intensity profile for VGC coupling directly to air and exponential fit.

The pillars' efficiency in transmitting the outcoupled light was examined as well. Figure 8.7 shows a plot of the normalized surface intensity profile along a row of pillars minus the exponential fit to these data. This plot shows increased intensity at the pillar locations. The explanation for this resides in the fact that in the pillar regions, the VGC effectively has a polymer cover with index $n_{cov} = n_p = 1.52$, rather than the air cover in non-pillar regions. Since this n_{cov} is higher than the grating index, it produces additional leakage of power from the waveguide mode to the pillar. Simulated results indicate a 32% higher CE for an $L = 25\mu m$ segment with $n_{cov} = 1.52$ as compared to an equal length segment with

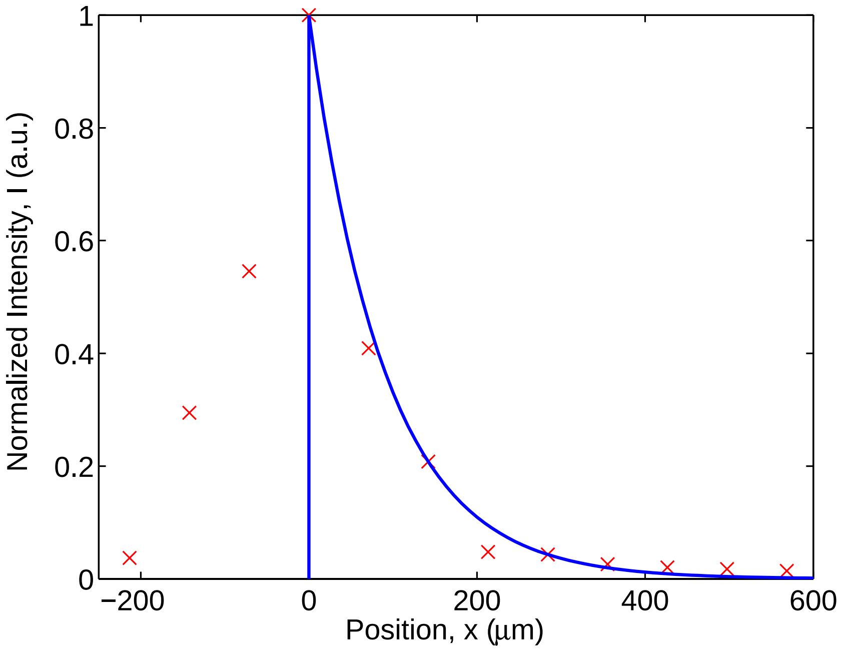

Figure 8.5: Measured normalized surface intensity profile for VGC coupling to polymer pillars and exponential fit.

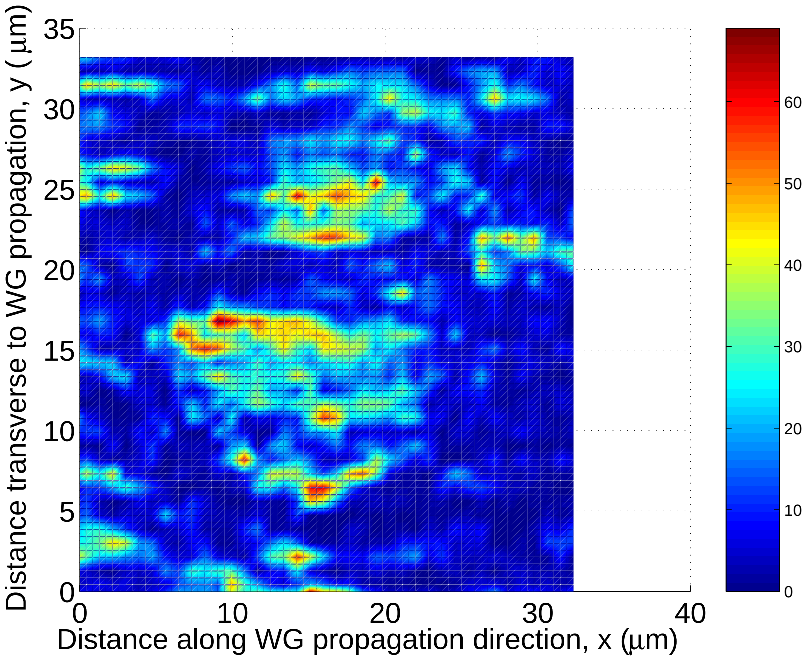

Figure 8.6: Surface plot of the output intensity of a single polymer pillar atop a volume grating coupler.

air cover ($n_{cov} = 1$).

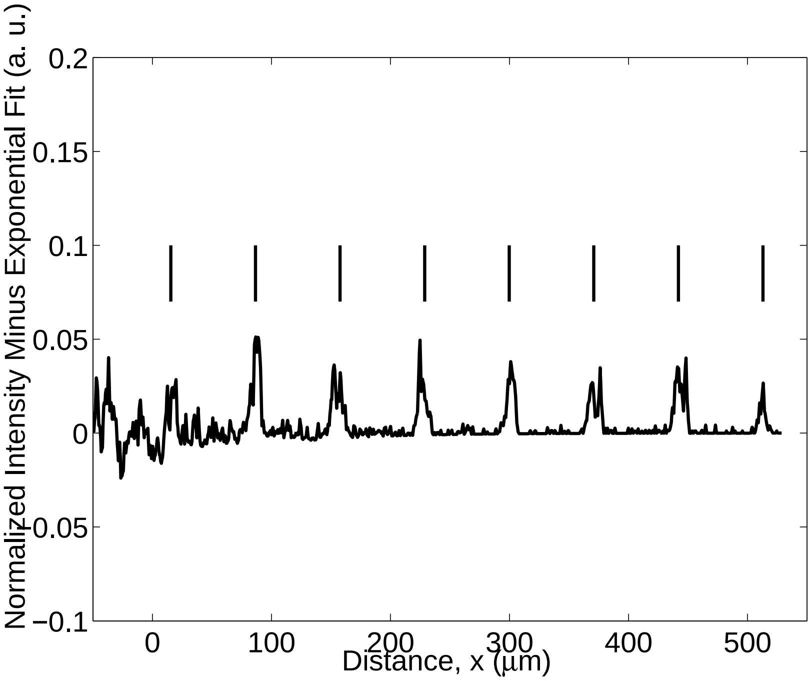

Figure 8.7: Measured normalized surface intensity profile for VGC coupling to polymer pillars minus exponential fit. Vertical lines mark the location of polymer pillars.

Another comparison between the relative output of the pillars and of adjacent areas in which no pillar is present is represented in Fig. 8.8. For three columns of pillars, the output of two rows of pillars and the three non-pillar areas directly adjacent to them were quantified by averaging the pixel values of areas the size of the pillars. There is significant overlap between the two data sets, as evidenced by the bars which indicate the range of data points at each location. This indicates that the pillars have an output that is at least as good and probably slightly better in efficiency than the non-pillar areas. Coupled with the other advantages offered by PPs, especially in terms of alignment, this is a particularly encouraging result.

8.4 Summary

Polymer pillars are an emerging technology with very promising characteristics for optical interconnects. They may provide a low-cost, manufacturable solution for facilitating the alignment of the input and output of optical interconnects to sources and detectors at a

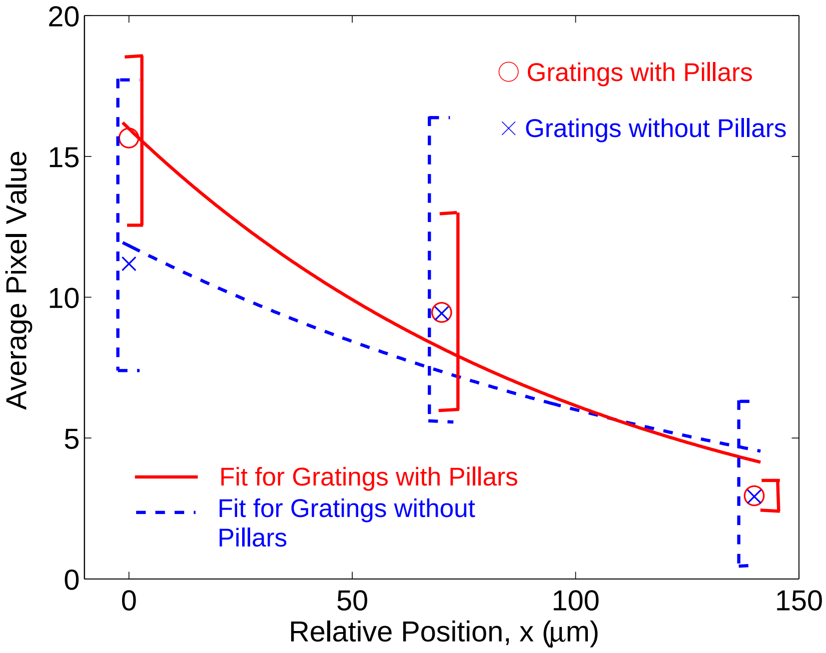

Figure 8.8: Measured average pixel values for pillar and non-pillar areas above VGC and exponential fits. Ranges of measured values are indicated by vertical solid lines (gratings with pillars) and vertical dashed lines (gratings without pillars).

vertical distance away from them. An analytical treatment of the coupling from a waveguide to a polymer pillar through a VGC has been presented. PPs have been fabricated on top of a polymer waveguide with a high-efficiency VGC. The VGC had a measured value of $\alpha_{TE} = 7.33mm^{-1}$. Analysis and measurements show that the α_{TE} is enhanced in the pillar regions by the presence of the high index pillar cover ($n_{cov} = n_p = 1.52$). Measurements also show that transmission of the light through the pillar experiences low loss and that there is essentially no penalty relative to outcoupling directly into air.

CHAPTER 9

CONCLUSIONS

The work presented in this thesis represents contributions to the analysis, design, fabrication and performance of VGCs. The main contributions have been in the understanding of the effects of polarization, wavelength, and loss on the performance of VGCs, as well as in the successful integration of VGCs with polymer pillars. VGCs integrated with polymer pillars represent a complete, practical mechanism for getting light out of a polymer waveguide and into a desired off-substrate location with high efficiency and high alignment tolerance.

9.1 Summary of Results

9.1.1 Analysis of Volume Grating Couplers

The analysis presented in this thesis represents the first systematic, rigorous analysis of the effects of polarization differences on the performance of the various configurations of VGCs for guided-wave optical interconnects. This analysis can be applied to structures with an arbitrary number of layers, and with single or multiple VGs, located either inside the waveguide layer or in adjacent or non-adjacent layers. The results obtained with this analysis allowed the first design of a polarization-independent VGC for a guided-wave optical interconnect. This thesis also includes the first rigorous analysis of the effect of lossy materials on the performance of VGCs. It was found that this effect is small for VGCs with high coupling coefficients.

This thesis also includes the first rigorous analysis of the wavelength-dependent response of VGCs for guided-wave optical interconnects. Understanding of this wavelength-dependence is important in determining the compatibility of VGCs with sources, such as VCSELs, whose wavelength can vary by several nanometers. It is also important in determining if VGCs can be used to enable wavelength multiplexing schemes in optical interconnects. The analysis performed shows that VGCs in guided-wave optical interconnects have a much wider wavelength tolerance than that exhibited by VGs in a bulk diffraction configuration. For typical parameters, FWHM wavelength widths on the order of $200nm$ were typical. It was also found that the wavelength tolerance can be strongly affected by the thickness of the VGC, allowing for some design freedom in determining it. These results point to good compatibility with VCSELs, because of the wide wavelength tolerance observed. They also point to possible compatibility with coarse wavelength multiplexing, where only a few wavelength are multiplexed in a waveguide.

The results pertaining to the analysis of the effects of polarization and loss on the performance of VGCs have been published in a journal article [68]. The results pertaining to the wavelength dependence of the response of VGCs have been accepted for journal publication [75].

9.1.2 Polarization-Dependent Volume Grating Coupler

The first complete measurement of the TE and TM outcoupling performance of a VGC was presented in this thesis. The results obtained confirm the prediction of a strong polarization-dependence in outcoupling at angles close to normal to the surface of a VGC, with a CE_{TE}/CE_{TM} ratio of 8.91. This quality of a VGC could be used in a polarization multiplexing scheme, the use of which is common in other areas of communications.

9.1.3 VGC Performance at Room Temperature vs. Elevated Temperature

A measurement of the coupling efficiency of a VGCs at room temperature $T = 22°$ and at an elevated temperature $T = 71°$ has been presented. A reduction in the coupling coefficient α of less than 1% was found, with a negligible difference in the resulting CE for a coupler of length $L = 400\mu m$.

9.1.4 Polarization-Independent Volume Grating Coupler

The first design, fabrication, and testing of a polarization-independent VGC were presented in this thesis. Polarization-independent performance is desirable in components that interface with optical fibers, and may also be desirable in optical interconnects. A CE_{TE}/CE_{TM} ratio of 1.12 was measured for a fabricated coupler with an outcoupling angle close to 30°.

9.1.5 Birefringence in the Index Modulation of HRF-600X Photopolymer

A measurement of the birefringence in the index modulation of the VGCs fabricated on the HRF-600X photopolymer has been presented. No previous investigation of the birefringence in the index modulation of VGCs fabricated in polymers without liquid crystals has been found in the literature. The birefringence measured accounts for a 39% higher modulation for TM polarized light than for TE polarized light and is helpful for the fabrication of polarization-independent couplers.

9.1.6 Measurement of the Wavelength-Dependent Response of a Volume Grating Coupler

The first measurement of the wavelength-dependent response of a VGC was presented in this thesis. The measurement, performed in the wavelength range of $1440nm$ to $1590nm$ for a VGC designed for operation at $1520nm$, agrees well with the predicted response for the fabricated coupler.

9.1.7 Volume Grating Couplers Integrated with Polymer Pillars for Optical Interconnects: Demonstration and Performance Measurement

In this thesis, the first demonstration of the integration of VGCs with polymer pillars for output from polymer waveguides was presented. An analysis of the coupling efficiency from a polymer waveguide to a polymer pillar through a VGC was presented. Measurement results presented show that after integration with the polymer pillar, the VGC maintained high efficiency outcoupling. The measurements presented also showed pillar uniformity, high efficiency transmission through the pillars of the light being coupled into them from the polymer waveguide, and an enhancement of the outcoupling to the pillars due to the high index of the pillar material compared to air.

9.2 Future Research

Many aspects of VGCs remain to be researched. In terms of analysis, a complete, rigorous study of the input coupling mechanism and its dependence on waveguide thickness, incident beam divergence, incident beam angular and spatial orientation in space, and beam size, is critically needed.

More avenues for future research lie in the areas of fabrication and integration. With a low-loss waveguide material also suitable for grating fabrication, VGCs could be fabricated directly in waveguides, leading to possibly better performance than is possible with the present two-material solution. Also, the use of VGCs made with polymer-dispersed liquid crystals [46] in the configurations described in this thesis could produce high-efficiency, dynamic coupling for optical interconnects. In addition, further and more complete investigations on the effects of elevated temperatures on the performance of VGCs may be needed, since many application environments involve such temperatures.

The integration of VGCs with polymer pillars is only past its first step. By co-designing the dimensions of pillars with the grating performance and properly aligning the edges of the pillars with those of the VGCs, the power outcoupled through the pillars can be maximized. Also, the use of pillars with a square base, for example, may make aligning the pillar and grating edges easier and result in higher performance. Additionally, other components of an optical interconnect, such as MSM detectors and VCSEL sources, may be incorporated to fabricate and measure the performance of a complete system. The integration of polymer pillars may also be exploited to obtain polarization-independent performance from the VGCs without having to outcouple the light in a direction away from normal. A polarization-independent coupler with an outcoupling angle of $\theta_c = 30°$ would, if integrated with a polymer pillar, couple the light into the pillar at an angle 60° from normal to the pillar-air interface, well beyond its critical angle. Thus, the pillar would guide this light upwards along its axis and therefore in the normal direction. Figure 9.1 is a diagram of this configuration. Another situation where the integration of polymer pillars may be exploited is in grating-to-grating coupling from board to chip [47] using two VGCs. The pillars may provide easy and robust alignment for this application. Figure 9.2 is a diagram of this configuration.

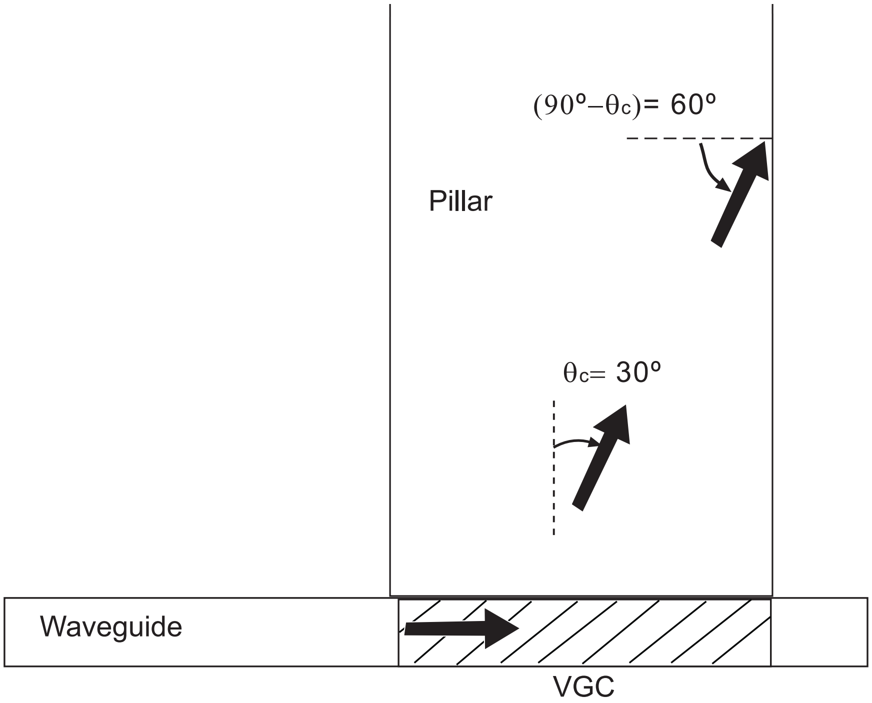

Figure 9.1: Diagram of polarization-independent coupler integrated with polymer pillar.

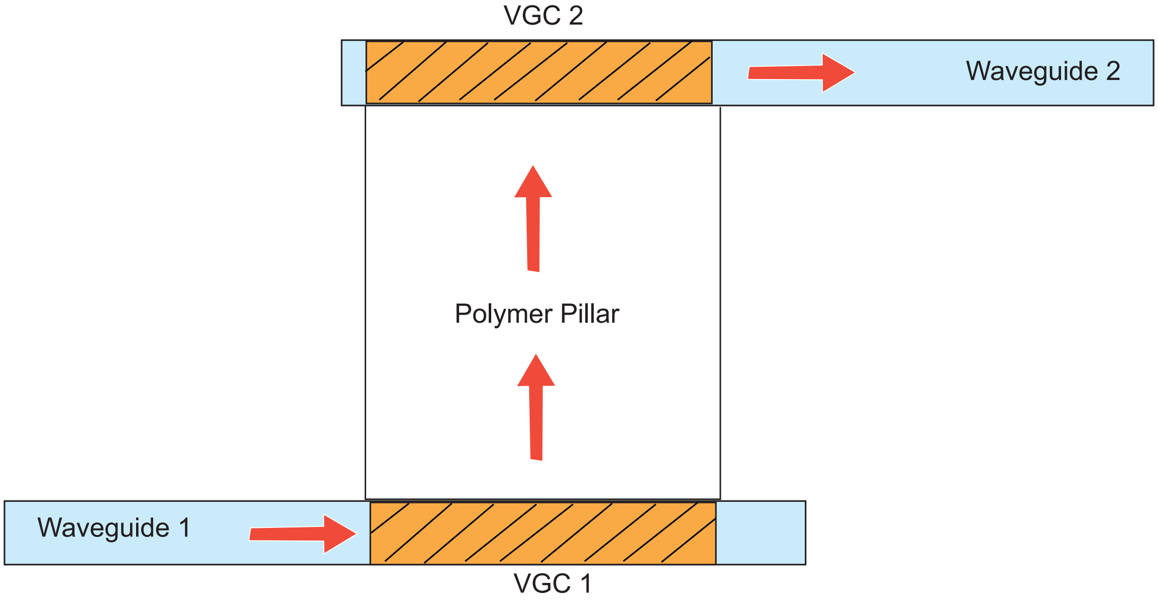

Figure 9.2: Diagram of grating-to-grating coupling through a polymer pillar.

BIBLIOGRAPHY

[1] J. W. Goodman, F. I. Leonberger, S. Y. Kung, and R. A. Athale, "Optical interconnections for VLSI systems," *Proc. IEEE*, vol. 72, pp. 850–866, July 1984.

[2] M. R. Feldman, S. C. Esener, C. C. Guest, and S. H. Lee, "Comparison between optical and electrical interconnects based on power and speed considerations," *Appl. Opt.*, vol. 27, pp. 1742–1751, May 1, 1988.

[3] D. A. B. Miller, "Rationale and challenges for optical interconnects to electronic chips," *Proc. IEEE*, vol. 88, pp. 728–749, June 2000.

[4] R. T. Chen, L. Lin, C. Choi, Y. J. Liu, B. Bihari, L. Wu, S. Tang, R. Wickman, B. Pickor, M. K. Hibbs-Brenner, J. Bristow, and Y. S. Liu, "Fully embedded board-level guided-wave optoelectronic interconnects," *Proc. IEEE*, vol. 88, pp. 780–793, June 2000.

[5] R. K. Kostuk, M. Kato, and Y. T. Huang, "Polarization properties of substrate-mode holographic interconnects," *Appl. Opt.*, vol. 29, pp. 3848–3854, Sept. 10, 1990.

[6] J. H. Yeh and R. K. Kostuk, "Substrate-mode holograms used in optical interconnects: design issues," *Appl. Opt.*, vol. 34, pp. 3152–3164, June 10, 1995.

[7] R. T. Chen, S. Tang, M. M. Li, D. Gerald, and S. Natarajan, "1-to-12 surface normal three-dimensional optical interconnects," *Appl. Phys. Lett.*, vol. 63, pp. 1883–1885, Oct. 4, 1993.

[8] J. H. Yeh and R. K. Kostuk, "Free-space holographic optical interconnects for board-to-board and chip-to-chip interconnections," *Opt. Lett.*, vol. 21, pp. 1274–1276, Aug. 15, 1996.

[9] S. M. Schultz, *High efficiency volume grating coupler*. PhD thesis, Georgia Institute of Technology, 1999.

[10] H. Kogelnik and T. P. Sosnowski, "Holographic thin film couplers," *Bell Syst. Tech. J.*, vol. 49, pp. 1602–1608, Sept. 1970.

[11] W. Driemeier, "Bragg-effect grating couplers integrated in multicomponent polymeric waveguides," *Opt. Lett.*, vol. 15, pp. 725–727, July 1, 1990.

[12] Q. Huang and P. R. Ashley, "Holographic Bragg grating input-output couplers for polymer waveguides at an 850-nm wavelength," *Appl. Opt.*, vol. 36, pp. 1198–1203, Feb. 20, 1997.

[13] M. L. Jones, R. P. Kenan, and C. M. Verber, "Rectangular characteristic gratings for waveguide input and output coupling," *Appl. Opt.*, vol. 34, pp. 4149–4158, July 10, 1995.

[14] V. Weiss, I. Finkelstein, E. Millul, and S. Ruschin, "Coupling and waveguiding in photopolymers," *Proc. SPIE*, vol. 3135, pp. 136–143, 1997.

[15] A. V. Mule', E. N. Glytsis, T. K. Gaylord, and J. D. Meindl, "Electrical and optical clock distribution networks for gigascale microprocessors," *IEEE Trans. VLSI Systems*, vol. 10, pp. 582–594, Oct. 2002.

[16] Semiconductor Industry Association, *International Technology Roadmap for Semiconductors 2002 Update*, 2002.

[17] P. R. Haugen, S. Rychnovsky, and A. Husain, "Optical interconnects for high speed computing," *Opt. Engr.*, vol. 25, pp. 1076–1084, Oct. 1986.

[18] D. A. B. Miller, "Optics for low-energy communication inside digital processors: quantum detectors, sources and modulators as efficient impedance converters," *Opt. Lett.*, vol. 14, pp. 146–148, Jan. 15, 1989.

[19] A. V. Krishnamoorthy and D. A. B. Miller, "Scaling optoelectronic-VLSI circuits into the 21st century: a technology roadmap," *IEEE J. Select. Topics Quantum Electron.*, vol. 2, pp. 55–76, Apr. 1996.

[20] K. Iga, "Surface-emitting laser - its birth and generation of new optoelectronics field," *IEEE J. Select. Topics Quantum Electron.*, vol. 6, pp. 1201–1215, Nov. 2000.

[21] A. J. Beuhler, D. A. Wargowski, T. C. Kowalczyk, and K. D. Singer, "Optical polyimides for single mode waveguides," *Proc. SPIE*, vol. 1849, pp. 92–103, Jan. 1993.

[22] A. Jain, S. Rogojevic, S. Ponoth, N. Agarwal, I. Matthew, W. N. Gill, P. Persans, M. Tomozawa, J. L. Plawsky, and E. Simonyi, "Porous silica materials as low-k dielectrics for electronic and optical interconnects," *Thin Solid Films*, vol. 398-399, pp. 523–522, Nov. 2001.

[23] R. A. Kirchhoff, C. J. Carriere, K. J. Bruza, N. G. Rondan, and R. L. Sammler, "Benzocyclobutenes: A new class of high performance polymers," *J. Macromol. Sci. Chem. Part A*, vol. 28, pp. 1079–1113, 1991.

[24] P. K. Tien, R. Ulrich, and R. J. Martin, "Modes of propagating light waves in thin deposited semiconductor films," *Appl. Phys. Lett.*, vol. 14, pp. 291–294, May 1, 1969.

[25] Y. S. Liu, R. J. Wojnarowski, W. A. Hennessy, J. Rowlette, J. Stack, M. Kadar-Kallen, E. Green, Y. Liu, J. P. Bristow, A. Peczalski, L. Eldada, J. Yardley, R. M. Oscgood, R. Scarmozzino, S. H. Lee, and S. Patra, "High density optical interconnects for board and backplane applications using VCSELs and polymer waveguides," *Proc. 47th Electronic Components and Technology Conference*, pp. 391–398, 1997.

[26] B. L. Booth, "Optical interconnection polymers," in *Polymers for Lightwave and Integrated Optics Technology and Applications* (L. A. Hornak, ed.), pp. 231–266, New York: Marcel Dekker Inc., 1992.

[27] J. Gan, L. Wu, H. Luan, B. Bihari, and R. T. Chen, "Two-dimensional 45° surface-normal microcoupler array for guided-wave optical clock distribution," *IEEE Phot. Technol. Lett.*, vol. 11, pp. 1452–1454, Nov. 1999.

[28] Y. Liu, L. Lin, C. Choi, B. Bihari, and R. T. Chen, "Optoelectronic integration of polymer waveguide array and metal-semiconductor-metal photodetector through micromirror couplers," *IEEE Phot. Technol. Lett.*, vol. 13, pp. 355–357, Apr. 2001.

[29] M. L. Dakss, L. Kuhn, P. F. Heidrich, and B. A. Scott, "Grating coupler for efficient excitation of optical guided waves in thin films," *Appl. Phys. Lett.*, vol. 16, pp. 523–525, June 15, 1970.

[30] A. Katzir, A. C. Livanos, J. B. Shellan, and A. Yariv, "Chirped gratings in integrated optics," *IEEE J. Quantum Electron.*, vol. 13, pp. 296–304, Apr. 1977.

[31] D. Heitmann and R. V. Pole, "Two-dimensional focusing holographic grating coupler," *Appl. Phys. Lett.*, vol. 37, pp. 585–587, Oct. 1, 1980.

[32] N. Eriksson, M. Hagberg, and A. Larsson, "Highly directional grating outcouplers with tailorable radiation characteristics," *IEEE J. Quantum Electron.*, vol. 32, pp. 1038–1047, June 1996.

[33] M. Oh, S. Ura, T. Suhara, and H. Nishihara, "Integrated-optic focal spot intensity modulator using electrooptic polymer waveguide," *J. Lightwave Tech.*, vol. 12, pp. 1569–1576, Sept. 1994.

[34] A. Alphones, "Double grating coupler on a grounded dielectric slab waveguide," *Opt. Comm.*, vol. 92, pp. 35–39, Aug. 1992.

[35] I. A. Avrustky, A. S. Svakhin, V. A. Sychugov, and O. Parriaux, "High-efficiency single-order waveguide grating coupler," *Opt. Lett.*, vol. 15, pp. 1446–1448, Dec. 15, 1990.

[36] L. Li, "Analysis of planar waveguide grating couplers with double surface corrugations of identical period," *Opt. Comm.*, vol. 114, pp. 406–412, Feb. 1995.

[37] M. Li and S. Sheard, "Experimental study of waveguide grating couplers with parallelogramic tooth profiles," *Opt. Engr.*, vol. 35, pp. 3101–3106, Nov. 1996.

[38] S. M. Schultz, E. N. Glytsis, and T. K. Gaylord, "Design of a high-efficiency volume grating coupler for line focusing," *Appl. Opt.*, vol. 37, pp. 2278–2287, Apr. 20, 1998.

[39] S. M. Schultz, E. N. Glytsis, and T. K. Gaylord, "Volume grating preferential-order focusing waveguide coupler," *Opt. Lett.*, vol. 24, pp. 1708–1710, Dec. 1, 1999.

[40] S. M. Schultz, E. N. Glytsis, and T. K. Gaylord, "Design, fabrication, and performance of preferential-order volume grating waveguide couplers," *Appl. Opt.*, vol. 39, pp. 1223–1231, Mar. 10, 2000.

[41] F. Lin, E. M. Strzelecki, and T. Jannson, "Optical multiplanar VLSI interconnects based on multiplexed waveguide holograms," *Appl. Opt.*, vol. 29, pp. 1126–1133, Mar. 10, 1990.

[42] F. Lin, E. M. Strzelecki, C. Nguyen, and T. Jannson, "Highly parallel single-mode multiplanar holographic interconnects," *Opt. Lett.*, vol. 16, pp. 183–185, Feb. 1, 1991.

[43] M. R. Wang, G. J. Sonek, R. T. Chen, and T. Jannson, “Large fanout optical interconnects using thick holographic gratings and substrate wave propagation,” *Appl. Opt.*, vol. 31, pp. 236–249, Jan. 10, 1992.

[44] C. C. Zhou, S. Sutton, R. T. Chen, and B. M. Davies, “Surface-normal 4 x 4 nonblocking wavelength-selective optical crossbar interconnect using polymer-based volume holograms and substrate-guided waves,” *IEEE Phot. Technol. Lett.*, vol. 10, pp. 1581–1583, Nov. 1998.

[45] E. N. Glytsis, N. M. Jokerst, R. A. Villalaz, S. Y. Cho, S. D. Wu, Z. Huang, M. A. Brooke, and T. K. Gaylord, “Substrate-embedded and flip-chip-bonded photodetector polymer-based optical interconnects: analysis, design, and performance,” *J. Lightwave Tech.*, vol. 21, pp. 2382–2394, Oct. 2003.

[46] S. Tang, Y. Tang, J. Colegrove, and D. M. Craig, “Fast electrooptic bragg grating couplers for on-chip reconfigurable optical waveguide interconnects,” *IEEE Phot. Technol. Lett.*, vol. 16, pp. 1385–1387, May 2004.

[47] A. V. Mule’, R. A. Villalaz, T. K. Gaylord, and J. D. Meindl, “Grating-to-grating coupling for board-to-chip optical I/O,” *Appl. Opt.*, vol. 43, 2004 (accepted).

[48] J. H. Harris, R. K. Winn, and D. G. Dalgoutte, “Theory and design of periodic couplers,” *Appl. Opt.*, vol. 11, pp. 2234–2241, Oct. 1972.

[49] R. Ulrich, “Efficiency of optical-grating couplers,” *J. Opt. Soc. Amer.*, vol. 63, pp. 1419–1431, Nov. 1973.

[50] A. Wuthrich and W. Lukosz, “Holography with guided optical waves: II. theory of the diffraction efficiencies,” *Appl. Phys.*, vol. 22, pp. 161–170, 1980.

[51] S. T. Peng, T. Tamir, and H. L. Bertoni, “Leaky-wave analysis of optical periodic couplers,” *Electron. Lett.*, vol. 9, pp. 150–152, Mar. 22, 1973.

[52] S. T. Peng, T. Tamir, and H. L. Bertoni, “Theory of periodic dielectric waveguides,” *IEEE Trans. Microwave Theory and Tech.*, vol. 23, pp. 123–133, Jan. 1975.

[53] K. Ogawa and W. S. C. Chang, “Analysis of holographic thin film grating coupler,” *Appl. Opt.*, vol. 12, pp. 2167–2171, Sept. 1973.

[54] W. Y. Wang and T. J. DiLaura, “Bragg effect waveguide coupler analysis,” *Appl. Opt.*, vol. 16, pp. 3230–3236, Dec. 1977.

[55] W. Driemeier, “Coupled-wave analysis of the Bragg effect waveguide coupler,” *J. Mod. Opt.*, vol. 38, pp. 363–377, Feb. 1991.

[56] H. Kogelnik, “Coupled wave theory for thick hologram gratings,” *Bell Syst. Tech. J.*, vol. 48, pp. 2909–2947, Nov. 1969.

[57] L. Solymar, “Power conservation theorem for 2-dimensional volume holograms,” *Electron. Lett.*, vol. 12, pp. 606–607, Nov. 1976.

[58] L. Solymar, “A general two-dimensional theory for volume holograms,” *Appl. Phys. Lett.*, vol. 31, pp. 820–822, Dec. 15, 1977.

[59] K. Matsumoto, K. Rokushima, and J. Yamakita, "Three-dimensional rigorous analysis of dielectric grating waveguides for general cases of oblique propagation," *J. Opt. Soc. Amer. A*, vol. 10, pp. 269–276, Feb. 1993.

[60] S. D. Wu and E. N. Glytsis, "Finite-number-of-periods holographic gratings with finite-width incident beams: analysis using the finite-difference frequency-domain method," *J. Opt. Soc. Amer. A*, vol. 19, pp. 2018–2029, Oct. 2002.

[61] S. D. Wu and E. N. Glytsis, "Optimization of finite-length input volume holographic grating couplers illuminated by finite-width incident beam," *Appl. Opt.*, vol. 43, 2004 (accepted).

[62] L. D. Dickson, R. D. Rallison, and B. H. Yung, "Holographic polarization-separation elements," *Appl. Opt.*, vol. 33, pp. 5378–5385, Aug. 10, 1994.

[63] J. T. Chang, D. C. Su, and Y. T. Huang, "A four channel polarization and wavelength separation element using substrate-mode stacked holograms," *Appl. Phys. Lett.*, vol. 68, pp. 3537–3539, June 17, 1996.

[64] M. Kato, H. Ito, T. Yamamoto, F. Yamagishi, and T. Nakagami, "Multichannel optical switch that uses holograms," *Opt. Lett.*, vol. 17, pp. 769–771, June 1, 1992.

[65] R. K. Kostuk, T. J. Kim, G. Campbell, and C. W. Han, "Diffractive-optic polarization-sensing element for magneto-optic storage heads," *Opt. Lett.*, vol. 19, pp. 1257–1259, Aug. 15, 1994.

[66] Y. T. Huang, "Polarization-selective volume holograms: general design," *Appl. Opt.*, vol. 33, pp. 2115–2120, Apr. 10, 1994.

[67] J. J. Butler, M. A. Rodriguez, M. S. Malcuit, and T. W. Stone, "Polarization-sensitive holograms formed using $DMP-128$ photopolymer," *Opt. Comm.*, vol. 155, pp. 23–27, Oct. 1998.

[68] R. A. Villalaz, E. N. Glytsis, and T. K. Gaylord, "Volume grating couplers: polarization and loss effects," *Appl. Opt.*, vol. 41, pp. 5223–5229, Sept. 1, 2002.

[69] Y. T. Huang, D. C. Su, and Y. K. Tsai, "Wavelength-division-multiplexing and -demultiplexing by using a substrate-mode grating pair," *Opt. Lett.*, vol. 17, pp. 1629–1631, Nov. 15, 1992.

[70] M. R. Wang, T. Jannson, and G. J. Sonek, "Substrate wavelength-demultiplexing optical interconnects based on superimposed holographic gratings and three-dimensional bragg diffraction," *Opt. Lett.*, vol. 18, pp. 2068–2070, Dec. 15, 1993.

[71] M. R. Wang and F. Lin, "Design of acrhomatic holographic grating couplers for substrate and backplane optical interconnects," *Opt. and Laser Tech.*, vol. 26, pp. 259–264, Aug. 1994.

[72] J. Liu and R. T. Chen, "A two-dimensional dual-wavelength routing network with 1-to-10 cascaded fanouts," *IEEE Phot. Technol. Lett.*, vol. 10, pp. 238–240, Feb. 1998.

[73] J. A. Liu and R. T. Chen, "Path-reversed substrate-guided-wave optical interconnects for wavelength-division demultiplexing," *Appl. Opt.*, vol. 38, pp. 3046–3052, May 10, 1999.

[74] W. H. Huang, Y. Amitai, and A. A. Friesem, "Formation of a planar coarse wavelength-division multiplexer and demultiplexer with reflection volume phase gratings," *Appl. Opt.*, vol. 41, pp. 5851–5855, Oct. 1, 2002.

[75] R. A. Villalaz, E. N. Glytsis, T. K. Gaylord, and T. N. Nakai, "Wavelength response of waveguide volume grating couplers for optical interconnects," *Appl. Opt.*, vol. 43, 2004 (accepted).

[76] W. Gambogi, A. Weber, and T. Trout, "Advances and applications of DuPont holographic photopolymer," *Proc. SPIE*, vol. 2043, pp. 2–13, Aug. 1993.

[77] C. Zhao, J. Liu, Z. Fu, and R. T. Chen, "Shrinkage correction of volume phase holograms for optical interconnects," *Proc. SPIE*, vol. 3005, pp. 224–229, 1997.

[78] S. Piazzolla and B. K. Jenkins, "Holographic grating formation in photopolymers," *Opt. Lett.*, vol. 21, pp. 1075–1077, July 15, 1996.

[79] S. D. Wu and E. N. Glytsis, "Holographic grating formation in photopolymers: Analysis and experimental results based on a nonlocal diffusion model and the rigorous coupled-wave analysis," *J. Opt. Soc. Amer. B*, vol. 20, pp. 3046–3052, June 2003.

[80] M. G. Moharam, E. B. Grann, D. A. Pommet, and T. K. Gaylord, "Formulation for stable and efficient implementation of the rigorous coupled-wave analysis of binary gratings," *J. Opt. Soc. Amer. A*, vol. 12, pp. 1068–1076, May 1995.

[81] M. Neviere, "The homogeneous problem," in *Electromagnetic Theory of Gratings*, ch. 5, pp. 123–157, Berlin: Springer-Verlag, 1980.

[82] D. E. Muller, "A method for solving algebraic equations using an automatic computer," *Math. Tables and Other Aids to Comp.*, vol. 10, pp. 208–215, Oct. 1956.

[83] The Mathworks Inc., "Matlab, ver. 6.5.1," 2003.

[84] M. L. Jones, *Design of normal-incidence waveguide-imbedded phase gratings for optical interconnects in multi-chip modules.* PhD thesis, Georgia Institute of Technology, 1995.

[85] G. Gavrilov, I. Maurer, K. Muratikov, S. Pirasevskaya, and G. Sotnikova, "Fringe effects during recording transmission holographic gratings in photopolymers," *Optics and Spectros.*, vol. 78, pp. 280–282, Feb. 1995.

[86] W. DuMouchel and F. O'Brien, "Integrating a robust option into a multiple regression computing environment," in *Computing Science and Statistics: Proceedings of the 21st Symposium on the Interface* (K. Berk and L. Malone, eds.), pp. 297–301, Alexandria, VA: American Statistical Association, 1989.

[87] A. V. Mulé, *Volume grating coupler-based optical interconnect technologies for polylithic gigascale integration.* PhD thesis, Georgia Institute of Technology, 2004.

[88] www.promerus.com.

[89] J. J. Butler, M. S. Malcuit, and M. A. Rodriguez, "Diffractive properties of highly birefringent volume gratings: investigation," *J. Opt. Soc. Amer. B*, vol. 19, pp. 183–189, Feb. 2002.

[90] J. Liu, Z. Fu, and R. T. Chen, "Polarization sensitivity of photopolymer-based volume holograms for one-to-many surface normal optical interconnects," *Opt. Eng.*, vol. 37, pp. 660–665, Feb. 1998.

[91] C. Yang and P. Yeh, "Form birefringence of volume gratings in photopolymers," *Appl. Phys. Lett.*, vol. 69, pp. 3468–3470, Dec. 2, 1996.

[92] M. S. Bakir, H. A. Reed, H. D. Thacker, C. S. Patel, P. A. Kohl, K. P. Martin, and J. D. Meindl, "Sea of leads (SoL) ultrahigh density wafer-level chip I/O interconnections for gigascale integration (GSI)," *IEEE Trans. Electron. Dev.*, vol. 50, pp. 2039–2048, Oct. 2003.

[93] M. S. Bakir, T. K. Gaylord, K. P. Martin, and J. D. Meindl, "Sea of polymer pillars: compliant wafer-level electrical-optical chip I/O interconnections," *IEEE Phot. Technol. Lett.*, vol. 15, pp. 1567–1569, Nov. 2003.

[94] M. S. Bakir, T. K. Gaylord, O. O. Ogunsola, E. N. Glytsis, and J. D. Meindl, "Optical transmission of polymer pillars for chip I/O optical interconnections," *IEEE Phot. Technol. Lett.*, vol. 16, pp. 117–119, Jan. 2004.

VITA

Ricardo A. Villalaz was born on July 15, 1975 in the city of Panama, Rep. of Panama. He received the Bachelor of Electrical Engineering with Highest Honor in 1998 and the Master of Science in Electrical and Computer Engineering in 2000, both from the Georgia Institute of Technology in Atlanta, Georgia. During this time, he performed research on constant-bandwidth scanning technology for monochromators and colorimetry-based retardation measurement methods. His current research interests include integrated optics and diffractive optics. Ricardo is a member of IEEE, the Optical Society of America, the Society of Hispanic Professional Engineers, Tau Beta Pi and Eta Kappa Nu.